Technical Physics Letters, Vol. 31, No. 7, 2005, pp. 537–540. Translated from Pis'ma v Zhurnal Tekhnicheskoĭ Fiziki, Vol. 31, No. 13, 2005, pp. 1–9.

Stable Oscillations and Effective Acceleration of Charged Particles at the Electric Field Antinode of a Standing Electromagnetic Wave

A. F. Kurin

Voronezh State University, Voronezh, 394006 Russia

e-mail: afkurin@mail.ru

Revised manuscript received February 28, 2005

Abstract—The phenomenon of the stable motion of charged particles at the electric field antinode of a standing electromagnetic wave is analyzed using the Hill equation derived from the equations of motion. The domains of parameters characterizing the field and charges are determined for the regime of stable oscillations. It is shown that the charged particles remaining at the electric field antinode can be accelerated to relativistic velocities. © *2005 Pleiades Publishing, Inc.*

Following the basic results obtained by Gaponov and Miller [1, 2], the descriptions of interactions of charged particles with spatially inhomogeneous high-frequency electromagnetic fields frequently employ averaging over the rapid field oscillations in the equations of motion for the charges. This implies that the charges are considered as moving under the action of an averaged Lorentz force. However, in strong fields, the time of flight through a region of inhomogeneous field for a charged particle traveling at a small transit angle is comparable with the period of field oscillations, so that the averaging becomes incorrect. The lifting of limitations with respect to the electric field amplitude makes possible new resonant and nonresonant regimes of interaction. For circularly polarized plane waves, such regimes were described in [3–5]. For a linearly polarized standing wave, the analysis without averaging leads to equations of motion in which the Lorentz force is a function of time. The particles in such a system perform parametric oscillations and encounter (instead of a quasi-potential barrier obtained upon averaging [1, 2]) a barrier dependent on the time (and, hence, on the moment of the particle entrance into the field). The motion of charged particles in a strong field is relativistic.

This paper is devoted to a theoretical analysis of a parametric effect whereby charged particles can perform stable oscillations at the electric field antinode of a standing electromagnetic wave. The oscillations are described in terms of the Hill equation. There are domains in the space of parameters characterizing the field and the moving charges, which correspond to the stable motion of particles. Oscillating at the electric field antinodes, the charged particles can be accelerated by the field to relativistic velocities. Apparently, the motion of charges in a standing electromagnetic wave provides the most effective acceleration regime. The efficiency of other acceleration regimes was considered in [6]. An analysis of the radiation from accelerated particles and their radiative deceleration falls outside of the scope of this paper. All conclusions from the proposed theory were verified by numerical solution of the exact equations of motion. The phenomenon described in this paper is similar to the well-known case of stable oscillations in the upper equilibrium position of a pendulum with oscillating suspension (the Bogoliubov–Kapitza effect).

Let us consider the motion of a particle bearing charge $-e$ in a high-frequency linearly polarized standing field of electromagnetic waves running along the z axis of a Cartesian coordinate system xyz in a nonmagnetic medium. The vector potential of a standing wave is

$$\mathbf{A} = \frac{E_0}{k}\cos(\omega t)\sin(hz)(1, 0, 0), \tag{1}$$

where E_0 is the amplitude of the electric field $\mathbf{E}$, $h = nk$, $k = \omega/c$, and n is the refractive index of the medium. Relativistic equations for the projections of the particle momentum $\mathbf{p} = (p_x, p_y, p_z)$ can be written as

$$\begin{aligned} \frac{dp_x}{dt} &= \frac{e}{c}\frac{dA_x}{dt}, \quad \frac{dp_y}{dt} = 0, \\ \frac{dp_z}{dt} &= -\frac{enE_0}{c}v_x\cos(\omega t)\cos(hz), \end{aligned} \tag{2}$$

where v_x is the particle velocity projection on the x axis. Integrating Eqs. (2) for p_x and p_y with the initial conditions $p_x(t_0) = p_{x0}$, $p_y(t_0) = p_{y0}$, and $z(t_0) = z_0$ and taking

1063-7850/05/3107-0537$26.00 © 2005 Pleiades Publishing, Inc.

into account expression (1) for the wave potential, we obtain

$$p_x = p_{x0} + \frac{eE_0}{\omega}[\cos(\omega t)\sin(hz) - \cos(\omega t_0)\sin(hz_0)],$$
$$p_y = p_{y0}. \quad (3)$$

Substituting these relations and the formulas $\mathbf{v} = c^2\mathbf{p}/W$ and $dW/dt = -(\mathbf{v}, \mathbf{E})$ into Eq. (2) for p_z, we obtain an equation written in the dimensionless form for the coordinate $Z = hz$:

$$\ddot{Z} = \Omega^2(n^{-2}\dot{Z}\sin T\sin Z - \cos T\cos Z) \times (q_x + \cos T\sin Z), \quad (4)$$

where dots over Z denote differentiation with respect to the dimensionless time $T = \omega t$, $\Omega = n\varepsilon/\gamma$ is the ratio of the cyclotron frequency in the magnetic field nE_0 to the field frequency ω, $\varepsilon = eE_0/(m_0c\omega)$ is the electric field parameter, m_0 is the rest mass of the charged particle, $\gamma = (1 - v^2/c^2)^{-1/2}$ is the relativistic factor, $v = |\mathbf{v}|$, and q_x is a constant parameter. The latter parameter in Eq. (4) is given by the formula

$$q_x = \frac{\gamma_0\beta_{x0}}{\varepsilon} - \sin Z_0\cos T_0, \quad (5)$$

where zero subscripts refer to the initial values (taken at $T = T_0 = \omega t_0$) of the relativistic factor (γ_0), the coordinate ($Z_0 = hz_0$), and the velocity projection on the x axis ($\beta_{x0} = v_{x0}/c$).

Using expressions (3), we obtain equations for the dimensionless coordinates $X = h(x - x_0)$ and $Y = h(y - y_0)$:

$$\dot{X} = \Omega(q_x + \cos T\sin Z), \quad \dot{Y} = q_y\Omega, \quad (6)$$

where $q_y = \gamma_0\beta_{y0}/\varepsilon$, $\beta_{y0} = v_{y0}/c$, and v_{y0} is the initial velocity projection on the y axis.

Finally, differentiating Ω (which is inversely proportional to the particle energy) with respect to T and taking into account relations (3), we obtain the equation

$$\dot{\Omega} = n^{-2}\Omega^3(q_x + \cos T\sin Z)\sin T\sin Z. \quad (7)$$

The system of equations (4), (6), and (7) has to be solved with the following initial conditions: $T = T_0$, $Z = Z_0$, $X = Y = 0$, $\Omega = \Omega_0 = n\varepsilon/\gamma_0$.

Let us substitute $Z = Z_1 - \pi/2$ in Eqs. (4), (6), and (7), thus placing the origin at the antinode of the electric field. The initial system of equations is nonlinear in Z, but we can obtain a system linearized with respect to Z_1 by using an approximation of $\sin Z \approx 1$, $\cos Z \approx -Z_1$, which is valid at the antinode of the electric field. As a result, we obtain a system of equations of motion that is linear with respect to the coordinates:

$$\ddot{Z}_1 = \Omega^2(Z_1\cos T + n^{-2}\dot{Z}_1\sin T)(q_x + \cos T),$$
$$\dot{X} = \Omega(q_x + \cos T), \quad (8)$$
$$\dot{Y} = q_y\Omega, \quad \dot{\Omega} = n^{-2}\Omega^3\sin T(q_x + \cos T),$$

where $q_x = n\beta_{x0}/\Omega_0 - \cos T_0$. The initial conditions are as follows: $T = T_0$, $Z_1 = X = Y = 0$, $\Omega = \Omega_0$.

Integrating the equation for Ω in system (8), we obtain

$$\frac{1}{\Omega^2} = \frac{1 - \beta_{x0}^2}{\Omega_0^2} + \frac{(q_x + \cos T)^2}{n^2}. \quad (9)$$

Substituting this expression into the equation for Z_1 in system (8), we arrive at a linear equation with periodic coefficients:

$$\ddot{Z}_1 + p_1(T)\dot{Z}_1 + p_2(T)Z_1 = 0, \quad (10)$$

where

$$p_1(T) = -n^{-2}\sin T(q_x + \cos T)\Omega^2,$$
$$p_2(T) = -\cos T(q_x + \cos T)\Omega^2.$$

Using the well-known substitution

$$Z_1 = Z_2e^{-0.5\int p_1 dT} = \frac{Z_2}{\sqrt[4]{a + (q_x + \cos T)^2}}, \quad (11)$$

where $a = n^2(1 - \beta_{x0}^2)/\Omega_0^2$, we exclude the first derivative from Eq. (10) and obtain the Hill equation:

$$\ddot{Z}_2 + p(T)Z_2 = 0, \quad (12)$$

where

$$pT = p_2(T) - \frac{1}{4}p_1^2(T) - \frac{1}{2}\dot{p}_1(T)$$
$$= \frac{1}{2}\frac{(1 - 2n^2)(q_x + \cos T)\cos T - \sin^2 T}{a + (q_x + \cos T)^2} \quad (13)$$
$$+ \frac{3}{4}\frac{(q_x + \cos T)^2\sin^2 T}{[a + (q_x + \cos T)^2]^2}$$

is a periodic function of T with three parameters (n, a, and q_x).

The stability of a trivial solution of Eq. (12) was determined using the well-known method [7] based on

the characteristic Lyapunov exponent A for this equation. The values of functions forming the fundamental system of solutions of Eq. (12) at $T = 2\pi$, which are necessary for the calculation of A, were determined by numerical methods. Figure 1 shows a diagram of the stability of the trivial solution of Eq. (12) for $n = 1$ and $a \geq 0$, where the coordinates of points in the cross-hatched regions give the values of parameters $a = (1 - \beta_{x0}^2)\gamma_0^2/\varepsilon^2$ and $q_x = \beta_{x0}\gamma_0/\varepsilon - \cos T_0$ that ensure stability. Figure 2 shows a part of this diagram in the region of small a values on a greater scale. Equations (12) and (13) remain unchanged upon the replacement of q_x by $-q_x$ and T by $T + \pi$, which implies that the domains of stability are arranged symmetrically with respect to the a axis. As can be seen, there are four such domains. Assuming that the particle initially (at $T = T_0$) possessed the maximum velocity component along the x axis, we can put $(1 - \beta_{x0}^2)\gamma_0^2 \simeq 1$ and, hence, $a \simeq 1/\varepsilon^2$. Therefore, small a values correspond to the case of strong electric fields (large ε values).

Let us consider how to use the stability diagram depicted in Figs. 1 and 2. The two parameters, a and q_x, are expressed via four physical quantities: β_{x0}, γ_0, ε, and T_0. Since $|\cos T_0| \leq 1$, the parameter q_x obeys the following inequalities:

$$\frac{\beta_{x0}\gamma_0}{\varepsilon} - 1 \leq q_x \leq \frac{\beta_{x0}\gamma_0}{\varepsilon} + 1. \qquad (14)$$

Taking the initial particle velocity component along the x axis (β_{x0}), the initial particle energy (γ_0), and the electric field strength (ε), we calculate the boundary conditions (14) and evaluate the parameter a. For this a value, we determine the intervals of q_x falling within the lower ($q_x < 0$) and upper ($q_x > 0$) cross-hatched regions and simultaneously obeying conditions (14):

$$q_{x,\min}^{(1,2)} \leq q_x \leq q_{x,\max}^{(1,2)}. \qquad (15)$$

Note that the boundary conditions in the lower ($q_{x,\min}^{(1)}$, $q_{x,\max}^{(1)}$) and upper ($q_{x,\min}^{(2)}$, $q_{x,\max}^{(2)}$) regions may occur both inside and on their boundaries. Substituting the expression for q_x into conditions (15), we obtain trigonometric inequalities

$$\frac{\beta_{x0}\gamma_0}{\varepsilon} - q_{x,\max}^{(1,2)} \leq \cos T_0 \leq \frac{\beta_{x0}\gamma_0}{\varepsilon} - q_{x,\min}^{(1,2)}, \qquad (16)$$

which determine the intervals of entrance angles T_0 corresponding to stable motion along the z axis.

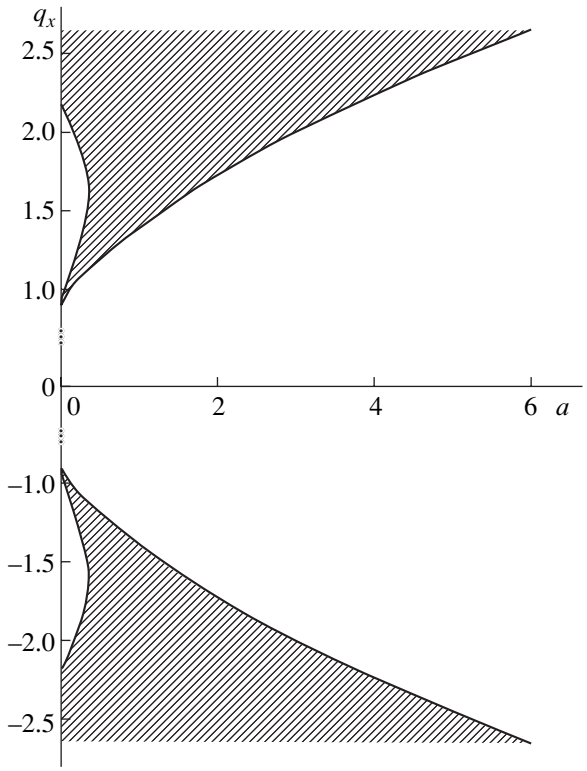

Fig. 1. A diagram of stability of the trivial solution of Eq. (12).

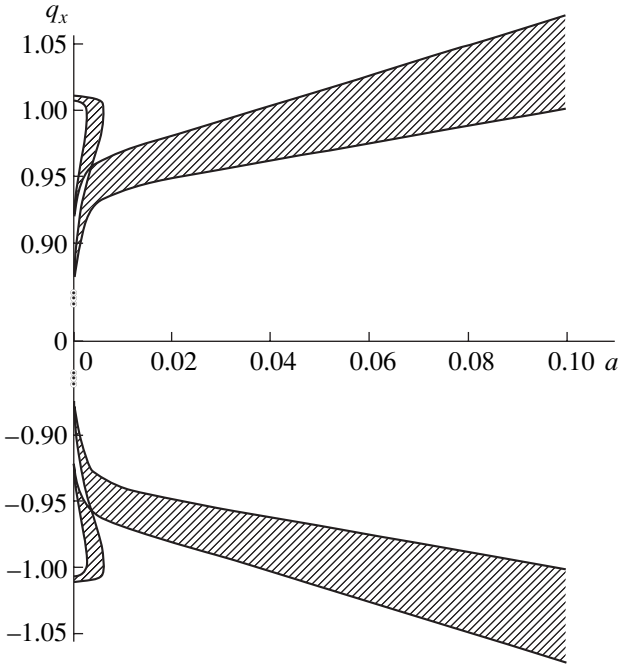

Fig. 2. A part of the diagram of Fig. 1 showing the domains of stability in the region of small a values on a greater scale.

Note that, if both boundary values in conditions (14) fall within the same cross-hatched region in Figs. 1 and 2, the values of $q_{x,\min}$ and $q_{x,\max}$ in (15) coincide with these values, and inequalities (16) yield the condi-

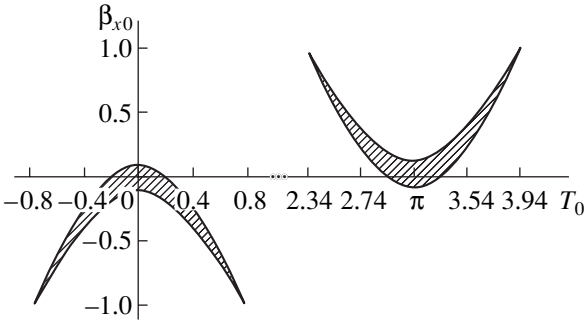

Fig. 3. Example of stability domains for the parameters β_{x0} and T_0 (cross-hatched) for $\varepsilon/\gamma_0 = 4$.

tion $-1 \le \cos T_0 \le 1$, implying that the motion is stable for all entrance angles. This situation takes place, for example, when $a = (1 - \beta_{x0}^2)\gamma_0^2/\varepsilon^2 = 1$ and $\beta_{x0}\gamma_0/\varepsilon = \pm 5/2$, which yields $\beta_{x0} = \pm 5/\sqrt{29}$ and $\varepsilon/\gamma_0 = 2/\sqrt{29}$. If both boundary values in conditions (14) fall outside the cross-hatched regions in Figs. 1 and 2 and the interval (14) does not contain points from these regions, the stable motion is impossible irrespective of T_0. This situation takes place, for example, when $a = 2$, $\beta_{x0}\gamma_0/\varepsilon = \pm 1/2$, which yields $\beta_{x0} = \pm 1/3$ and $\varepsilon/\gamma_0 = 2/3$. In the case $\beta_{x0} = 0$, inequalities (14) yield $-1 \le q_x \le 1$ and the diagram in Fig. 2 shows that the stable motion is possible for $a \le 0.095$, that is, for $\varepsilon/\gamma_0 \ge 3.2$.

Figure 3 presents an example of stability domains for the parameters β_{x0} and T_0 (cross-hatched) constructed for $\varepsilon/\gamma_0 = 4$ using Eqs. (14)–(16) and Fig. 2, which are periodically repeated along the T_0 axis. As can be seen, the motion confined at the electric field antinode is possible for the particles whose entrance moments fall within certain intervals in the vicinity of $T_0 = s\pi$ ($s = 0, 1, \ldots$).

The wavelength λ and the electric field strength E_0 for electrons is conveniently estimated using the formula

$$\varepsilon = 3.1 \times 10^{-2} E_0 \left[\frac{\text{kV}}{\text{cm}}\right] \lambda[\text{m}].$$

Relation (9) yields an expression for the particle energy gained during the motion at the electric field antinode of a standing wave:

$$\gamma = \gamma_0 \left\{1 - \beta_{x0}^2 + \left[\beta_{x0} + \frac{\varepsilon}{\gamma_0}(\cos T - \cos T_0)\right]^2\right\}^{\frac{1}{2}}. \quad (17)$$

As can be seen from this formula, the charges remaining at the electric field antinode (i.e., at the maximum field strength) are periodically accelerated in phase with the field oscillations in time. The maximum energy (under otherwise equal conditions) is gained by the particles entering at $T_0 = s\pi$ ($s = 0, 1, \ldots$), that is, when the electric field is zero. The electric force acting on these particles retains its direction for the maximum period of time, equal to half of the period of field oscillations (π), after which the force direction changes to the opposite and the particles are decelerated. The energy of accelerated particles can be significant: for $\varepsilon/\gamma_0 \gg 1$ (strong field), we have $\gamma \simeq 2\varepsilon \gg 1$.

Using equations (8) for the particle velocity components $\dot{X}$ and $\dot{Y}$, we obtain

$$\beta_x = \frac{v_x}{c} = \frac{\beta_{x0}\gamma_0 + \varepsilon(\cos T - \cos T_0)}{\gamma},$$

$$\beta_y = \frac{v_y}{c} = \frac{\beta_{y0}\gamma_0}{\gamma},$$

where γ is given by formula (17). These relations show that, as expected, the charged particles are predominantly accelerated along the field (i.e., along the x axis). The oscillating charges drift in the $x0y$ plane.

REFERENCES

1. A. V. Gaponov and M. A. Miller, Zh. Éksp. Teor. Fiz. **34**, 242 (1958) [Sov. Phys. JETP **7**, 168 (1958)].
2. M. A. Miller, Izv. Vyssh. Uchebn. Zaved., Radiofiz. **1**, 110 (1958).
3. A. F. Kurin and E. A. Kurin, Zh. Tekh. Fiz. **63** (7), 55 (1993) [Tech. Phys. **38**, 560 (1993)].
4. A. F. Kurin, Zh. Tekh. Fiz. **64** (8), 14 (1994) [Tech. Phys. **39**, 754 (1994)].
5. A. F. Kurin, Izv. Vyssh. Uchebn. Zaved., Radiofiz. **46**, 52 (2003).
6. G. A. Askar'yan, Zh. Éksp. Teor. Fiz. **36**, 619 (1959) [Sov. Phys. JETP **9**, 430 (1959)].
7. V. A. Yakubovich and V. M. Starzhinskii, *Linear Differential Equations with Periodic Coefficients* (Nauka, Moscow, 1972; Wiley, New York, 1975).

Translated by P. Pozdeev

Technical Physics Letters, Vol. 31, No. 7, 2005, pp. 541–544. Translated from Pis'ma v Zhurnal Tekhnicheskoĭ Fiziki, Vol. 31, No. 13, 2005, pp. 10–17.

Microchannel Edge Formation in Laser-Ablated Polyimide

A. A. Evstrapov*, A. O. Pozdnyakov, S. G. Gornyĭ, and K. V. Yudin

Institute for Analytical Instrumentation, Russian Academy of Sciences, St. Petersburg, 198103 Russia

Laser Center Company, St. Petersburg, Russia

** e-mail: evstra@iai.rssi.ru*

Received February 25, 2005

Abstract—Microchannels in polyimide (PI) have been produced by means of laser ablation (LA). The obtained results confirm the possibility of using the LA technology for the functional structure formation on PI-based microfluidic chips (MFCs). The shape of the channel edge may depend on the thermal properties of PI. This circumstance makes it possible to optimize the process of MFC fabrication by selecting a proper PI and the corresponding LA regime. Optimization of the other characteristics, such as mechanical properties and planarity of the MFCs, requires additional investigations. © *2005 Pleiades Publishing, Inc.*

Micro- and nanodimensional patterns are important elements of modern analytical microfluidic devices [1]. Such devices make possible the manipulations with microscopic amounts of substances, including the supply and dosage of picoliter samples, their stirring and mixing with other reagents, conducting chemical reactions, and the detection and fractionation of the reaction products [2]. An important component of any microfluidic device is the microfluidic chip (MFC). Until recently, MFCs were typically based on quartz and silicon [3]. The relatively low cost of polymeric materials and the possibility of large-scale commercial production of polymer-based MFCs make these materials highly attractive. Methods for the fabrication of microfluidic channel (microchannel) patterns in polymeric substrates, such as mechanical embossing and the formation of temporal spacers (removed upon complete MFC structure formation) have been developed. These techniques can be successfully applied to polymers possessing low heat resistance [4–6]. It can be expected that the possibility of burning out channels in polymers stable at elevated temperatures, such as polyimide (PI), by means of laser ablation (LA) would provide for the formation of microchannels at a much higher rate. Our analysis of the available literature showed that this question, despite its evident importance, is practically unstudied. The formation of MFC channels using low-cost IR lasers offers the most expedient (technically and economically justified) solution of problems related to the development of polymer-based MFC structures.

This Letter presents the result obtained in the first stage of our experiments devoted to the development of the LA of PIs in the IR range for fabricating MFCs with microchannels possessing the optimum edge shape.

The PI coatings were prepared from two polyamic acids (PAAs) as prepolymers. The first PAA was synthesized from 3,3',4,4'-oxydiphthalic anhydride (ODPA), *p*-phenylenediamine (PPD), and 2,5-bis(4-aminophenyl)pyrimidine (APP). In some experiments, we used the coatings prepared from ODPA–PPD–APP suspensions with C_{60} fullerene additives. The synthesis of ODPA–PPD–APP prepolymer and the preparation of suspensions containing C_{60} fullerene are described in detail elsewhere [7]. The second PAA was a commercial lacquer of the AD-9103 grade (State Standard TU-6-19-247–84), which is a product of the interaction between pyromellitic dianhydride and 4,4'-diaminodiphenyl oxide. The PAA layers were cast onto the surface of K-8 glass substrates and leveled with a glass spatula so as to obtain a uniform ~60-μm-thick layer. Prior to the polymer application, the substrate surface was thoroughly degreased with acetone. After application, the samples with PAA layers were dried for several hours at ~40°C in vacuum (~700 mbar). Finally, the PAA layer was subjected to thermal imidization by heating in vacuum (~700 mbar) to ~360°C at a rate of ~2 K/min. The PI coatings were prepared in a VT6060T vacuum furnace (Kendro Laboratory Products, Germany).

The microchannel patterns in PI coatings were formed using a commercial setup of the Speedy II type (TROTEC Co., USA) equipped with an IR laser (quasi-cw CO_2 laser, $\lambda = 10.6$ μm, Synrad, USA) operating at an output power of $W = 1$, 1.25, 1.75, 2.5, or 3.75 W. The laser beam was scanned over the sample surface at a velocity of 6 mm/s and computer-controlled to form a microchannel pattern with a resolution of up to 1000 dpi. The system software allowed the laser beam scan regime to be controlled online, which made it possible to introduce corrections into the microchannel topology. The obtained structures were examined and characterized with the aid of a Leica NCS SL confocal scanning laser microscope (Leica, Germany). The measurements were performed in the reflection mode at a probing laser beam wavelength of 458 nm.

1063-7850/05/3107-0541$26.00 © 2005 Pleiades Publishing, Inc.

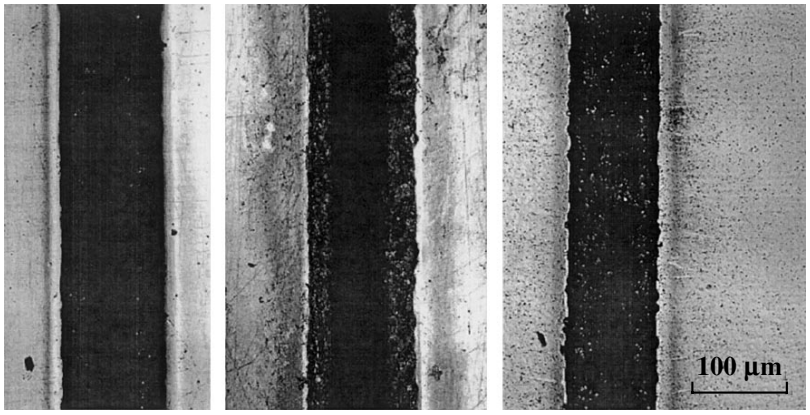

Fig. 1. Micrographs of the channels obtained in (a) PM, (b) ODPA–PPD–APP, and (c) ODPA–PPD–APP/C_{60} coatings by LA at a laser power of 1.25 W and a beam scan velocity of 6 mm/s.

Figure 1 shows micrographs of the typical channels obtained in PM, ODPA–PPD–APP, and ODPA–PPD–APP/C_{60} coatings by LA at a laser power of 1.25 W and a beam scan velocity of 6 mm/s. As can be seen, the channel edges in the PM matrix are much smoother than those in ODPA–PPD–APP and ODPA–PPD–APP/C_{60}. The channel edge had an analogous appearance for all output laser powers. The channel width in ODPA–PPD–APP/C_{60} is somewhat narrower than in PM and ODPA–PPD–APP. One of the most important requirements to MFC channels is to provide for a laminar flow of liquids. This, in turn, predetermines the restrictions imposed on the microrelief (roughness) of the surface and the uniformity of the channel along its length. The obtained results showed that the LA channels formed in PM meet all these requirements. The characteristics of microchannels obtained in our experiments (width, 100–200 μm; depth, 10–50 μm; trapezoidal profile; satisfactory microrelief), allow the proposed technology to be used for the fabrication of various functional devices on MFCs (such as transport and separatory channels, mixers, etc.).

In view of the important role of the channel geometry, it is necessary to select the appropriate criteria for evaluating the MFC channels in this respect. Within the framework of fractal concepts [8], the edge line length L can be measured using segments of characteristic length d. By using a plot of $\log L$ versus $\log d$, it is possible to determine the fractal dimension D of the channel edge. This parameter enters into the relation $L(d) = L_0 d^{(1-D)}$, where L_0 is the length of a nonfractal curve. We have processed the micrographs in Fig. 1 so as to determine the fractal dimension of the microchannel edge, which has proved to be $D \sim 1$ for the channels in PM and $D > 1.05$ for the channels in ODPA–PPD–APP and ODPA–PPD–APP/C_{60}. Since the fractal dimension can be an important quantitative characteristic of the MFC channel edge, this parameter is worth more detailed investigation.

Figure 2 shows plots of the channel width b versus laser power W for various matrices processed by LA at a constant beam scan velocity of 6 mm/s. A comparison of the $b(W)$ curves confirms the conclusions derived from the analysis of micrographs (Fig. 1), according to which the channel width in ODPA–PPD–APP/C_{60} is somewhat narrower than in pure ODPA–PPD–APP and PM. As can be seen from Fig. 2, an increase in the laser power leads to a growth of the channel width. At $W \sim 1.25$ W, the $b(W)$ curve deviates from monotonic growth, which can be naturally explained by a change in the conditions of laser radiation absorption and thermal conductivity at the moment of complete burning out of the polymer layer, that is, when the laser beam

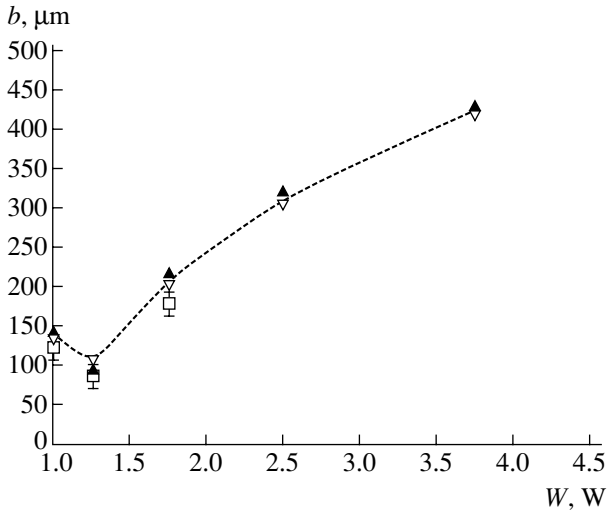

Fig. 2. Plots of the channel width b versus laser power W for (▲) PM, (▽) ODPA–PPD–APP, and (□) ODPA–PPD–APP/C_{60} matrices processed by LA at a constant beam scan velocity of 6 mm/s.

strikes the surface of the glass substrate. An analysis of the channel relief showed that LA channels at a power below ~1.25 W are formed within the polymer layer, while the LA at $W > 1.25$ burns out the polymer layer down to the substrate. In the former case, the channel has the shape of a round cylinder, whereas, in the latter case, the channel is almost rectangular.

Using the obtained experimental data, it is possible to evaluate some energy characteristics of our LA experiments. Within the framework of the threshold model, a polymer is removed by LA when the absorbed energy exceeds a certain threshold. Therefore, the channel edge is the site where the incident energy density E is approximately equal to the threshold energy density ε. For a given scan velocity v, laser beam diameter a, and laser power W, the incident energy can be evaluated using the formula $E = Wa/(Sv)$, where S is the effective area of the beam–surface interaction. In our experiments, the incident power was determined at a half-height of the Gaussian laser beam intensity profile. Therefore, the S value can be estimated with sufficient accuracy as $S = a^2$. Calculations performed assuming a Gaussian profile and continuous radiation and using the channel width obtained at $W = 1$ W (corresponding to complete burning out of the polymer layer) gave $\varepsilon \sim 2.3$ J/cm^2 for PM and ODPA–PPD–APP and a somewhat greater value (~5 J/cm^2) for ODPA–PPD–APP/C_{60}, which is indicative of an increase in the LA energy threshold for the fullerene-doped PI. It is important to note that the shape of the channel edge in the fullerene-doped PI is almost the same as that in the pure PI. This result indicates that fullerene virtually does not influence the heat resistance of the polymer matrix, but it can somewhat increase its thermal stability. The mechanism of this influence is still unclear.

A strong absorption of IR radiation by the PM matrix (see, e.g., the data for Kapton™ [9], which is analogous to our PM) takes place at a wavelength of ~9.2 μm. According to the same data [9], the absorption at a wavelength of 10.6 μm used in our study is significantly lower. This is naturally explained by a higher LA energy threshold of ~2.1 J/cm^2 [9] at this wavelength. This value is in good agreement with our experimental estimate of $\varepsilon \sim 2.3$ J/cm^2. It should be noted that the value reported in [9] was observed both for freestanding Kapton™ films with a thickness of about 70 μm and for ~5-μm-thick coatings on silicon.

According to the IR spectroscopy data [10], the level of IR absorption in ODPA–PPD–APP at 10.6 μm is also relatively low (intense absorption in this PI is observed above 1050 cm^{-1}). Taking into account the comparable coefficients of transmission and reflection in the given experimental geometry, we may conclude that the ε values for PM and ODPA–PPD–APP are also practically identical. Under a reasonable assumption that the thermal conductivities of all PIs used in this study are close to each other, the LA channel edge formation is probably determined by polymer heating in the regions where $E \sim \varepsilon$. Then, the different response of polymers to laser-induced heating, which is manifested by the less smooth channel edge in ODPA–PPD–APP as compared to that in PM, can be explained by the fact that ODPA–PPD–APP in the region where $E < \varepsilon$ (i.e., outside the LA channel) is somewhat softened, albeit not removed, under the laser action. Taking into account the close thermal stabilities of ODPA–PPD–APP and PM, this mechanism influencing the channel edge formation is confirmed by the existence of a softening point ($T_s \sim 320$°C [10]) in the case of ODPA–PPD–APP. The passage of a beam scanned at a preset rate may result in subsequent overcooling of the softened polymer regions and fixing of the corresponding polymer structure. At a given scan velocity (6 mm/s), the time τ required for the laser beam to travel a distance comparable with the beam diameter (~50 μm) is about 0.1 s. Taking in to account the low thermal conductivity of PI ($D \sim 10^{-7}$ m^2/s), we can estimate the characteristic linear size of the near-edge region featuring thermal flows as $x = \sqrt{D\tau}$, which yields a value on the order of ~100 μm. This value is significantly greater than the characteristic linear size of inhomogeneities of the channel edge (~1 μm) and than the polymer layer thickness (~50 μm). On the one hand, this result is evidence for the local character of processes involved in the edge formation. On the other hand, it is still possible that the edge formation may be influenced by temperature variations in the large (compared to the characteristic size of the channel edge inhomogeneities) regions in the substrate plane, for which $E < \varepsilon$. Apparently, this effect determines, to a certain extent, the inhomogeneity of PI regions outside the channel (Fig. 1) over distances significantly greater than the characteristic size of the channel edge inhomogeneities. This behavior is naturally explained by a decrease in the polymer temperature with increasing distance from the channel edge in the course of LA.

One possible reason for a decrease in the mobility of macromolecules (which might account for the absence of softening in the regions where $E < \varepsilon$) can be the presence of various crosslinks in the polymer structure. The electron-acceptor properties of fullerene molecules make them capable of interacting with the electron-donor fragments of macromolecules (such as, e.g., the terminal amino groups of PAA) and participating in complicated reactions accompanying the decomposition of polymers. Apparently, these effects can be determined to a considerable extent by the degree of dispersion of the given molecular filler in the polymer matrix [7]. A more thorough investigation and optimization of the LA channel shape through variation of the physicochemical properties of PI and its components is currently in progress.

Acknowledgments. This study was supported by the Russian Foundation for Basic Research (project 03-01-39003GFENa) and the Federal Program "Investigations in Selected Directions of Science and Tech-

nology 2002–2006" (project 10, "Development of Equipment Set for Chemical Microanalysis").

The authors are grateful to the managers of Leica company for help in restoration of the confocal scanning laser microscope used in this study.

REFERENCES

1. *Proceedings of the 7th International Conference on Micro Total Analysis Systems, Squaw Valley, 2003*, Ed. by M. Allen Northrup, Klavs F. Jensen, and D. Jed Harrison, Vols. 1–2.
2. L. Carey and L. Mitnik, Electrophoresis **23**, 1386 (2002).
3. L. Lichtenberg, E. Verpoorte, and N. F. Rooij, Electrophoresis **22**, 258 (2001).
4. A. Gerlach, G. Knebel, A. E. Guber, *et al.*, Microsyst. Technol. **7**, 265 (2002).
5. L. Martynova, L. E. Locascio, M. Gaitan, *et al.*, Anal. Chem. **69**, 4783 (1997).
6. S. Metz, R. Holzer, and F. Renaud, Lab on a Chip **1**, 29 (2001).
7. A. O. Pozdnyakov, B. M. Ginzburg, T. A. Maricheva, *et al.*, Fiz. Tverd. Tela (St. Petersburg) **46**, 1328 (2004) [Phys. Solid State **46**, 1371 (2004)].
8. B. B. Mandelbrot, *The Fractal Geometry of Nature* (Freeman, San Francisco, 1982; RKhD, Izhevsk, 2002).
9. J. H. Brannon and J. R. Lankard, Appl. Phys. Lett. **48**, 1226 (1986).
10. A. O. Pozdnyakov, V. V. Kudryavtsev, and K. Friedrich, Wear **254**, 501 (2003).

Translated by P. Pozdeev

Technical Physics Letters, Vol. 31, No. 7, 2005, pp. 545–547. Translated from Pis'ma v Zhurnal Tekhnicheskoĭ Fiziki, Vol. 31, No. 13, 2005, pp. 18–23.

On the Possibility of Controlling the Motion of Spiral Waves in a Two-Dimensional Lattice of Excitable Elements with the Aid of Topological Defects

K. V. Andreev and L. V. Krasichkov

Saratov State University, Saratov, Russia

e-mail: kandreev@cas.ssu.runnet.ru; lvk@cas.ssu.runnet.ru

Received February 25, 2005

Abstract—Autowave dynamics in a two-dimensional lattice of excitable elements of the FitzHugh–Nagumo type containing topological defects has been studied. It is shown that the core of a spiral wave can drift along a path composed of such defects. The possibility of controlling the motion of spiral waves in excitable and oscillating media is considered. *© 2005 Pleiades Publishing, Inc.*

Autowave behavior is frequently encountered in nonlinear active media of various natures [1, 2]. In particular, autowaves can appear in physical (liquids in oscillating gravitational field, lattices of Josephson junctions), chemical (Belousov–Zhabotinsky reactions in Petri dish), and biological systems (spiral waves in the cerebral core of humans and animals [3], self-sustained waves in muscle tissues). In view of the universal character of such autowave phenomena, it is a currently important task to study and develop methods for the control of spatiotemporal dynamics in systems exhibiting autowave behavior.

This Letter presents the results of investigations of the possibility of controlling the motion of spiral waves with the aid of topological defects. As is known [1], the core of a spiral wave moving in a nonlinear active media exhibits a drift, and this drift can be either regular or nonregular. In an excitable medium, such a core occurring near a topological defect can be trapped by this defect, after which the spiral wave will rotate around it. Krinsky *et al.* [4] used the Barkley model [5] to show that the core of a spiral wave can move in a medium behind an exciting electrode, which introduces a perturbation at a given point of the medium.

Previously, we studied [6, 7] a two-dimensional (2D) lattice of piecewise-linear maps [8] qualitatively describing the dynamics of neurons. It was demonstrated that the core of a spiral wave could be driven to move along a chain composed of point defects. The effect was substantially new and had never been reported previously, but the system in which this phenomenon took place was discrete with respect to both temporal and spatial coordinates. In addition, the medium studied in [6, 7] was autooscillatory. In this context, it was of interest to consider the possibility that the core of a spiral wave would also move along a chain composed of defects in a classical model of an excitable medium.

As was mentioned above, the model used previously [6, 7] was intended for the description of the spatiotemporal dynamics of neuron lattices. By analogy, we decided to consider the excitable medium as a lattice of elements modeled by the FitzHugh–Nagumo system [9, 10]. This model describes the propagation of electric pulses in a nerve fiber, which is the classical example of an excitable medium [1, 2]. In the case of a 2D lattice, the model can be described by a system of equations:

$$\begin{cases} \dfrac{dx_{i,j}}{dt} = \dfrac{1}{\varepsilon}\left(-\dfrac{1}{3}x_{i,j}^3 + x_{i,j} - y_{i,j}\right) + I_{i,j}, \\ \dfrac{dy_{i,j}}{dt} = x_{i,j} - ay_{i,j} + b, \end{cases} \quad (1)$$

where $i, j = 1, 2, \ldots, N$ (we have simulated a 2D lattice with $N = 100$); a, b, and ε are constant parameters (identical for all elements of the lattice); and the term $I_{i,j}$ describes the interaction between the lattice elements. The interaction term can be written as

$$I_{i,j} = D(x_{i-1,j} + x_{i+1,j} + x_{i,j-1} + x_{i,j+1} - 4x_{i,j}), \quad (2)$$

where D is the degree of coupling between elements (we take into account the coupling with only four nearest neighbors). The simulation was carried out using the condition of zero total flux on the boundaries.

Generally speaking, the problem posed by Eqs. (1) and (2) can be considered as a numerical scheme for solving a set of differential equations in partial derivatives describing a continuous excitable medium [2].

1063-7850/05/3107-0545$26.00 © 2005 Pleiades Publishing, Inc.

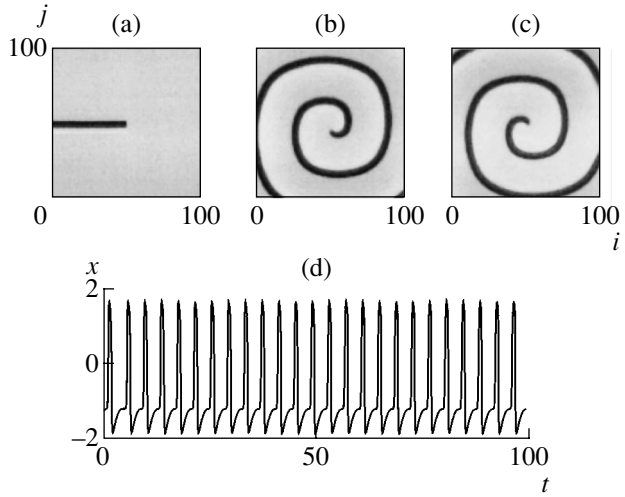

Fig. 1. Dynamics of the state variable amplitude for a lattice of elements modeled by the FitzHugh–Nagumo system corresponding to Eqs. (1) and (2) with $a = 1$, $b = 0.55$, $\varepsilon = 15$, and $D = 5$: (a) initial distribution of the oscillation amplitude in the form of a broken wave front; (b, c) instantaneous distributions in a propagating solitary spiral wave; (d) typical time series of the state variable x.

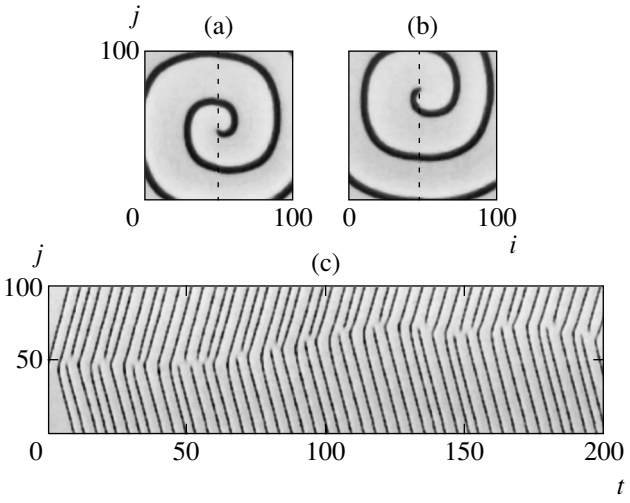

Fig. 2. Dynamics of the state variable amplitude for a lattice of elements modeled by the FitzHugh–Nagumo system corresponding to Eqs. (1) and (2) with $a = 1$, $b = 0.55$, $\varepsilon = 15$, and $D = 5$: (a, b) instantaneous distributions in a solitary spiral wave moving along the line $i = 50$ containing point defects (indicated by black points) spaced by four lattice elements; (c) the typical spatiotemporal diagram constructed for a column with $i = 48$ using distributions (a) and (b).

However, if we restrict the consideration to the dynamics of an ensemble of neurons, the medium should be considered as substantially discrete.

As is known [2], a model system described by Eqs. (1) and (2) can feature autowave phenomena. In order to excite a solitary spiral wave, it is necessary to set the initial conditions in the form of a broken wave front such as depicted in Fig. 1a. Figures 1b and 1c show an example of the spatiotemporal lattice dynamics in the case of propagation of a solitary spiral wave. The typical time series observed for an individual lattice element is presented in Fig. 1d.

A model point defect occurring at the lattice site with the coordinates (i, j) is considered as an element isolated from the lattice. Such an element does not influence the neighboring sites, and, hence, its own dynamics presents no interest.

Let us consider the behavior of a solitary wave on the model lattice containing topological defects. If the defects are of the point type and are randomly distributed over the lattice, the spiral wave will not be destructed provided that the number of defects is relatively small (about several percents of the total number of lattice sites). In the course of evolution of the system, the core of the spiral wave exhibits drift and may approach one of the point defects. As a result, the core will be trapped by this defect. It should be noted that the motion of the core of a spiral wave around a topological defect also takes place for defects of other types.

Now let us assume that a solitary spiral wave is formed and the point defects are arranged so as to form a "path" passing near the core of the wave (Fig. 2a). In this case, the core will be trapped by one of these point defects. If the distance between defects is relatively short, the trapped core will travel between the adjacent defects rather than "stick" to a certain trap. Thus, it is possible to drive the spiral wave so that it will move along the path composed of the point defects (Figs. 2b and 2c). Apparently, a sufficiently large distance between defects will make this motion impossible. The results of our numerical simulations showed that, for the given parameters of the system of Eqs. (1) and (2), the maximum separation of defects at which the drift of the core is still possible amounts to six lattice elements. We may assume that this value is determined by the core diameter and changes depending on the system parameters.

The direction and velocity of motion of the core of a solitary wave can be evaluated using spatiotemporal diagrams constructed for a lattice column adjacent to the column with defects. Since the lattice oscillations inside the core of the spiral wave are absent (and the amplitude of oscillations of the elements near the core is significantly lower than that of the other elements), the core leaves a bright-gray trace on the spatiotemporal diagram (Fig. 2c). Using the slope of this trace, it is possible to determine the drift direction and average velocity for the core of a spiral wave.

In conclusion, we have demonstrated that a characteristic feature of the interaction of a spiral wave with point defects on a lattice of piecewise-linear maps, whereby the core of the wave drifts along the path of defects, also takes place in the classical model of an excitable medium described by the FitzHugh–Nagumo system. The observed effect opens ways to control the motion of spiral waves by introducing point defects into

the lattice. By virtue of the universality of autowave phenomena, the obtained results can be generalized to excitable media of different types.

Acknowledgments. This study was supported in part by the US Civilian Research and Development Foundation (grant BRHE REC-006).

REFERENCES

1. A. Yu. Loskutov and A. S. Mikhaĭlov, *Foundations of Synergetics* (Nauka, Moscow, 1990; Springer, Berlin, 1991).
2. D. I. Trubetskov, E. S. Mchedlova, and L. V. Krasichkov, *Introduction to Theory of Self-Organization of Open Systems* (Fizmatlit, Moscow, 2002) [in Russian].
3. J. C. Prechtl, L. B. Cohen, B. Pesaran, *et al.*, Proc. Natl. Acad. Sci. USA **94**, 7621 (1997).
4. V. Krinsky, F. Plaza, and V. Voignler, Phys. Rev. E **52**, 2458 (1995).
5. D. Barkley, M. Kness, and L. Tuckerman, Phys. Rev. A **42**, 2489 (1990).
6. K. V. Andreev and L. V. Krasichkov, Izv. Ross. Akad. Nauk, Ser. Fiz. **66**, 1777 (2002).
7. K. V. Andreev and L. V. Krasichkov, Izv. Ross. Akad. Nauk, Ser. Fiz. **67**, 1701 (2003).
8. K. V. Andreev and L. V. Krasichkov, Pis'ma Zh. Tekh. Fiz. **29** (3), 46 (2003) [Tech. Phys. Lett. **29**, 105 (2003)].
9. R. FitzHugh, Biophys. J. **1**, 445 (1961).
10. J. Nagumo, S. Arimoto, and S. Yoshizawa, Proc. IRE **50**, 2061 (1962).

Translated by P. Pozdeev

Technical Physics Letters, Vol. 31, No. 7, 2005, pp. 548–550. Translated from Pis'ma v Zhurnal Tekhnicheskoĭ Fiziki, Vol. 31, No. 13, 2005, pp. 24–30.

Nitriding of Technical-Purity Titanium in Hollow-Cathode Glow Discharge

Yu. Kh. Akhmadeev, I. M. Goncharenko, Yu. F. Ivanov, N. N. Koval, and P. M. Schanin

Institute of High-Current Electronics, Siberian Division, Russian Academy of Sciences, Tomsk, 634055 Russia
e-mail: schanin@opee.hcei.tsc.ru

Revised manuscript received March 13, 2005

Abstract—The process of nitriding at low pressures and temperatures (≤550°C) in hollow-cathode glow discharge plasma was studied for technical-purity titanium of the VT1-0 commercial grade. The diffusion saturation of titanium with nitrogen in plasma with a concentration of $n = 10^{10}$–10^{11} cm^{-3} takes place at an ion current density on the cathode within 1.6–4.0 mA/cm^2. It is established that a key role in the process of metal saturation is played by atomic nitrogen. The experiments revealed the formation of a layer of gradient structure with a high microhardness (~14 GPa) on the surface of nitrided titanium. © *2005 Pleiades Publishing, Inc.*

In order to increase the surface hardness and resistance to wear and corrosion of titanium alloys, articles are frequently subjected to saturation with nitrogen (nitriding) by diffusion from the plasma of glow [1–4] or arc discharge [5] or by implantation with nitrogen ion beams [6]. In most cases, the nitriding of titanium is carried out for several hours at high temperatures (800–900°C) and elevated pressures (100–1000 Pa). However, the nitriding of low-doped titanium alloys at high temperatures (above the temperature of the polymorphous $\alpha \Rightarrow \beta$ phase transition) leads to the growth of grains and a change in the microstructure, which detrimentally influence the material performance characteristics. Nitriding at low temperatures (≤550°C) was reported for VT-18U titanium alloy irradiated with nitrogen ion beams (first, at an ion energy of 30 keV and, then, at 300 eV) to a total dose of ~10^{20} cm^{-2} [6], VT-22 alloy exposed to hollow-cathode glow discharge [5], and pure titanium treated in a low-pressure (1 Pa) glow discharge in a triode system ensuring high (up to 4 mA/cm^2) ion current densities on the cathode surface [7].

Although there is no commonly accepted mechanism of the diffusion saturation of titanium with nitrogen, most researchers believe that a determining role in this process, especially at low temperatures, is played by the molecular and atomic nitrogen ions. However, Meletis [7] suggested that a necessary condition for reaching a high hardness in pure titanium articles is that the metal surface should be bombarded, in addition to ions, by high-energy neutrals effectively creating vacancies and defects in the target and, thus, enhancing the diffusion of atomic nitrogen. If the nitriding of titanium is considered as a plasmachemical process, a necessary condition is that the metal saturation with nitrogen must proceed in a plasma containing both N atoms and N^+ ions. This implies that, besides ionization, it is necessary to provide conditions for the maximum dissociation of nitrogen molecules.

The aim of this study was to reveal characteristic features of the nitrogen saturation of technical-purity titanium (commercial VT1-0 grade) in low-pressure glow discharge, to study the formation of the nitrided layer at various sample temperatures and discharge parameters, and to determine the structure and phase composition of the nitrided surface layer.

Figure 1 shows a schematic diagram of the experimental setup. Holder *1*, occurring at the center of a vac-

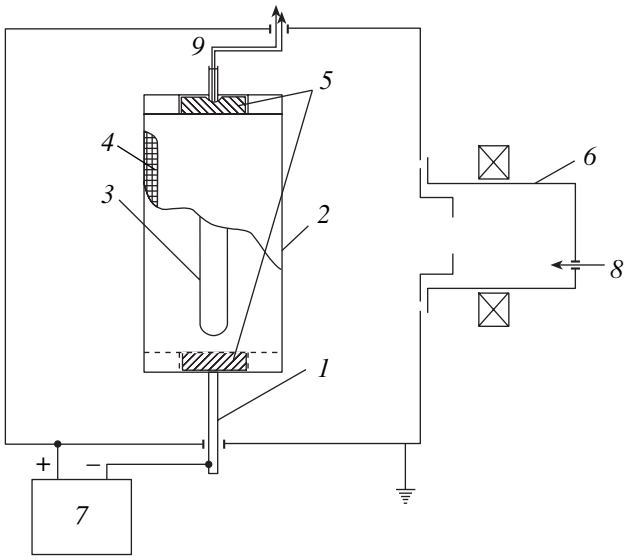

Fig. 1. Schematic diagram of the experimental setup (see the text for explanations).

1063-7850/05/3107-0548$26.00 © 2005 Pleiades Publishing, Inc.

uum chamber, supports a hollow cathode *2* having the shape of a cylinder with a diameter of 80 mm and a length of 120 mm. The side surface of the cylinder has two 100-mm-long windows *3* and *4*, one with a width of 10 mm and another, of 20 mm (closed with a small-mesh grid). The samples *5* (disks with a diameter of 25 mm and a thickness of 5 mm) are mounted flush with the internal end surfaces of the hollow cathode in order to eliminate the cathode layer curvature and to ensure homogeneous ion irradiation. The sample temperature was measured by thermocouple *9*. The hollow cathode was maintained at a negative voltage relative to the anode (chamber), which was provided by a bias voltage source *7*. Additional source *6* (based on a cold hollow-cathode arc discharge [8] created plasma with a concentration controlled within broad limits by means of a variable discharge current. Using this source, it was possible to initiate and maintain the glow discharge in a high-current form even at low gas pressures. Pure nitrogen (N_2) or a working gas mixture (Ar–N_2) were supplied via a gas admission and pressure control system *8* of the gas-discharge plasma source.

The experiments were performed with technical-purity titanium of the VT1-0 commercial grade. The nitriding process was carried out as follows. First, the chamber was filled with argon at a pressure of $P_{Ar} = 4.4 \times 10^{-1}$ Pa, and the hollow cathode surface was cleaned and trained for 10–20 min at a negative bias voltage of U_d = 0–1500 V and a gas-discharge plasma generator current of I_d = 50 A. Then, a working gas (pure nitrogen or a 40% Ar–60% N_2 mixture) was admitted to the working chamber, the required pressure was set by varying the operation rate of a turbomolecular pump, and the glow discharge was initiated. The process of nitriding at various working gas pressures was carried out for 4.5 h at various sample temperatures (450, 550, or 750°C). The structure, phase composition, and mechanical properties of the nitrided material were studied using conventional metallographic techniques (on etched cross sections), scanning and transmission electron microscopy (on brittle cleavages and extracted carbon replicas), and micro- and nanohardness measurements.

Experimental data on the microhardness of the surface of samples treated at various glow discharge parameters and temperatures are presented in the table. These data reveal some trends in the plasmachemical nitriding of titanium. The microhardness grows with increasing ion current density J_i, ion energy (discharge voltage U_d), and sample temperature. The last factor is especially significant: an increase in the temperature by 300°C (from 450 to 750°C) leads to a 2.2-fold growth in the microhardness. The sample surface exposed to the plasma shows evidence of intense etching due to sputtering by ions accelerated in the cathode layer.

It was established that, if the ion access to the rear side of a sample was excluded (so that only atomic and molecular nitrogen species could interact with this side), etching did not take place and the metal surface acquired a golden appearance. At the same time, the microhardness of this surface almost coincided with that of the surface exposed to the plasma. This implies that nitriding proceeds at equal rates on both the front and rear sides of the sample. Nitrogen saturation of the rear side of a sample treated in a glow discharge plasma was also observed in [4].

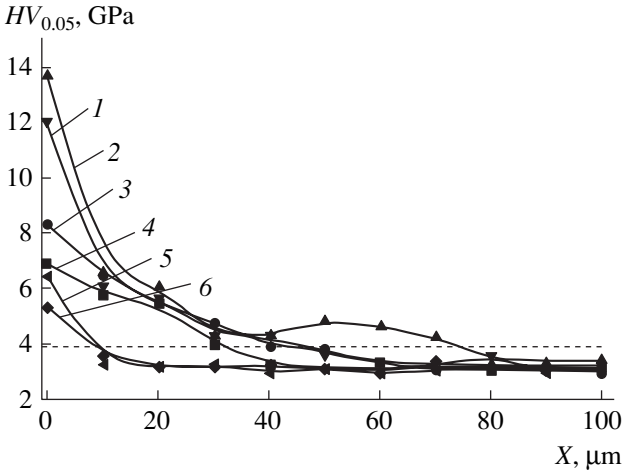

Fig. 2. Microhardness profiles of the (*1*, *3*, *5*) front side and (*2*, *4*, *6*) rear side of a sample of VT1-0 titanium nitrided in a hollow-cathode glow discharge plasma at low pressures and temperatures T = 750 (*1*, *2*), 550 (*3*, *4*), and 450°C (*5*, *6*). The dashed line shows the microhardness measured before the nitriding process.

Figure 2 shows the microhardness profiles of the samples of VT1-0 titanium nitrided at various temperatures. The cures clearly reveal a 50- to 60-μm-thick layer in which the microhardness is significantly increased as compared to that of the initial material. An analysis of the results of nanoindentation showed that the nanohardness of the rear surface was also comparable with that of the front surface. This fact implies that, at high glow discharge voltages, only partial metal etching due to sputtering by ions and fast neutrals (formed as a result of charge transfer) takes place on the front surface exposed to the cathode layer.

The presence of both a nitrided layer and a diffusion saturated layer in VT1-0 titanium treated in the glow discharge was also clearly revealed by the analysis of electron micrographs of the transverse sections formed

Dependence of the microhardness of technical-purity titanium (VT1-0 grade) on the conditions of nitriding in glow discharge plasma

P, Pa	T, °C	U_d, kV	J_i, mA/cm^2	HV, GPa	HV/HV_0
3.9	750	1.4	4.0	14	4.7
2.8	550	1.4	3.9	8.2	2.7
2.1	450	1.0	1.9	6.4	2.1

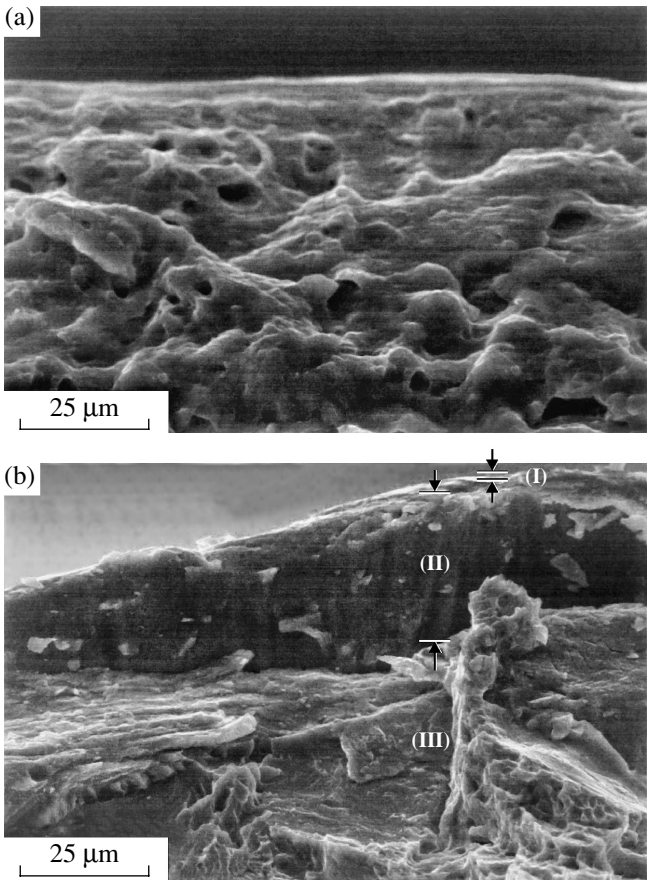

Fig. 3. Electron micrographs showing the structure of the brittle cleavage surface of VT1-0 titanium samples (a) before and (b) after nitriding for 4.5 h at 550°C in a glow discharge plasma: (I) titanium nitride rich film; (II) diffusion saturation layer; (III) heat-affected zone.

upon brittle cleavage of the material (Fig. 3). Judging from the observed relief, the surface layer of nitrided samples has a submicrocrystalline structure with a grain size of ~350–400 nm. The maximum hardness (which could be fully revealed only by nanoindentation tests) of this surface layer varied depending on the load (50 or 200 mN) within 10–18.5 GPa. The thickness of this hardened layer decreased from 1.5 to 0.1 μm when the temperature of processing was reduced from 750 to 450°C. An analysis of the phase composition of a nitrided layer was performed by means of electron microscopy in the diffraction regime. The carbon replicas revealed (in addition to TiN) the presence of titanium oxides (TiO and TiO_2) and (relatively rare) titanium hydrides. As a rule, the oxide and hydride phases occur in the form of films with thicknesses of up to several tens of nanometers, while the thickness of titanium nitride fragments reaches several hundreds of nanometers.

In order to determine the influence of argon on the dissociation of nitrogen molecules and to elucidate the roles of N^+ ions and neutral N atoms in the course of nitriding in glow discharge plasma, we have studied the dependence of the microhardness of titanium on the content of argon in the working gas mixture at a constant total pressure, discharge voltage, and sample temperature. An increase in the argon content from 0 to 40% led to a 15–20% growth in the microhardness. This effect is probably explained by an increase in the degree of molecular nitrogen dissociation in the mixture, which leads to an increasing number of N atoms and N^+ ions. This conclusion agrees with the results recently reported in [9], where it was also found that the number of N^+ ions increased with the argon content in the mixture.

In conclusion, the results of our investigation showed that the saturation of titanium with nitrogen in a hollow-cathode glow discharge is a plasmachemical process in which the decisive role belongs to atomic nitrogen formed as a result of the dissociation of molecular nitrogen. This dissociation is related to the excitation of molecules by electrons oscillating in the hollow cathode, followed by decay of the excited molecules. The exposure to plasma results in the formation of a multilayer gradient structure at the metal surface, which comprises a titanium nitride rich film, a diffusion saturation layer, and a heat-affected zone with a gradual transition to the bulk material. The surface layer exhibits a characteristic golden appearance and contains, in addition to titanium nitride, inclusions of titanium oxide and hydride phases.

Acknowledgments. This study was supported in part by the Russian Foundation for Basic Research, project no. 02-02-39002.

REFERENCES

1. K. T. Rei and T. Lampe, Mater. Sci. Eng. **69**, 437 (1985).
2. T. A. Panaioti, Fiz. Khim. Obrab. Mater., No. 4, 70 (2003).
3. A. M. Smyslov and E. V. Safin, in *Proceedings of the 5th Conference on Modification of Material with Particle Beams and Plasma Flows, Tomsk, 2000*, pp. 352–353.
4. V. V. Budilov and R. D. Agzamov, in *Proceedings of 6th Conference on Modification of Material with Particle Beams and Plasma Flows, Tomsk, 2002*, pp. 428–431.
5. V. M. Nerovnyĭ and V. V. Peremit'ko, Fiz. Khim. Obrab. Mater., No. 3, 49 (1995).
6. M. I. Guseva, G. M. Gordeeva, Yu. V. Martynenko, *et al.*, Fiz. Khim. Obrab. Mater., No. 2, 11 (1999).
7. E. I. Meletis, Surf. Coat. Technol. **149**, 95 (2002).
8. P. M. Schanin, N. N. Koval, Yu. A. Akhmadeev, and S. V. Grigor'ev, Zh. Tekh. Fiz. **74** (5), 24 (2004) [Tech. Phys. **49**, 545 (2004)].
9. Z. X. Cao and H. Oecher, J. Vac. Sci. Technol. A **22**, 321 (2004).

Translated by P. Pozdeev

Technical Physics Letters, Vol. 31, No. 7, 2005, pp. 551–554. Translated from Pis'ma v Zhurnal Tekhnicheskoĭ Fiziki, Vol. 31, No. 13, 2005, pp. 31–38.

Dynamic Features of the Photoinduced Plasticity Kinetics in Glassy Semiconductors

M. L. Trunov*, S. N. Dub, and R. S. Shmegera

Uzhgorod National University, Uzhgorod, Ukraine

Bakul' Institute for Superhard Materials, National Academy of Sciences of Ukraine, Kiev, Ukraine

** e-mail: stm@tn.uz.ua*

Revised manuscript received March 3, 2005

Abstract—The photoinduced variation of plasticity (photoplastic effect) in glassy semiconductor films was studied for the first time on a nanoscale level using a nanoindentation technique. It is shown that an increase in Young's modulus and a decrease in the nanohardness for such films in the initial stage of their exposure to light with a wavelength in the vicinity of the fundamental absorption edge is a characteristic feature of the photomechanical response kinetics. The photoplastic after-effect has been observed, whereby the state of film softening (as compared to the initial dark state) is retained for some time after the light switch-off, and the length of this period is dependent on the conditions of exposure. © *2005 Pleiades Publishing, Inc.*

Previously, the evolution of the plastic properties of glassy semiconductor films irradiated by light in the spectral region near the fundamental absorption edge was studied using a microindentation technique [1, 2]. It was found that chalcogenide glasses of the As–Se system exhibited a negative photoplastic effect (athermal photosoftening), which was reversible with respect to the light being switched on and off. This phenomenon can be used for high-density data recording based on the local deformation of a storage medium with simultaneous application of mechanical load to the material surface. This principle of data recording, which may be called photomechanical, offers potentially higher performance characteristics and is free of some disadvantages inherent in the conventional thermomechanical method, according to which the material is softened by thermal heating [3].

In order to develop the photomechanical recording technology, it is necessary to know the dynamic characteristic of the mechanical response of materials to the applied load and the exposure to light on a nanoscale level. The possibilities of microindentation techniques are rather restricted in this respect, since the material response cannot be determined on the required temporal (~0.1–1 s) and spatial (10–100 nm) scales. However, modern nanohardness meters allow the dynamics of indenter penetration in the course of precise local action on the surface of a material to be studied *in situ* (with continuous monitoring of the indentation depth) and the kinetics of elastic and viscoelastic recovery upon unloading to be traced.

This Letter presents data on the photoplasticity kinetics, the plastic flow at a preset load, and subsequent recovery upon rapid unloading in glassy semiconductor films studied by method of nanoindentation under conditions of fast loading with a sharp indenter.

The experiments were performed on thin films of a chalcogenide glass with the stoichiometric composition As_2Se_3 prepared by thermal deposition on K-8 glass substrates. The film thickness was monitored in the course of deposition and controlled so as to be about 2 μm. In order to reduce the influence of relaxation processes involved in the glass structure stabilization, the freshly deposited samples were kept in the dark for three months. The stabilized films were exposed to radiation of a solid state laser with a wavelength of 650 nm. The laser photon energy (E = 1.90 eV) is close to the bandgap width (E_g = 1.78 eV at an absorption coefficient of $\alpha = 10^3$ cm^{-1}) of the film material. The laser beam intensity on the sample surface did not exceed 20 mW/cm^2.

The mechanical properties of the deposited films were studied using the nanoindentation technique. The investigation was performed on a Nanoindenter II (MTS Systems) nanohardness meter using the Berkovich indenter (a trihedral diamond pyramid with a 65.3° apical angle and a tip curvature radius of about 200 nm). The main characteristics of this device and details of the nanohardness testing are presented in [4, 5]. The nanohardness H and Young's modulus E were calculated according to the Oliver–Pharr method [6] based on the indentation depth determined from the indenter penetration diagram measured in the course of each test. The tests were performed on five samples prepared in the same deposition cycle, which provided the statistics necessary for evaluation of the reproducibility of the experimental data. The experimental error did not exceed 0.01 GPa for the nanohardness and 0.5 GPa for Young's modulus.

1063-7850/05/3107-0551$26.00 © 2005 Pleiades Publishing, Inc.

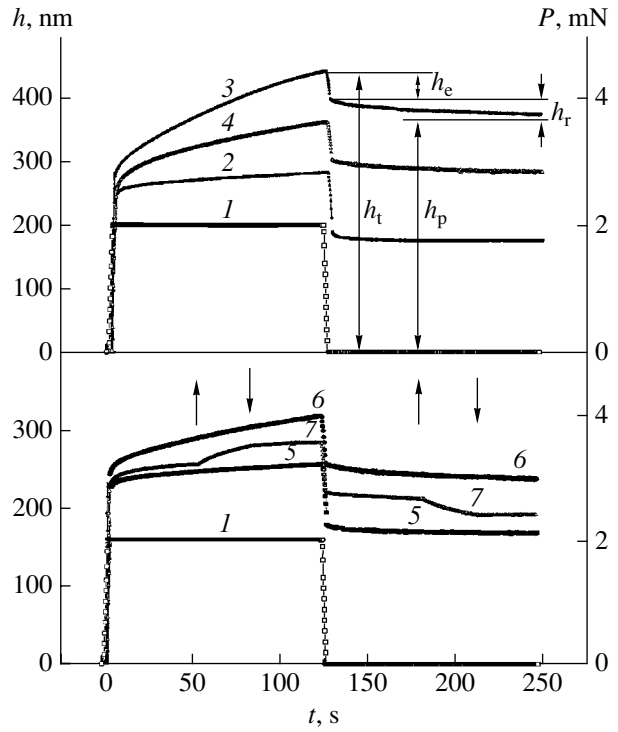

Fig. 1. Time variation of the indenter penetration depth h in 2-μm-thick As_2Se_3 films tested by nanoindentation (*2*, *5*) in the dark, (*3*, *4*, *6*) under irradiation, and (*7*) in the dark with short-time exposures immediately upon repeated irradiation. Curve *1* shows a diagram of the indenter load *P*. Arrows indicate the moments of light switching on (↑) and off (↓) for curve *7* (see the text for explanations).

The investigation was performed using the method of cyclic indentation [1], whereby several nanoindentations (load–unload test cycles) were made under the same indenter load and other test conditions. After each cycle, the indenter holder was moved relative to the sample, so that each subsequent test cycle was performed at a new site on the film. The distance between these indentation sites was 25 ± 0.5 μm, so that the total area of the test region was much smaller than the laser spot size on the sample surface. Each sample was used in a series of eight test cycles, two of which were performed in the dark (before and after the exposure to laser radiation), and the other six, in the course of the exposure; in addition, three test cycles were performed after keeping the samples in the dark for 24 h. The time interval between test cycles was 3–6 min (this time was required for the indenter positioner to find the new test site). Each test cycle consisted of four time steps: loading (2 s), holding at the maximum load (120 s), unloading to zero (2 s), and viscous recovery (120 s). The test schedule is presented by curve *1* in Fig. 1. The maximum load in each test was the same (2 mN).

In contrast to the traditional data presentation in the form of *P–h* diagrams (*P* is the indenter load and *h* is the penetration depth) adopted in the nanoindentation experiments [4], we used the *h–t* diagrams (*t* is the current test time), which is more illustrative under the conditions of our experimental procedure. The *h–t* diagrams were used for determining the unrecovered total print depth h_t and the particular deformation components in the course of the test, including elastic (h_e), plastic (h_p), and viscous relaxation (h_r) components (Fig. 1, curve *3*).

Figure 1 presents the typical experimental *h–t* curves obtained in the course of nanoindentation of an As_2Se_3 film in the dark (curve *2*), during the first exposure to laser radiation (curves *3* and *4*, corresponding to the first and third test cycles on exposure, respectively), after keeping the exposed film in the dark for 24 h (curve *5*), and after repeated irradiation (curve *6*). Curve *7* was measured immediately after termination of the second exposure and describes the mechanical response of the sample to the following sequence of events: (i) the indentation was started in the dark; (ii) the light was switched on at $t = 60$ s under the full load and then switched off upon a 30-s exposure; and (iii) an analogous switch on–off procedure was carried out upon unloading, during the viscoelastic print recovery in the dark (the moments of light switching on and off are indicated by arrows). The main parameters of the mechanical response of the film to these external actions, as well as their relative variations determined for the aforementioned tests, are summarized in the table, where $\Delta H = H - H_0$, $\Delta E = E - E_0$, $K = (H^3/E^2) \times 10^2$, and the test results are listed in accordance with the curves presented in Fig. 1.

As can be seen from the results of our experiments, the depth of indenter penetration during nanoindentation in the dark (both before and after irradiation) rather weakly varies when the indenter is kept under an applied load, while the subsequent print recovery is determined primarily by the elastic component h_e at the moment of step unloading (Fig. 1, curves *2* and *5*).

The pattern obtained for the sample under irradiation is quite different and resembles the behavior observed in our previous microindentation experiments [1, 2]. In the first test cycle on exposure, the indenter penetration depth in the course of loading exhibits a sharp growth (Fig. 1, curve *3*), whereas, in the third cycle, the rate of this growth decreases (curve *4*). The results of statistical processing of the experimental results allow us to ascertain that the difference between curves *3* and *4* falls outside the natural scatter (related to a local inhomogeneity of the film surface) and reflects a real evolution of the plastic properties of films on exposure to light.

The obtained *h–t* diagrams reveal a significant redistribution of the elastic (h_e) and viscous relaxation (h_r) components of the print recovery upon unloading. As can be seen in Fig. 1, the viscous recovery component h_r observed under irradiation is noticeably greater in absolute value than the dark recovery. This is unambiguous evidence for a significant increase ("defreezing")

of the kinetic mobility of molecular units in the glass structure on exposure to light, as well as for the light-induced general glass structure relaxation.

Evaluation of the resistance of the film material to the plastic deformation, expressed in terms of the $K = H^3/E^2$ parameter [7], shows that the film plasticity in the initial stage of exposure is about 20 times that in the dark. It should be noted that Young's modulus of the film in the initial stage of irradiation increases, whereas the nanohardness drops more than by half (see table), although these characteristics usually exhibit a direct correlation. Discussion of this fact falls outside the scope of this paper; we must only point out that this behavior was observed in all the samples tested, as well as in the samples of glassy semiconductors of other compositions.

We have also observed the photoplastic after-effect, whereby the films occur in a metastable softened state for some time immediately upon termination of irradiation (Fig. 1, curve *7*). This state differs from the initial dark state (Fig. 1, curve *5*).[1] The afteraction time depends on the irradiation conditions (light intensity, duration of exposure) and may vary from a few seconds to several tens of seconds.

An analysis of the obtained results shows that all components of the photomechanical response exhibit nonmonotonic changes in the course of irradiation. This behavior is illustrated in Fig. 2, which shows the evolution of components of the total deformation h_t, including the elastic (h_e), plastic (h_p), and viscous relaxation (h_r) components, in comparison to Young's modulus (E) and the nanohardness (H) in the course of eight test cycles performed before, during, and after the first laser irradiation. The deformation components were determined from the indenter recovery diagram measured in the course of each test cycle (as indicated for curve *3* in Fig. 1). This method of data treatment is similar to that used for material testing in the regime of strain relaxation [8].

As can be seen from Fig. 2, the relative contributions of various components to the total deformation, as well as their dynamics, are different. Switching on the light (indicated by the arrow pointing up) leads to a significant increase in the plastic deformation component (curve *1*), a decrease in the elastic component (curve *2*), and the appearance of an appreciable relaxation component (curve *3*). Young's modulus E (curve *5*) and the nanohardness H (curve *4*) also exhibit nonmonotonic dynamics. This pattern indicates that the film structure is continuously changing both during irradiation and upon switching off the light; the maximum changes take place during the initial period of exposure (~300 s under the irradiation conditions indicated above).

[1] At the same time, keeping irradiated samples in the dark for 24 h results in their significant strengthening, which is manifested by an increase in both the nanohardness and Young's modulus (see table).

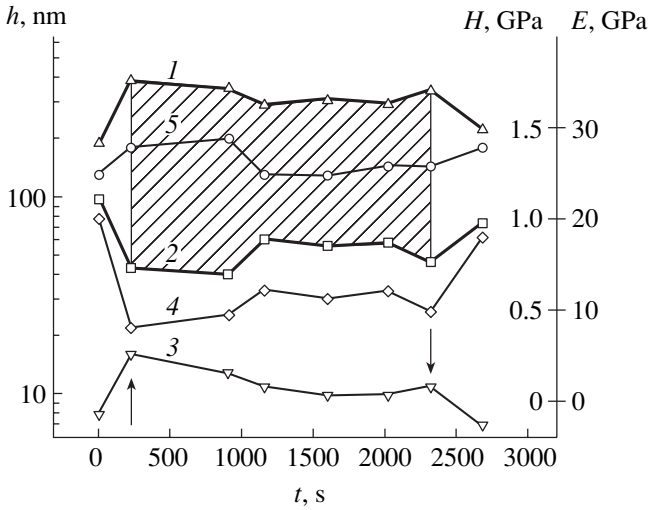

Fig. 2. Dynamics of the photomechanical response of a 2-μm-thick As_2Se_3 film tested by nanoindentation in the course of laser irradiation: (*1–3*) plastic (h_p), elastic (h_e), and viscous relaxation (h_r) components of the total deformation, respectively; (*4*) nanohardness H; (*5*) Young's modulus E. Cross-hatched region shows the variation of the contribution of plastic and elastic components in the film loaded under irradiation. Arrows indicated the moments of light switching on (↑) and off (↓).

To summarize, we have used a nanoindentation technique to study for the first time the dynamic features in the behavior of all elastic and plastic compo-

Parameters of the mechanical response of a 2-μm-thick As_2Se_3 film tested by nanoindentation in the course of laser irradiation and keeping in the dark

Test (see Fig. 1)	H, GPa	E, GPa	K, GPa	$\Delta H/H_0$, %	$\Delta E/E_0$, %
Freshly deposited films tested after 3-month stabilization in the dark					
Dark test (curve *2*)	1.00 (H_0)	25.0 (E_0)	0.160	0	0
Irradiation, 1st test cycle (curve *3*)	0.40	28.0	0.008	–60	+12
Irradiation, 3rd test cycle (curve *4*)	0.50	25.0	0.020	–50	0
Irradiated films tested after 24-h keeping in the dark					
Dark test 24 h after irradiation (curve *5*)	1.44 (H_0)	31.5 (E_0)	0.30	0	0
Repeated irradiation (curve *6*)	0.92	33.0	0.07	–36	+4
Dark test with short-time exposures, performed immediately upon repeated irradiation (curve *7*)	1.02	29.0	0.12	–29	–8

nents in the mechanical response of glassy semiconductor films exposed to laser radiation. The obtained experimental results provide quantitative data on the time evolution of these components and their relative magnitudes.

REFERENCES

1. M. L. Trunov, Pis'ma Zh. Tekh. Fiz. **30** (20), 49 (2004) [Tech. Phys. Lett. **30**, 865 (2004)].
2. M. L. Trunov and V. S. Bilanich, Thin Solid Films **459**, 228 (2004).
3. P. Vettiger, M. Despont, U. Drechsler, *et al.*, IBM J. Res. Dev. **44**, 323 (2000).
4. N. G. Olson, C. Leung, and X. Wang, Exp. Tech. **12**, 51 (2002).
5. S. N. Dub, in *Proceedings of the 9th International Symposium on Thin Films in Electronics, Kharkov, 2003* ("Konstanta" R&D Center, Kharkov Physicotechnical Institute, Kharkov, 2003), pp. 343–349.
6. W. C. Oliver and G. M. Pharr, J. Mater. Res. **7**, 1564 (1992).
7. A. Leyland and A. Matthews, Wear **246**, 1 (2000).
8. *Relaxation Phenomena in Solids*, Ed. by V. S. Postnikov (Metallurgiya, Moscow, 1968) [in Russian].

Translated by P. Pozdeev

Technical Physics Letters, Vol. 31, No. 7, 2005, pp. 555–557. Translated from Pis'ma v Zhurnal Tekhnicheskoĭ Fiziki, Vol. 31, No. 13, 2005, pp. 39–45.

Nonlinear Electric Response Enhancement in Metal Films with Regular Inhomogeneities

S. V. Khor'kov

Nizhni Novgorod State Technical University, Nizhni Novgorod, Russia

e-mail: priem@nntu.nnov.ru

Revised manuscript received February 21, 2005

Abstract—The nonlinear response of thin metal films textured by periodic inclusions has been studied. The effective nonlinear conductivity exhibits critical behavior, which is determined by the relative "density" of insulating or perfectly conducting inclusions. © *2005 Pleiades Publishing, Inc.*

The nonlinear electric response of inhomogeneous systems has been extensively studied by experimental methods, in particular, using higher harmonics in the response voltage of samples in a variable electric field [1–3] and nonlinear voltage–current (*I–U*) characteristics [4, 5]. It was established that nonlinear characteristics such as the third harmonic amplitude, the effective nonlinear conductivity of a medium, and the relative intensity of the 1/*f* noise [2] are determined by the fourth-power electric field correlator $\langle \mathbf{e}^4 \rangle$ [6–8] (where angle brackets $\langle \ldots \rangle$ denote averaging of the volume of the medium).

If the structure of a medium is randomly disordered, the electric field exhibits fluctuations that lead to enhancement of the nonlinear properties. However, the effective electric conductivity also exhibits enhancement in periodic structures, where the nonlinear response increases because the current lines concentrate in narrow links connecting regions occupied by a highly conducting component [10]. This results in a significant heating of the electron gas in the vicinity of geometric features of the periodic structure.

In this study, the nonlinearity of a medium is taken into account by adding a cubic term to the current density expansion in powers of the field strength in the Ohm law:

$$\mathbf{j} = \sigma\mathbf{e} + \chi\mathbf{e}^2\mathbf{e},$$

where σ and χ are the linear and nonlinear conductivities, respectively. Let us restrict our consideration to the case of weak nonlinearity, so that $\sigma \gg \chi\mathbf{e}^2$, and assume that the system dimensions are such that the effective conductivity components σ_{eff} and χ_{eff} exhibit self-averaging. Then, the Ohm law for the whole medium can be written as

$$\mathbf{J} = \sigma_{\text{eff}}\mathbf{E} + \chi_{\text{eff}}\mathbf{E}^2\mathbf{E}, \quad (1)$$

where $\mathbf{J} = \langle \mathbf{j} \rangle$ and $\mathbf{E} = \langle \mathbf{e} \rangle$ are the average current density and field strength, respectively, in the sample. Stroud and Hui [7] showed that, if $\sigma_{\text{eff}} > \chi_{\text{eff}}\mathbf{E}^2$, the effective nonlinear conductivity χ_{eff} of a heterogeneous medium can be determined as

$$\chi_{\text{eff}} = \frac{\langle \chi\mathbf{e}^4 \rangle}{\langle \mathbf{e} \rangle^4}, \quad (2)$$

where $\mathbf{e}$ is the electric field in the equivalent linear medium.

This paper is devoted to a description of the effective nonlinear conductivity of a film containing cross-shaped inclusions. The inclusions are assumed to be negligibly thin and to have a linear size of 2*h*, while their centers are spaced by 2*a* and form a square lattice. Figure 1 shows a unit cell *ABCD* of this lattice. The film thickness is assumed to be sufficiently small so that the current distribution can be considered two-dimensional; by virtue of the symmetry, this distribution is periodic. We will consider two limiting cases, whereby the cross-shaped inclusions are insulating or perfectly conducting. The first case corresponds, for example, to a metal film with a high conductivity σ, in which thin cuts are made by a laser so as to form cross-shaped "inclusions" not conducting electric current. A film made of a low-purity metal with a low conductivity σ, which contains high-purity metal inclusions whose conductivity is several orders of magnitude higher than σ, corresponds to the second limiting case.

Within the framework of the electron temperature approximation, the nonlinear conductivity of a film can be determined as $\chi = \dfrac{\partial\sigma(T)}{\partial T}\dfrac{\sigma}{\Lambda}$, where Λ is the coefficient of heat transfer from electrons to the lattice [11]. In order to determine the effective nonlinear conductivity χ_{eff} according to relation (2), it is necessary first to calculate the electric field in the equivalent linear medium. Owing to the periodicity of the model structure, it will be sufficient to determine the field within a single unit cell *ABCD*. In the linear case, the electric

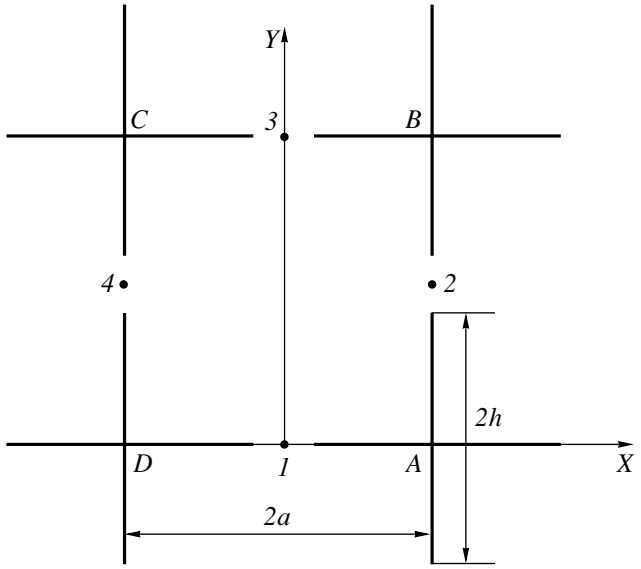

Fig. 1. Schematic diagram showing the unit cell *ABCD* of an inhomogeneous medium with a periodic structure: 2*a* is the distance between the centers of cross-shaped inclusions and 2*h* is the linear size of inclusions (see the text for explanations).

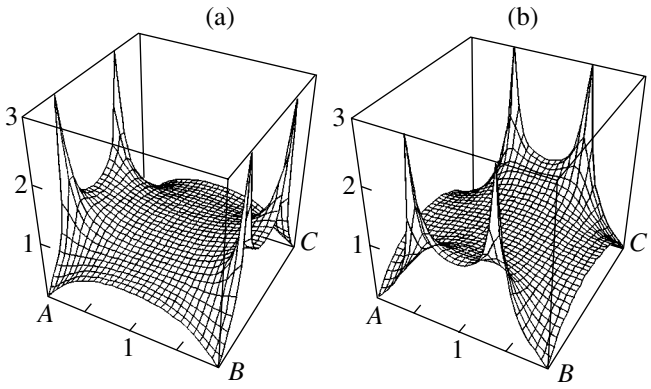

Fig. 2. Electric field distribution in a unit cell *ABCD* for $|\mathbf{E}| = 1$, $a = 1$, and $h = 0.5$ in a medium with (a) dielectric and (b) perfectly conducting inclusions.

field can be determined by means of conformal mapping. The external field **E** will be considered as known. If this field is oriented along the *X* axis (Fig. 1), the complex field in a system with dielectric inclusions can be written as (see [12])

$$e(z) = \frac{A}{C}\left(\frac{1-\mathrm{sn}^2(z)}{\xi_0^2-\mathrm{sn}^2(z)}\right)^{1/2}, \qquad (3)$$

where $z = x + iy$, sn(*z*) is the amplitude (elliptic) sine,

$$z = C\int_0^{\mathrm{sn}(z)} \frac{dt}{\sqrt{(1-t^2)(1-k^2t^2)}}; \quad k = 1/\sqrt{2},$$
$$C = a/K(k),$$

K is the complete elliptic integral of the first kind, and ξ_0 is a constant that can be expressed in terms of the amplitude delta function $dn(\ldots)$ as $\xi_0 = 1/dn(h/C, k)$. The coefficient *A* can be determined via conformal mapping of the unit cell *ABCD* (featuring a complex field distribution) onto a parallelogram in which the field is homogeneous. Since the square of the field is invariant relative to such transformations, we obtain

$$A = a\frac{|\mathbf{E}|}{K(k\xi_0)}. \qquad (4)$$

Figure 2a shows a distribution of the complex field (3) in the unit cell for $|\mathbf{E}| = 1$ and $h = a/2$.

Then, in order to determine the effective nonlinear conductivity χ_{eff} according to relation (2), it is necessary to integrate $|e(z)|^4$ over the unit cell volume. Let us analyze the electric field distribution so as to find the regions providing the main contributions to the nonlinear response. Note that the field exhibits singularities at the end points of the vertical elements of inclusions (Fig. 2), which may account for the main contribution to the $\langle|e|^4\rangle$ correlator. One can readily check that the field at these points exhibits asymptotic behavior of the type $|e(r)| \propto 1/r^{1/2}$. Integrating $|e(z)|^4$ over the unit cell area, we obtain a logarithmic divergence in *r* at the lower limit. However, it would be incorrect to conclude that the nonlinear response is large due to these sharpenings. Actually, this divergence of χ_{eff} is related to the assumption of infinitely thin inclusions. In real inclusions, the ends of the crosses have finite curvature radii, and the divergence disappears.

Now it will be shown that the effective nonlinear conductivity strongly increases when the density of current lines at the source and sink is large. Let us introduce a parameter characterizing the inhomogeneity of the medium: $\tau = (a - h)/a$. In the case when the inclusions almost touch one another ($\tau \ll 1$), the electric field asymptotically tends to

$$|e(r)| \propto \frac{|\mathbf{E}|a}{K(k\xi_0)r} \qquad (5)$$

in a region with the dimensions $d \ll r \ll a$, where *r* is measured from points *2* and *4* (Fig. 2), and $d = 2(a–h)$ is the gap width for the current flowing in and out of the cell.

Determining the effective nonlinear conductivity according to formula (2), using the asymptotic relation (5), and integrating over the unit cell in a polar coordinate system, we eventually obtain

$$\chi_{\mathrm{eff}} \approx \chi\frac{a^2}{2K^4(k\xi_0)}\int_0^{\pi}\int_d^a \frac{r\,dr\,d\alpha}{r^4} \approx \chi\frac{\pi}{4\tau^2\ln^4(\gamma/\tau)}. \qquad (6)$$

Formula (6) was obtained taking into account that, for $\tau = d/2a \ll 1$, we have $K(k\xi_0) \approx \ln\gamma/\tau$, where $\gamma =$

$4/K^4(1/\sqrt{2})$. Therefore, the effective nonlinear conductivity exhibits anomalous behavior for $\tau \longrightarrow 0$.

Now let us consider the case when the cross-shaped inclusions are perfectly conducting. Again, for determining the effective nonlinear conductivity χ_{eff} according to relation (2), it is necessary first to calculate the electric field in the equivalent linear medium. Following the scheme proposed in [12], we arrive at an expression analogous to (3), in which ξ_0 has to be replaced by $\eta_0 = dn((a-h)/C, k)$:

$$e(z) = \frac{D}{C}\left(\frac{1-\mathrm{sn}^2(z)}{\eta_0^2-\mathrm{sn}^2(z)}\right)^{1/2}, \quad (7)$$

where

$$D = a\frac{|\mathbf{E}|}{K(k\eta_0)}. \quad (8)$$

Figure 2b shows the corresponding distribution of the complex field in the unit cell for $|\mathbf{E}| = 1$ and $h = a/2$. In this case, the field exhibits singularities at the end points of the horizontal elements of inclusions, where the asymptotic behavior also corresponds to $|e(r)| \propto 1/r^{1/2}$. As was noted above, this behavior is related to zero curvature of the cross ends, which is physically unrealistic. According to physical considerations, the effective nonlinear conductivity strongly increases with decreasing parameter τ. Using relations (7) and (8), one can readily show that, in the case when the inclusions almost touch one another, the electric field at points *1* and *3* asymptotically tends to

$$|e(r)| \propto \frac{|\mathbf{E}|a}{K(k\eta_0)r}. \quad (9)$$

This asymptotic behavior becomes quite evident if we recall the problem of determining the electric field in a capacitor with convex plates. In our case, the role of plates is played by the horizontal elements of the cross-shaped inclusions. The field in such a capacitor behaves as $|e(r)| \propto 1/r$.

Using the asymptotic relation (9) and performing calculations analogous to those used in deriving formula (6), we eventually obtain an expression for the effective nonlinear conductivity for $\tau \longrightarrow 0$ in the case of perfectly conducting inclusions:

$$\chi_{eff} = \chi\frac{4}{\pi^3\tau^2}. \quad (10)$$

In continuous metal films, the effective nonlinear conductivity χ is, in a certain sense, small. However, as was demonstrated above, the presence of dielectric or perfectly conducting cross-shaped inclusions in such films may lead to considerable growth of the effective nonlinear conductivity χ_{eff}, which may significantly exceed χ. A control parameter in this system is τ, which characterizes the relative "density" of inclusions. It should be noted that, despite the growth of χ_{eff} with decreasing τ, the second term in the right-hand part of Eq. (1) has to be greater than the first term. This condition can always be met by decreasing the average field **E** in the medium.

As was noted above, the third harmonic amplitude and the relative density of the $1/f$ noise in inhomogeneous media are also proportional to the $\langle \mathbf{e}^4 \rangle$ field correlator. This implies that these quantities must also behave like the nonlinear conductivities given by formulas (6) and (10). Experiments [1–4] showing evidence for the enhancement of a nonlinear response in the critical region were performed for randomly inhomogeneous metal films. To the author's knowledge, no experimental data were reported for the films with regular structures of inhomogeneities considered in this study and in previous papers [10, 13].

Acknowledgments. The author is grateful to A.M. Satanin for fruitful discussions.

REFERENCES

1. M. A. Dubson, Y. C. Hui, M. B. Weissman, *et al.*, Phys. Rev. B **39**, 6807 (1989).
2. Y. Yagil, G. Deutcher, and D. J. Bergman, Phys. Rev. Lett. **69**, 1423 (1992).
3. Y. Yagil and G. Deutcher, Phys. Rev. B **46**, 16115 (1992).
4. Y. Gefen, W. H. Shih, R. B. Laibowitz, *et al.*, Phys. Rev. Lett. **57**, 3097 (1986).
5. R. K. Chakrabarty, K. K. Bardhan, and A. Basu, Phys. Rev. B **44**, 6773 (1991).
6. A. Aharony, Phys. Rev. Lett. **58**, 2726 (1987).
7. D. Stroud and P. M. Hui, Phys. Rev. B **37**, 8719 (1988).
8. D. J. Bergman, Phys. Rev. B **39**, 4598 (1989).
9. A. M. Satanin, S. V. Khor'kov, and A. Yu. Ugol'nikov, Pis'ma Zh. Éksp. Teor. Fiz. **62**, 301 (1995) [JETP Lett. **62**, 322 (1995)].
10. A. M. Satanin, V. V. Skuzovatkin, and S. V. Khor'kov, Zh. Éksp. Teor. Fiz. **112**, 643 (1997) [JETP **85**, 351 (1997)].
11. F. G. Bass and Yu. G. Gurevich, *Hot Electrons and Strong Electromagnetic Waves in a Plasma of Semiconductors and Gas Discharge* (Nauka, Moscow, 1975) [in Russian].
12. B. Ya. Balagurov, Zh. Tekh. Fiz. **51**, 1146 (1981) [Sov. Phys. Tech. Phys. **26**, 651 (1981)].
13. A. M. Satanin, S. V. Khor'kov, and V. V. Skuzovatkin, Pis'ma Zh. Éksp. Teor. Fiz. **65**, 521 (1997) [JETP Lett. **65**, 544 (1997)].

Translated by P. Pozdeev

Technical Physics Letters, Vol. 31, No. 7, 2005, pp. 558–559. Translated from Pis'ma v Zhurnal Tekhnicheskoĭ Fiziki, Vol. 31, No. 13, 2005, pp. 46–49.

Photosensitive Silicon Bipolar Negative-Differential-Resistance Device with Controlled *I–U* Characteristic

I. A. Kashtankin and N. T. Gurin*

Ul'yanovsk State University, Ul'yanovsk, Russia

** e-mail: gurinnt@sv.ulsu.ru*

Received February 28, 2005

Abstract—A photosensitive negative-differential-resistance (NDR) device has been developed based on two low-power bipolar silicon transistors on a common substrate, with the emitter junction of one transistor shunted by the conducting channel of the other transistor. As the intensity of IR radiation incident on the shunting transistor increases, the peak current in the N-shaped *I–U* characteristic decreases until it vanishes completely. An increase in the intensity of IR radiation incident on the shunted transistor leads to a significant increase in the peak current. © *2005 Pleiades Publishing, Inc.*

Semiconductor structures with N-shaped *I–U* curves possess a number of unique properties, which stimulate the search for new solutions in technology and circuit design aimed at the development of novel semiconductor devices. In recent years, much attention has been devoted to the implementation of such negative-differential-resistance (NDR) devices in telecommunication and low-current automation systems, which makes it possible to use simpler circuits, reduce weight and size characteristics, and increase the performance and reliability of equipment [1, 2]. There is extensive literature devoted to the problems encountered in the development, construction, and investigation of NDR devices. At the same time, the effects of various external factors, including radiation and temperature, on the formation of NDR are still insufficiently studied.

The most effective means of obtaining semiconductor devices with NDR regions in the *I–U* curves are (i) modulation of the base current and (ii) shunting of the emitter junction in a bipolar transistor with the aid of a controlled resistance. In particular, the role of this controlled element can be played by a MIS or a bipolar transistor [3]. Previously, we have demonstrated the possibility of creating a photosensitive NDR device, in which the emitter junction of a bipolar transistor is shunted by the conducting channel of a MIS transistor [4].

In this Letter, we report on the effect of IR radiation with a wavelength of 950 nm and a power of 10–120 mW on the characteristics of a bipolar *N*-type transistor based on a planar silicon structure grown on a ⟨100⟩-oriented phosphorus-doped single crystal (KEF-4.5 grade) substrate (r_v = 4.6 Ω cm), with a 6-μm-thick boron-doped *P*-base (R_s = 2.6 Ω/□) and a 1.2-μm-thick phosphorus-doped N^+-emitter (R_s = 40 Ω/□). The metallization layer thickness was 1 μm. A schematic diagram of the device and its equivalent scheme are presented in Fig. 1.

A positive feedback chain in the given NDR device is formed by transistor T_2, whose collector–emitter circuit controls the base–emitter current in the transistor T_1. At low values of the collector voltage in T_1, the emitter junction of T_2 is closed and the base leakage current of T_1 is at a minimum. Resistor *R* prevents transistor T_2 from passage to a saturation regime. As the collector–emitter voltage U_c increases, the emitter junction of T_2 opens and this transistor passes from the cutoff regime to an active state, thus decreasing the base current of T_1 and the collector current I_c. This behavior determines the formation of the N-shaped characteristic (Fig. 2).

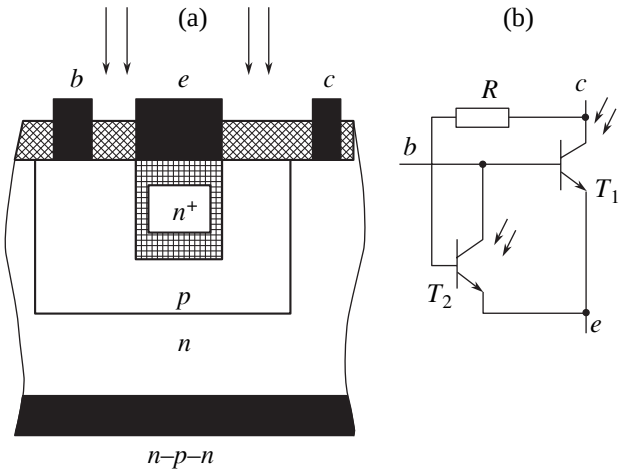

Fig. 1. Schematic diagrams of (a) the proposed NDR device structure and (b) its equivalent circuit (see the text for explanations).

1063-7850/05/3107-0558$26.00 © 2005 Pleiades Publishing, Inc.

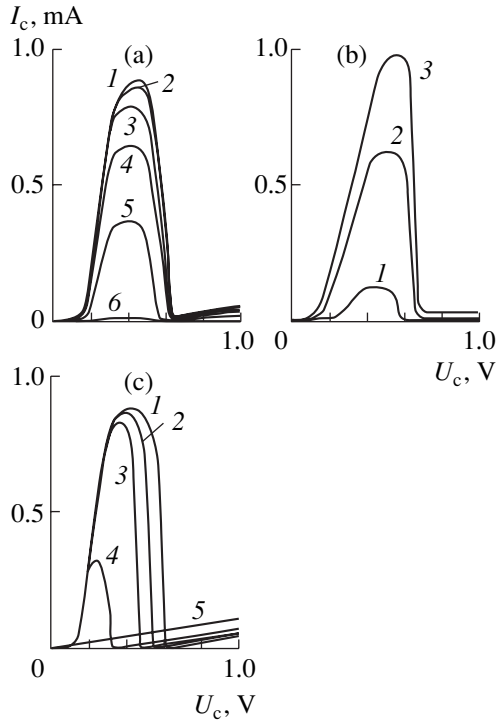

Fig. 2. The *I–U* curves of the proposed bipolar NDR-phototransistor exposed to IR radiation of various intensities *P* (U_0 = 0.5 V): (a) T_2 exposed, *P* = 0 (*1*), 10 (*2*), 20 (*3*), 40 (*4*); 80 (*5*), 120 mW (*6*); (b) T_2 exposed, *P* = 0 (*1*), 40 (*2*), 80 mW (*3*); (c) both T_1 and T_2 exposed, *P* = 0 (*1*), 20 (*2*), 40 (*3*). 80 (*4*); 120 mW (*5*).

When the base region of T_2 is exposed to IR radiation with increasing intensity, the maximum current in the *I–U* characteristic of the structure under consideration decreases as a result of the increasing shunting action. At a radiation power of 120 mW, the peak completely vanishes and the *I–U* curve is rectified (Fig. 2a). Irradiation of the base region of T_1 leads to a significant increase in the peak current in the same way as in usual bipolar phototransistors (Fig. 2b). When both transistors are exposed, the effect of shunting of the base of T_1 prevails and the peak current decreases until the NDR region completely vanishes (Fig. 2c). Note that the peak voltage also decreases.

Thus, using the proposed NDR device, it is possible either to decrease the peak current (up to complete rectification of the characteristic, with a decrease in the peak voltage) or to increase this peak, depending on the device geometry and the irradiation intensity. This behavior distinguishes the proposed device from other photosensitive NDR devices such as thyristors and triacs, in which IR radiation only decreases the S-shaped region in the *I–U* curve (up to its complete rectification).

Advantages of the proposed NDR device are its simple design, small number of component elements, the possibility of functional integration, low power, and small dimensions. These features open wide possibilities for implementing this device in various circuits for electronic equipment and photosensitive position sensors, generators, optoelectronic analog-to-digital converters, memory elements, and various automation systems.

Acknowledgments. This study was supported by the Presidential Program of Support for the Leading Scientific Schools in Russia (project no. NSh-1482-2003.8).

REFERENCES

1. S. A. Goryainov and I. D. Abezgauz, *Semiconductor Devices with Negative Resistance* (Énergiya, Moscow, 1970) [in Russian].
2. F. D. Kasimov, Mikrosist. Tekhn., No. 4, 6 (2003).
3. T. A. Vorob'eva and N. T. Gurin, Izv. Vyssh. Uchebn. Zaved., Élektronika, No. 5, 22 (2002).
4. I. A. Kashtankin and N. T. Gurin, in *Proceedings of the 6th International Conference on Opto-, Nanoelectronics, Nanotechnologies, and Microsystems, Ul'yanovsk, 2004*, p. 106.

Translated by P. Pozdeev

Technical Physics Letters, Vol. 31, No. 7, 2005, pp. 560–563. Translated from Pis'ma v Zhurnal Tekhnicheskoĭ Fiziki, Vol. 31, No. 13, 2005, pp. 50–57.

Effect of the Nanographite Film Thickness on the Optical Rectification Pulse

G. M. Mikheev[a,*], R. G. Zonov[a], A. N. Obraztsov[b], A. P. Volkov[b], and Yu. P. Svirko[c]

[a] *Institute of Applied Mechanics, Ural Division, Russian Academy of Sciences, Izhevsk, Udmurtia, 426067 Russia*

[b] *Department of Physics, Moscow State University, Moscow, 119992 Russia*

[c] *Department of Physics, Joensuu University, Joensuu, Finland*

** e-mail: gmmikheev@udmnet.ru*

Received February 21, 2005

Abstract—The phenomenon of optical rectification during pulsed laser irradiation was studied in nanographite films of various thicknesses obtained by plasmachemical deposition on silicon substrates. The amplitude of the optical rectification pulse (ORP) strongly depends on the film thickness h and reaches a maximum at $h \sim 2.5$ μm. At a smaller film thickness, the ORP is accompanied by a photoelectric signal of microsecond duration, which arises in the silicon substrate. For the nanographite films with $h > 2.5$ μm, the ORP is observed in the absence of any signal from the substrate, which allows such films to be used in fast-response detectors of pulsed laser radiation in a broad spectral range. © *2005 Pleiades Publishing, Inc.*

In recent years, there has been an explosion of interest in studying the optical and, especially, nonlinear optical properties of various nanostructured carbon materials. The obtained results point to the possibility of using fullerenes and carbon nanotubes in various devices, such as laser radiation limiters, optical switches, and passive gates [1–5]. Previously, we have reported [6–8] on the phenomenon of optical rectification in nanographite films, which are also characterized by low cold electron emission thresholds [9, 10]. When such a film is fixed between two parallel electrodes and exposed to nanosecond laser radiation pulses, a pulsed electric voltage appears between the electrodes, with the pulse shape repeating the laser pulse envelope. The discovery of this phenomenon opens new application fields for nanographite films, such as broadband laser radiation detectors, ultrashort electric pulse generators, and position-sensitive transducers [6–8]. In order to elucidate the mechanisms responsible for the generation of ultrashort photoelectric pulses in nanographite films, it is of interest to study a correlation between the observed photoelectric effects and the film thickness. This Letter presents the result of such investigations.

The experiments were performed with carbon films obtained by means of plasmachemical deposition from a methane–hydrogen mixture according to our standard method described elsewhere [10, 11]. The deposit thickness was controlled by varying the growth duration t within 0–180 min. The films were deposited onto $0.5 \times 25 \times 25$-mm silicon plates. As was demonstrated previously, the main structural elements in the carbon films obtained for $t = 60$ min are platelike crystallites of an irregular shape, comprising several (typically, five to fifty) parallel, well-ordered graphene layers [9, 10]. According to the data of Raman scattering, electron and X-ray diffraction, and high-resolution electron microscopy, the crystallite structure corresponds to that of a well-ordered graphite [12]. The thickness of these crystallites ranges from 2 to 20 nm, while their lateral dimensions vary within 1–3 μm. In all crystallites, the atomic layers exhibit predominant orientation in the direction of the normal to the substrate surface, with a maximum deviation from this direction not exceeding ±20°. The distance between crystallites is about 0.5–1 μm. Thus, the carbon films studied exhibit a clearly pronounced porous nanocrystalline structure. The average thickness of nanocarbon films was determined by the deposition time t and, for example, amounted to 2–3 μm for $t = 60$ min.

Figure 1 (inset) shows a schematic diagram of the experimental arrangement. A nanocarbon film *1* on a silicon substrate was pressed with two 3-mm-wide flat conducting clamps *2* (also playing the role of electrodes) to a dielectric sample holder. The distance between electrodes was approximately 18 mm. The rear surface of the sample substrate *3* was in contact with the sample holder (not depicted in the figure), while virtually the entire film surface was free, since the electrodes (parallel to each other) covered only a small part of this surface. A photoelectric signal, generated between electrodes when the film surface was irradiated, was fed directly to the input of a storage oscillograph *4* with a 50-MHz bandwidth and a 1-MΩ input

1063-7850/05/3107-0560$26.00 © 2005 Pleiades Publishing, Inc.

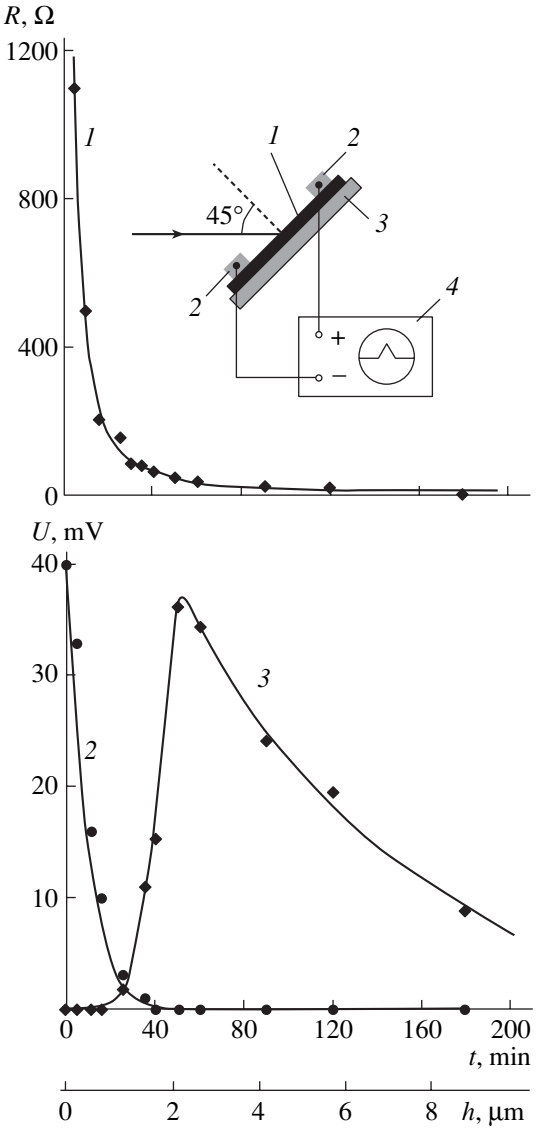

Fig. 1. Plots of the (*1*) interelectrode resistance *R*, (*2*) amplitude *U* of the photoelectric signal, and (*3*) ORP amplitude versus growth time *t* (or thickness *h*) of nanographite films. The inset shows a schematic diagram of the experimental arrangement (see the text for explanations).

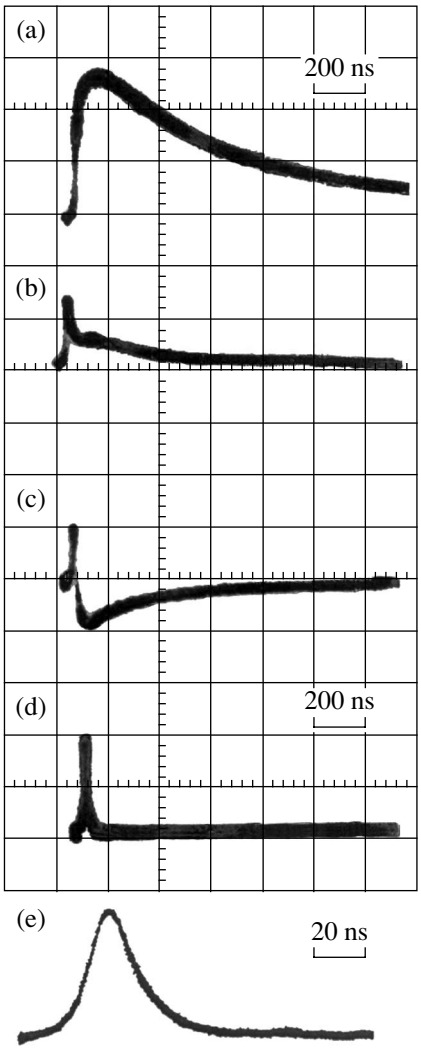

Fig. 2. The typical pulse waveforms measured for nanographite films with thicknesses (a) $h < 1$ μm, (b, c) $h = 1$–2.5 μm, and (d, e) $h > 2.5$ μm. The measurements were performed (a, b) near the lower electrode, (c) near the upper electrode, or (d, e) in an arbitrary site using storage oscillographs with (a–d) a 50-MHz bandwidth and 1-MΩ input impedance and (e) a 250-MHz bandwidth and 50-Ω impedance.

impedance or with a 250-MHz bandwidth and a 50-Ω impedance.

The measurements were performed under conditions corresponding to the maximum optical rectification pulse (ORP) amplitude, which was provided by a 45° angle of the laser beam incidence onto the film surface and the electrodes oriented perpendicular to the plane of light incidence [6, 7]. The films were exposed to *p*-polarized radiation of a single-mode single-frequency passive *Q*-switched YAG:Nd^{3+} laser [13] generating pulses of Gaussian shape with a full width at half maximum (FWHM) of $\tau \sim 20$ ns and pulse energy of $\varepsilon = 4$ mJ. The laser beam diameter was 2 mm.

The results of measurements were used to determine the dc resistance *R* between electrodes (Fig. 1, curve *1*) and the photoelectric pulse amplitude *U* (Fig. 1, curves *2* and *3*) as functions of the film thickness *h* (or the deposition time *t*). We have also thoroughly studied the shape of the photoelectric signals observed for the films grown for various times *t* (Fig. 2). After the photoelectric measurements, the samples were cleaved and the film thicknesses were measured with the aid of an optical microscope (×1000) equipped with a digital camera [14]. In this way, it was possible to determine the thickness of films obtained using relatively long deposition times. The thickness of thin films deposited for a short time was calculated using a formula derived

assuming that a silicon substrate and the nanographite film can be considered as two resistors connected in parallel: $h = (R_0 - R)/(RR_0a)$, where $a = L/(\rho L_0)$, R_0 is the resistance between electrodes on the silicon substrate in the absence of a graphite film, L is the electrode length, L_0 is the interelectrode distance, and ρ is the specific conductivity of the film material. The parameter a was calculated using the same formula with h independently determined for a thick film ($h > 3$ μm) with the aid of the optical microscope. Using the obtained dependence of the film thickness h on the deposition time t, it was possible to plot the results of measurements of the R and U values as functions of h (Fig. 1). It should be noted that initial stages of the deposition process were significantly different from the subsequent stages. In particular, deposition virtually does not take place during the first 5 min, which results in a nonlinear dependence of h on t in the interval from 0 to 20 min (Fig. 1, additional h axis).

The results of our experiments showed that laser irradiation of a film-free silicon substrate, as well as the substrates with films grown for $t = 0$–20 min, is accompanied by the appearance of a pulsed photoelectric signal between the electrodes with a FWHM of about 0.5 μs (Fig. 2a). The amplitude of this signal depends on the laser spot position on the sample surface relative to the electrodes. As the laser beam is scanned from the lower to upper electrode (see the inset in Fig. 1), the photoelectric signal amplitude first decreases to zero, changes in polarity, and then increases (in magnitude) again. It should be noted that analogous behavior of the pulsed signal is observed for any angle of laser beam incidence onto the film, as well as for any orientation of electrodes relative to the light incidence plane.

In the case of laser irradiation of nanographite films grown for deposition times from 20 to 50 min, an additional ultrashort photoelectric signal—ORP—appears at the leading front of the photoelectric signal. It is important to note that neither amplitude nor polarity of the ORP depend on the laser spot position on the sample film surface (Figs. 2b and 2c). At the same time, this signal exhibits characteristic orientational dependences, whereby the signal polarity and amplitude significantly depend on the light incidence angle and polarization and on the mutual spatial orientation of the film and electrodes relative to the plane of incidence [6, 7]. The ORP duration corresponded to FWHM ~ 20 ns (Fig. 2e), and its shape repeated the laser pulse envelope. An increase in the film growth time leads to complete vanishing of the photoelectric signal with a microsecond width (Fig. 1, curve *2*; Fig. 2d). The ORP amplitude U as a function of t behaves quite differently (Fig. 1, curve *3*): it exhibits a maximum for a film growth time of $t = 50$ min and, then, gradually decreases as t is further increased.

The appearance of a photoelectric signal between electrodes on a clean silicon substrate and on the substrates bearing films with thicknesses below 2 μm can be explained in terms of the well-known Dember effect, which originates from a difference in mobilities of the nonequilibrium electrons and holes generated in silicon under illumination. As the nanographite film thickness increases, the laser radiation power reaching the substrate is attenuated and the amplitude of this signal decreased. At a film thickness of 2.5 μm and above, the incident laser radiation is completely absorbed in the carbon film and the signal related to the Dember effect vanishes. This analysis implies that the ORP cannot be related to the silicon substrate and arises entirely due to the interaction of laser radiation with the nanographite film possessing a special structure (manifested, in particular, in the experiments with cold electron emission [9, 10]). The absence (or very small amplitude) of the ORP in the films with $h \le 1$ μm can be explained by the absence of these special properties in such films and by their small thickness. A decrease in the ORP amplitude observed for $h \ge 2.5$ μm is explained by a considerable decrease in the interelectrode resistance R (Fig. 1, curve *1*), which shunts the pulsed voltage across the nanographite film surface.

Thus, we have demonstrated that the maximum ORP amplitude in the nanographite films studied is observed at a film thickness of about 2.5 μm. In the films of smaller thicknesses, the ORP sharply decreases and there appears a photoelectric signal of microsecond duration, which is related to the silicon substrate. In films with thicknesses above 5 μm, the ORP also significantly decreases as a result of shunting.

In conclusion, we also report that our most recent experiments showed the possibility of using nanographite film photodetectors without any external bias voltage. Such detectors are capable of monitoring the shape of laser radiation pulses with durations shorter than 0.5 ns in a wavelength range from 0.266 to 5 μm. It should be noted that these values are by no means limiting characteristics of the proposed nanographite film photodetectors.

REFERENCES

1. Lee W. Tutt and A. Kost, Nature **356**, 225 (1992).
2. L. Smilowitz, D. McBranch, V. Klimov, *et al.*, Opt. Lett. **21**, 922 (1996).
3. H. I. Elim, W. Ji, G. H. Ma, *et al.*, Appl. Phys. Lett. **85**, 1799 (2004).
4. G. X. Chen, M. N. Hong, Q. He, *et al.*, Appl. Phys. A **79**, 1079 (2004).
5. N. N. Il'ichev, E. D. Obraztsova, S. V. Garnov, and S. E. Mosalaeva, Kvantovaya Élektron. (Moscow) **34**, 572 (2004).
6. G. M. Mikheev, R. G. Zonov, A. N. Obraztsov, and Yu. A. Svirko, Appl. Phys. Lett. **84**, 4854 (2004).

7. G. M. Mikheev, P. G. Zonov, A. N. Obraztsov, and Yu. P. Svirko, Pis'ma Zh. Tekh. Fiz. **30** (17), 88 (2004) [Tech. Phys. Lett. **30**, 750 (2004)].

8. G. M. Mikheev, R. G. Zonov, A. N. Obraztsov, *et al.*, Pis'ma Zh. Tekh. Fiz. **31** (3), 11 (2005) [Tech. Phys. Lett. **31**, 94 (2005)].

9. A. N. Obraztsov, A. P. Volkov, A. I. Boronin, *et al.*, Zh. Éksp. Teor. Fiz. **120**, 970 (2001) [JETP **93**, 846 (2001)].

10. A. N. Obraztsov, A. A. Zolotukhin, A. O. Ustinov, *et al.*, Carbon **41**, 836 (2003).

11. I. Yu. Pavlovskiĭ and A. N. Obraztsov, Prib. Tekh. Éksp., No. 1, 152 (1998).

12. A. N. Obraztsov, I. Yu. Pavlovsky, A. P. Volkov, *et al.*, Diamond Relat. Mater. **8**, 814 (1999).

13. G. M. Mikheev, D. I. Maleev, and T. N. Mogileva, Kvantovaya Élektron. (Moscow) **19**, 45 (1992) [Sov. J. Quantum Electron. **22**, 37 (1992)].

14. G. M. Mikheev, R. G. Zonov, D. G. Kalyuzhnyĭ, and A. Yu. Popov, Prib. Tekh. Éksp., No. 3, 164 (2003).

Translated by P. Pozdeev

Technical Physics Letters, Vol. 31, No. 7, 2005, pp. 564–566. Translated from Pis'ma v Zhurnal Tekhnicheskoĭ Fiziki, Vol. 31, No. 13, 2005, pp. 58–64.

Composition Profiles of Silicon–Silicon Oxide and Silicon–Rare Earth Oxide Structures

N. V. Latukhina[a,*] and V. M. Lebedev[b,]**

[a] *Samara State University, Samara, Russia*

[b] *St. Petersburg Institute of Nuclear Physics, Russian Academy of Sciences, Gatchina, Leningrad oblast, Russia*

*e-mail: * natalat@yandex.ru; ** lebedev@pnpi.spb.ru*

Received February 21, 2005

Abstract—Elemental composition profiles of the structures comprising the layers of dysprosium oxide (Dy_2O_3), lutetium oxide (Lu_2O_3), or silicon oxide (SiO_2 with Dy and Lu impurities) on silicon substrates have been studied by means of Rutherford backscattering spectrometry and nuclear reaction analysis. The structures were prepared by high-temperature diffusion in oxygen or air. The results of depth profiling are compared to the concentrations of electrically active impurities in the diffusion layers on silicon, which were determined from measurements of the capacitance–voltage characteristics and the surface resistance and from the data of transmission electron microscopy and X-ray diffraction. © *2005 Pleiades Publishing, Inc.*

In recent years, systems containing silicon in various forms (single crystal, porous, nanocrystalline particles in a silicon dioxide matrix, etc.) doped with rare earth (RE) elements have attracted much attention in view of the prospects for obtaining light-emitting structures on silicon substrates. However, methods developed for obtaining such structures practically do not involve such a well-known technology as diffusion doping. This is explained by the fact that the concentrations of RE ions introduced into silicon by diffusion are insufficiently high for ensuring effective luminescence [1]. Nevertheless, we believe that, in developing a practical technology of light-emitting structures, diffusion offers some advantages in comparison to the widely used ion implantation, since the former process takes place under more thermodynamically equilibrium conditions and is not accompanied by the formation of radiation defects in silicon.

This paper presents the results of investigation of the structures comprising single crystal silicon diffusion-doped by RE elements (dysprosium and lutetium) and silicon oxide containing impurities of the same RE elements.

Sample preparation. Single crystal silicon doped with RE elements was prepared by their diffusion from RE oxide films applied onto the initial crystal surface. The substrates were commercial *n*-type single crystal silicon plates. The diffusion process was carried out at a temperature of 1200–1300°C in air or in a dry oxygen atmosphere. The high-temperature treatment time was varied from 1 to 3 h. Under these conditions, several processes may simultaneously take place at the interface between silicon and RE oxide, which can lead to the formation of several phases with different compositions. In particular, this system features the formation of an interlayer consisting of mixed silicon and RE oxides and the interaction between RE elements and silicon with the formation of silicides and silicates. The substrate surface not covered by the RE oxide converts into silicon oxide, which is free of RE impurities.

As a result of the diffusion doping, the near-surface layer of silicon changes the character of the conductivity (from *n*- to *p*-type), because both RE elements under the conditions studied behave as acceptor impurities in silicon [1, 2].

The samples of silicon oxide containing RE elements were prepared by additional thermal oxidation of the surface of *p*-type silicon layers diffusion-doped by RE elements. This was achieved by heating the samples in air at a temperature from 1000 to 1270°C for several hours until the formation of SiO_2 layers with a thickness of 0.2–0.3 μm.

Investigation of the structure, composition, and properties of samples. In the case of single crystal silicon diffusion-doped by RE elements, the thickness of a diffusion layer was determined as the depth of the *p–n* junction. According to this, the diffusion layers had a thickness from 4 to 8 μm, depending on the temperature and duration of the diffusion annealing.

The elemental composition profiles in the sample structures were studied using methods of nondestructive microanalysis, including Rutherford backscattering spectrometry (RBS) and nuclear reaction analysis (NRA) with deuterons [3, 4]. The RBS sensitivity with respect to the RE element concentration in silicon is better than 0.01 at. % at an experimental accuracy of 2–3%. The accuracy of determination of the oxygen content in the samples with the aid of the NRA employing the $^{16}O(d, p)^{17}O$ reaction was within 5% at a sensitivity better than 0.1 at. %. The uncertainty of the depth

1063-7850/05/3107-0564$26.00

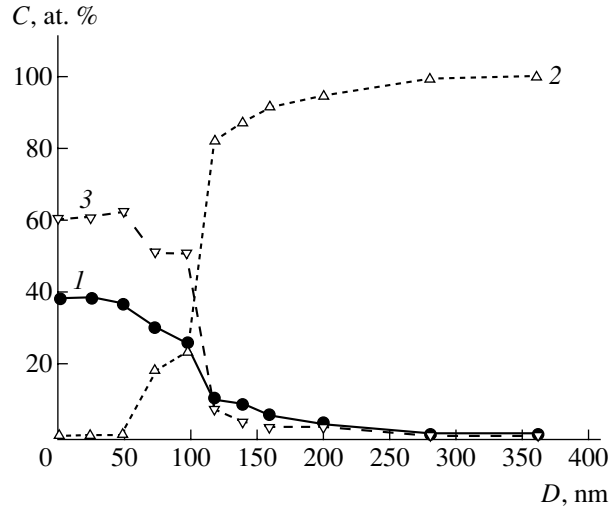

Fig. 1. Depth–concentration (*D*–*C*) profiles of elements in the Lu_2O_3–Si structure: (*1*) lutetium; (*2*) silicon; (*3*) oxygen.

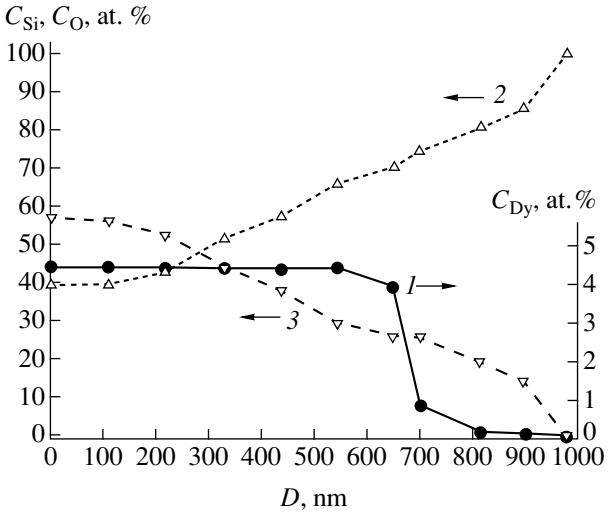

Fig. 2. Depth–concentration (*D*–*C*) profiles of elements in the Dy_2O_3–Si structure: (*1*) dysprosium; (*2*) silicon; (*3*) oxygen (arrows indicate the concentration scales).

determination was ~50 nm. By combining the RBS and NRA methods in one experiment, it is possible to determine with a high precision the concentrations of both heavy and light elements in the layers of silicon and RE oxides.

The study was carried out using an analytical complex for investigating materials by methods of nuclear microanalysis, which is based on the electrostatic accelerator of the St. Petersburg Institute of Nuclear Physics [5]. A sample was mounted in the vacuum chamber of this setup and irradiated with deuterons (particle energy, E_d = 0.9 MeV; beam diameter, 0.3 cm; beam current density on the target, up to 100 nA). The secondary particles were detected by a Si detector at an energy resolution of ΔE = 10 keV for E_α = 5.5 MeV, at a take-off angle of φ = 135° relative to the probing beam.

Figures 1–3 show the depth–concentration profiles for the main elements entering into the sample structures, which were calculated from the RBS data using a special program described in [3].

Figure 1 presents the profiles of lutetium, silicon, and oxygen in a Lu_2O_3–Si structure upon annealing for 1 h at 1194°C. As can be seen from these data, the total thickness of the oxide layer amounts to ~0.15 μm. This layer comprises a nearly stoichiometric lutetium oxide (Lu_2O_3) with a thickness of ~0.07 μm and a transition oxide interlayer with a thickness of ~0.08 μm. In deeper layers, the content of silicon exceeds 80 at. %, and these regions can be considered as silicon enriched with oxygen and lutetium. The concentration of lutetium at a depth of 0.14 μm from the silicon interface (i.e., 0.28 μm from the outer surface of the structure) falls below 0.5 at. %.

Figure 2 presents the depth–concentration profiles of elements in the surface layers of silicon doped with dysprosium. The sample was prepared by removal of the dysprosium oxide layer from a Dy_2O_3–Si structure upon annealing for 3 h at 1300°C. In this sample, the boundary between a mixed oxide layer and the silicon substrate can be identified only by a sharp step on the dysprosium profile (right-hand scale of concentrations), since the silicon and oxygen concentrations (left-hand scale) smoothly vary from the surface down to a depth of about 1 μm. In contrast, the dysprosium concentration is virtually constant (~4.4%) to a depth of 0.6 μm, then it exhibits a sharp drop at a depth of 0.7 μm, and eventually decreases to zero at 1 μm. Therefore, the thickness of a mixed oxide layer can be

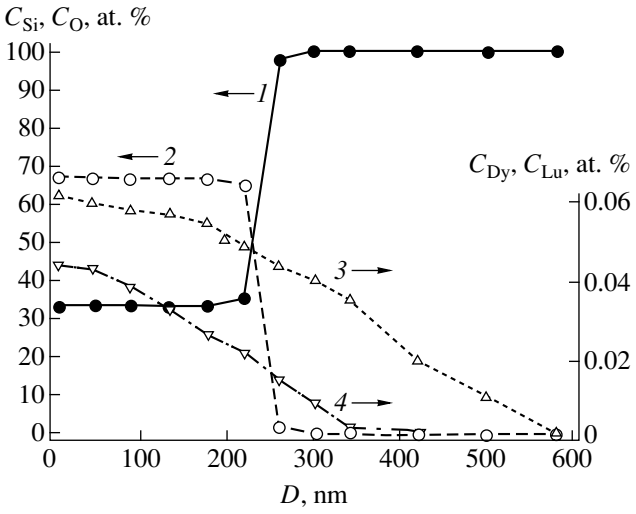

Fig. 3. Depth–concentration (*D*–*C*) profiles of elements in the SiO_2(Dy)–Si and SiO_2(Lu)–Si structures: (*1*) silicon; (*2*) oxygen; (*3*) Dy in SiO_2(Dy)–Si; (*4*) Lu in SiO_2(Lu)–Si (arrows indicate the concentration scales).

estimated at 0.65 μm, and the thickness of a silicon layer enriched with dysprosium and oxygen amounts approximately to 0.35 μm.

The Lu_2O_3–Si and Dy_2O_3–Si structures were also characterized by determining the concentrations of electrically active RE ions, which were assumed to be equal to the hole density and found from an analysis of the capacitance–voltage characteristics and the surface resistance of silicon. These data were obtained in the course of the sequential layer removal by etching and measurement of the Hall mobility of charge carriers. The results of these measurements showed that the hole density in the surface layers did not exceed 10^{17} cm^{-3} (i.e., 0.01%) and gradually decreased with increasing depth down to several microns.

Therefore, we may suggest that a considerable proportion of RE atoms are concentrated in a thin (a fraction of a micron) near-surface layer of silicon and occur in an electrically inactive state. This conclusion was confirmed by the results of structural analysis of the surface layers of silicon diffusion-doped with RE elements, which was performed by methods of transmission electron microscopy (TEM) and X-ray diffraction (XRD) [6]. The TEM images of the surface of the diffusion-doped layer of silicon revealed objects with characteristic dimensions from 0.02 to 0.15 μm. The phase analysis using the patterns of electron microdiffraction from the particles extracted from these samples confirmed the presence of RE oxides in all cases.

Thus, we may infer that the simultaneous diffusion of RE elements and oxygen from an RE oxide film into silicon is accompanied by their interaction, which leads to the formation of RE oxide clusters in the crystalline silicon matrix.

As for silicon oxide containing RE elements, Fig. 3 presents the depth–concentration profiles of silicon and oxygen (left-hand concentration scale) in the SiO_2–Si structures with silicon oxide formed by thermal oxidation of the surface of diffusion-doped silicon. In the samples doped with lutetium, as well as in those doped with dysprosium, the silicon oxide layer thickness could be readily determined from the Si and O profiles and amounted to ~0.2 μm, whereas the RE element concentrations smoothly decayed down to a depth of 0.6 μm for Dy and 0.4 μm for Lu (right-hand scale).

A comparison of the depth–concentration profiles for dysprosium in Figs. 2 and 3 shows that RE oxide clusters formed in the silicon matrix in the course of oxidation possess a rather high mobility and are distributed between the oxide layer and silicon. Apparently, a part of these clusters exhibits decomposition, since the oxygen concentration in the surface layer of silicon in these structures is lower than the RE concentration.

Conclusion. The results of our investigation showed that the doping of silicon with RE elements by diffusion from RE oxide films leads to a concentration of RE elements in the surface layer of silicon reaching several hundreds ppm, which is equivalent to 10^{20}–10^{21} cm^{-3}. A part of these RE atoms diffuses via lattice sites of the silicon crystal structure down to a depth of several microns and behaves as an acceptor impurity in silicon. However, a much greater part of the RE atoms are retained in the near-surface layer of silicon with a thickness on the order of several tenths of a micron. These atoms occur in an electrically inactive state and form RE oxide inclusions with dimensions up to 0.15 μm [6]. During thermal oxidation of the diffusion-doped silicon surface, the RE impurity is redistributed between the oxide layer and silicon bulk, which results in smoother RE element profiles in such structures.

REFERENCES

1. N. A. Sobolev, Fiz. Tekh. Poluprovodn. (St. Petersburg) **29**, 1153 (1995) [Semiconductors **29**, 595 (1995)].
2. A. I. Borisenko *et al.*, Dokl. Akad. Nauk SSSR **262**, 1409 (1982).
3. G. Gavrilov, A. Krivchitch, and V. Lebedev, Nucl. Instrum. Methods Phys. Res. A **5156**, 108 (2003).
4. A. E. Gamarts, V. M. Lebedev, V. A. Moshnikov, and D. B. Chesnokova, Fiz. Tekh. Poluprovodn. (St. Petersburg) **38**, 1195 (2004) [Semiconductors **38**, 1160 (2004)].
5. V. M. Lebedev, Yu. G. Luk'yanov, and V. A. Smolin, in *Proceedings of the 13th International Conference on Electrostatic Accelerators, Obninsk, 1999*, pp. 60–66.
6. L. V. Zhuravel', N. V. Latukhina, and E. Yu. Blytushkina, Izv. Vyssh. Uchebn. Zaved., Mater. Élektron. Tekh. **3**, 72 (2004).

Translated by P. Pozdeev

Technical Physics Letters, Vol. 31, No. 7, 2005, pp. 567–569. Translated from Pis'ma v Zhurnal Tekhnicheskoĭ Fiziki, Vol. 31, No. 13, 2005, pp. 65–70.

Recombination X-ray Radiation from Plasma Liners

V. I. Oreshkin*, R. B. Baksht, A. Yu. Labetskiĭ, N. A. Ratakhin, A. G. Russkikh, S. A. Chaikovsky, A. V. Fedyunin, and A. V. Shishlov

Institute of High-Current Electronics, Siberian Division, Russian Academy of Sciences, Tomsk, Russia

** e-mail: oreshkin@ovpe.hcei.tsc.ru*

Received February 21, 2005

Abstract—The possibility of creating a high-power X-ray source based on the recombination radiation mechanism has been studied and analyzed. The recombination X-ray radiation from neon, aluminum, and argon was obtained in experiments with plasma liners performed on the GIT-12 setup using a current pulse amplitude of ~2.5 MA and a leading pulse front width of ~300 ns. The obtained results show that the recombination mechanism of X-ray generation offers good prospects for the development of a high-power X-ray source with photon energies in the 7–20-keV range. © *2005 Pleiades Publishing, Inc.*

At present, plasma liners or fast Z-pinch plasmas are widely used as high-power (up to 200 TW [1]) soft X-ray sources. The spectral range of such sources in terms of the photon energies typically extend from 0.1 up to about 7 keV. X-ray photons in the range of higher energies (>20 keV) are usually generated with the aid of high-power electron beams stopped in cold condensed targets. The interval from 7 to 20 keV is not covered by any of the existing types of terawatt sources. A comparative analysis of the two available types of sources (based on the Z-pinch plasmas and electron beams) [2] showed that real prospects for the creation of a high-power X-ray source with photon energies in the 7–20-keV range are offered only by the Z-pinch schemes. The most attractive feature of such systems is related to the prospects of exciting radiation of the spectral lines due to electron transitions in the *K* shells, since it is principally possible to insure that a considerable proportion of the energy supplied to the Z-pinch will be converted into radiation of this very type. However, the actual efficiency of conversion of the plasma generator energy into the energy of radiation in the 7–20-keV range is very low, since this energy interval corresponds to the *K*-shell transitions in atoms with relatively large atomic numbers ($Z \sim 28–40$) and the *K*-shell excitation requires overcoming a high "radiation" barrier related to emission of the *L* and *M* lines.

In order to overcome this difficulty, it was suggested [3, 4] to use the recombination radiation of hydrogen- and helium-like ions of elements with lower *Z*. The recombination continuum radiation from these ions falls in the range of energies above those of all spectral lines, which allows *Z* to be decreased. Therefore, despite a somewhat lower efficiency of energy conversion into the recombination continuum radiation than into the *K*-shell emission, the former process can be energetically more favorable due to a decrease in the "radiation" barrier. Moreover, the *K*-shell emission yield increases proportionally to the first power of *Z*, while the emissivity in the recombination continuum is proportional to the fifth power of *Z*.

In order to evaluate the recombination radiation yield, we have previously developed an analytical model [3, 4] based on assumptions similar to those used by Mosher *et al.* [5] (MQK model) for the description of *K*-shell emission. Our analytical model assumes that (i) the plasma is fully ionized, (ii) the emission time is determined by the time of hydrodynamic plasma confinement; (iii) the plasma is optically transparent at frequencies corresponding to the photon energies >7 keV; and (iv) a part of the plasma kinetic energy E_{kin} converted into the internal energy E_{in} is determined as $E_{in} = \varepsilon E_{kin}$, where the factor ε takes into account the "radiation" barrier effects. Using the model [3, 4], it is possible to evaluate the maximum radiation yield and the optimum (from the standpoint of the recombination radiation yield) Z-pinch temperature, mass, and initial radius for a given substance with the atomic number *Z*, a required photon energy range $h\nu > E_0$, and a preset generator current *I*.

The dependences of the optimum Z-pinch temperature on *Z* for $h\nu > 3$, 7, and 10 keV are presented in Fig. 1. As can be seen, the optimum electron temperature in the pinch for $h\nu > E_0$ and small *Z* decreases as $T_{opt} = (1/3)(E_0 - RyZ^2)$, where $Ry = 13.6$ eV is the ionization potential for hydrogen. This decrease in T_{opt} is related to the fact that the energy of a photon emitted upon trapping a free electron in a bound state is equal to the sum of the kinetic energy of the free electron and its potential energy in the bound state (ionization energy). The latter value increases with *Z*, and, hence, the required kinetic energy of free electrons (i.e., their temperature) decreases. However, this decrease is only possible until the plasma recombination onset, because then the optimum temperature for large-*Z* substances

1063-7850/05/3107-0567$26.00 © 2005 Pleiades Publishing, Inc.

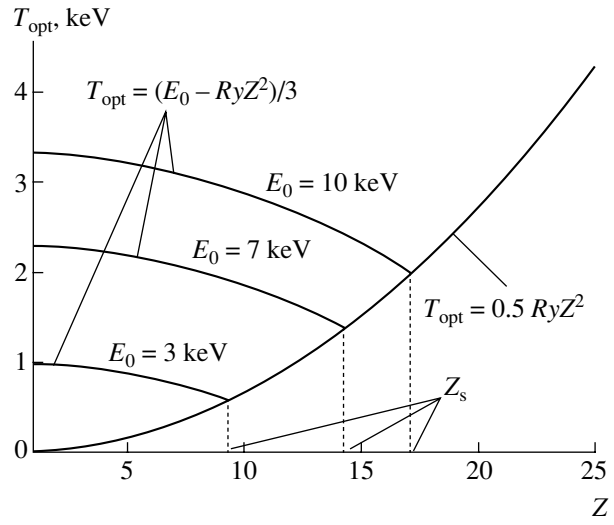

Fig. 1. A plot of the optimum plasma temperature T_{opt} versus atomic number Z for recombination radiation in the photon energy range $h\nu > 3$, 7, and 10 keV.

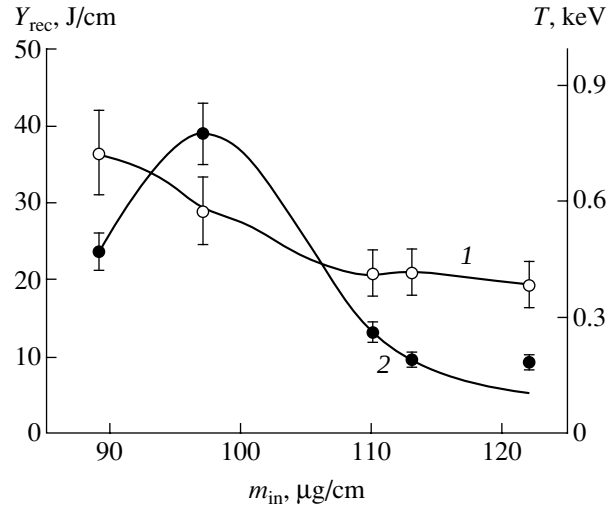

Fig. 2. Plots of the (*1*) plasma temperature and (*2*) recombination radiation yield versus inner shell mass m_{in} for the optimum two-cascade neon Z-pinch configuration (outer shell radius, 4 cm; inner shell radius, 1 cm; outer shell mass, 70 μg/cm).

begins to increase as $T_{opt} \sim RyZ^2$. Therefore, for a given $h\nu > E_0$, there is a certain atomic number Z_s (see Fig. 1) for which the T_{opt} value is minimum. Although the recombination radiation yield according to our model [3, 4] always increases with Z, the maximum yield has to be expected for substances with atomic numbers close to Z_s. A further increase in Z (i) requires an increase in the pinch temperature (which encounters experimental difficulties) and (ii) leads to enhancement of the "radiation" barrier effects.

We have compared the recombination radiation yield in the photon energy range $h\nu > E_0$ (for $Z = Z_s$) evaluated using our model to estimates of the *K*-shell emission yield according to the MQK model [5] for the same range. This comparison showed that the ratio of the recombination radiation yield to that of the *K*-shell emission increases with the photon energy as $\sim E_0^{1.86}$. Therefore, use of the recombination radiation (even with neglect of the "radiation" barrier effects) becomes energetically favorable for the generation of photons with energies ~20 keV. Obviously, allowance for the "radiation" barrier effects must decrease this threshold. In addition, the generation of recombination radiation requires a lower temperature of the plasma. Indeed, for the *K*-shell emission, the optimum plasma temperature is $\approx E_0/3$ [5], whereas the optimum temperature for the recombination continuum radiation is $\approx E_0/5$. Moreover, the atomic number of a substance whose electron transitions can provide for the *K*-shell emission in the desired photon energy range is 1.8 times that necessary for the recombination radiation. Thus, the *K*-shell emission in the 7–20-keV range requires using substances with atomic numbers within ~28–40, while the recombination continuum radiation in this energy range is possible for $Z \sim 18$–22.

The recombination radiation yield was previously measured in a single experiment [6] on the contraction of two-cascade argon liners, which was performed on the Z-generator at the Sandia National Laboratory (USA) using load current amplitudes up to 17 MA [1]. We have performed systematic investigations on the GIT-12 setup using a current pulse amplitude of ~2.5 MA and a leading pulse front width of ~300 ns [7]. It should be noted that significant recombination radiation yields can be obtained only using setups with currents on a megaampere level. For this reason, the recombination radiation yields achieved with the GIT-12 system are definitely below the *K*-shell emission yields in the same energy range. For this reason, the main aim of these experiments was to verify the model concepts [3, 4] and to determine the optimum (from the standpoint of the recombination radiation yield) parameters of plasma liners and compare these values to the optimum parameters of liners predicted for the *K*-shell emission.

The experiments using the GIT-12 generator for obtaining the recombination radiation were performed with neon, aluminum, and argon plasmas. All of these experiments were conducted with two-cascade liners. In the experiments with argon and neon, these were two-cascade gas liners, while, in the case of aluminum, the outer cascade was a gas shell and the inner cascade was a wire array. The experimental results are listed in the table, which shows the maximum recombination radiation yields measured on the GIT-12 setup. A comparison of the measured data to the values predicted by the model [3, 4] shows a good agreement between theory and experiment.

We have most thoroughly studied the case of two-cascade neon liners and determined the optimum (from

Comparison of the recombination radiation yields expected according to the model [4] and those obtained in experiments on the GIT-12 setup in the range of photon energies $h\nu > E_0$

Substance	E_0, keV	Expected yield, J/cm (for $\varepsilon = 0.3$)	Experimental yield, J/cm
Neon	3.15	30	40 ± 5
Aluminum	3.15	85	45 ± 5
Argon	5.0	50	30 ± 10

the standpoint of the recombination radiation yield) gas shell parameters (mass and radius) and the electron temperature in the final implosion stage. The temperature was determined from the slope of the continuum spectrum [8] plotted as the continuum emission intensity versus photon energy. Figure 2 shows plots of the plasma temperature and recombination radiation yield versus inner shell mass for the optimum configuration (outer shell radius, 4 cm; inner shell radius, 1 cm; outer shell mass, 70 μg/cm). As can be seen from these data, the maximum yield corresponds to the optimum plasma temperature predicted by the model [3, 4] (Fig. 1). Note that the optimum liner mass for the recombination radiation is 10–15% lower than the optimum value for the *K*-shell emission.

To summarize, the results of our experiments on the GIT-2 setup show that the recombination mechanism of X-ray generation offers good prospects for the development of a high-power X-ray source with photon energies in the 7–20-keV range.

Acknowledgments. This study was supported by the Defense Threat Reduction Agency (USA) (DTRA project no. 01-02-P-0099) and the Russian Foundation for Basic Research, (project no. 05-02-16662). One of the authors (A.V. S.) gratefully acknowledges support from the Russian Science Support Foundation.

REFERENCES

1. R. B. Spielman, C. Deeney, G. A. Chandler, *et al.*, in *Proceedings of the 4th International Conference on Dense Z-Pinches, Vancouver, 1997*, Ed. by N. Pereira, J. Davis, and P. Pulsifer; AIP Conf. Proc. **409**, 101 (1997).
2. N. A. Ratakhin, Izv. Vyssh. Uchebn. Zaved., Fiz. **40** (12), 92 (1997).
3. V. I. Oreshkin, A. L. Velikovich, J. Davis, *et al.*, Bull. Am. Phys. Soc. **46** (8), 317 (2001).
4. A. L. Velikovich, J. Davis, V. I. Oreshkin, *et al.*, Phys. Plasmas **8**, 4509 (2001).
5. D. Mosher, N. Qi, and M. Krishnan, IEEE Trans. Plasma Sci. **26**, 1052 (1999).
6. P. Coleman, M. Krishnan, J. P. Apruzese, *et al.*, Bull. Am. Phys. Soc. **48** (7), 336 (2003).
7. S. P. Bugaev, A. M. Volkov, A. A. Kim, *et al.*, Izv. Vyssh. Uchebn. Zaved., Fiz. **40** (12), 38 (1997).
8. S. A. Chaikovsky, N. A. Zhidkova, A. V. Fedyunin, *et al.*, in *Proceedings of the 13th International Symposium on High Current Electronics, Tomsk, 2004*, Ed. by B. Kovalchuk and G. Remnev, pp. 375–379.

Translated by P. Pozdeev

Technical Physics Letters, Vol. 31, No. 7, 2005, pp. 570–572. Translated from Pis'ma v Zhurnal Tekhnicheskoĭ Fiziki, Vol. 31, No. 13, 2005, pp. 71–77.

A New Method of Dark Resonance Excitation on D_2 Line in ^{87}Rb Vapor

G. A. Kazakov*, B. G. Matisov, J. Delporte, and G. Mileti

St. Petersburg State Polytechnic University, St. Petersburg, 195251 Russia
National Space Research Center (CNES), 31401 Toulouse, France
Neuchâtel Cantonal Observatory, CH-2000 Neuchâtel, Switzerland
** e-mail: kazakov@quark.stu.neva.ru*

Received March 9, 2005

Abstract—A new method based on optical pumping is proposed for increasing the parameters of dark resonance excitation on D_2 line in ^{87}Rb vapor. The pumping is provided by linearly polarized two-frequency laser radiation propagating in the direction perpendicular to the probing field directed along the cell with atomic rubidium vapor. This method significantly improves the dark resonance parameters as compared to the case of pumping by a circularly polarized field. Qualitative considerations are confirmed by the results of numerical calculations. © *2005 Pleiades Publishing, Inc.*

Quantum frequency standards find increasing use both in basic science and in technological applications. In recent years, there has been an explosion of interest in these standards, which is related to the development of all-optical quantum clock based on the coherent population trapping (CPT) phenomenon.

The CPT for atoms interacting with a resonance field is well known (see review [1] and references therein). Investigations devoted to the creation of a CPT-based atomic clock using a cell with alkali metal vapor have been reported in [2–4]. The main advantage of this clock consists in that the selected standard transition is excited by purely optical methods, which makes it possible to create small-sized devices with low energy consumption due to the absence of a microwave resonator. However, the all-optical atomic clock development encounters certain problems related to the optimization of signal parameters (amplitude, width, contrast, and slope of the amplitude–frequency characteristic).

This paper describes a new method that provides for a significant improvement of the signal characteristics. The proposed method is based on the use of two-frequency optical pumping for accumulating atoms on the working sublevels.

The working sublevels in the atomic clock are the Zeeman levels with the magnetic moment projection $m = 0$ on two hyperfine components of the ground state in alkali metal atoms, and the transition between these sublevels is conventionally called standard. In ^{97}Rb atoms, such working sublevels are $|1\rangle = |F = 1, m = 0\rangle$ and $|2\rangle = |F = 2, m = 0\rangle$ (Fig. 1). The coherence between these levels is provided by two-photon Raman transitions induced by circularly polarized correlated two-frequency (ω_1, ω_2) radiation. It is a common practice to use copropagating running waves and to form a spectroscopic signal proportional to the absorption depending on the frequency difference $\omega_1 - \omega_2$. When the difference is varied in the vicinity of the hyperfine splitting frequency Δ_{hfs} in the ground state, the absorption intensity exhibits a narrow trough called dark resonance, whose width is determined by the coherence relaxation rate in the ground state and by the field parameters.

One of the main parameters determining the stability of a frequency standard (atomic clock) is the slope S of its amplitude–frequency characteristic [5–8]:

$$S = \left|d^2 I/d\Omega^2\right|_{\Omega = 0},$$

where I is the photodetector current and $\Omega = [\Delta_{hfs} - (\omega_1 - \omega_2)]/2$ is the two-photon detuning. By order of magnitude, the slope S is evaluated as the ratio of the amplitude to the square width of the resonance [6].

In developing the quantum frequency standards, considerable attention is devoted to determining the optimum working conditions so as to obtain the maximum S value. One possible way of such optimization is to select a proper excitation scheme. An alkali metal atom interacting with a unidirectional circularly polarized field always has a blank level (called "pocket"), which is a Zeeman sublevel of the ground state with the maximum (for σ^+ polarization of the laser field) or minimum (for σ^- polarization) magnetic moment projection. Atoms accumulated in the "pocket" fall out of the process of coherence formation (because of the lack of cyclic interaction) between the working sublevels $|1\rangle$ and $|2\rangle$, which leads to a sharp drop in the signal amplitude (i.e., in the difference between the values of

1063-7850/05/3107-0570$26.00 © 2005 Pleiades Publishing, Inc.

absorption without and with the two-photon resonance) and in the signal contrast (i.e., in the ratio of the amplitude to the total absorption far from the resonance).

One possible solution to this problem consists in using counterpropagating light waves with opposite circular polarizations [4]. In this case, the aforementioned "pocket" is absent, but the resonance amplitude exhibits a significant spatial variation with a period of $\pi/(k_1 - k_2)$, where $k_j = 2\pi/\lambda_j$ is the wavenumber of a light field with frequency ω_j. This variation is related to the difference of wavelengths λ_1 and λ_2 for various frequency components. In particular, for ^{87}Rb atoms this period amounts to $\pi/(k_1 - k_2) \approx 2$ cm. For this reason, no sharp increase in the dark resonance amplitude is observed in a cell with dimensions $L \geq \pi/(k_1 - k_2)$, because of the spatial averaging. In a small cell with dimensions $L \ll \pi/(k_1 - k_2)$, an important role is played by the relaxation on walls. The influence of this factor can be reduced by increasing the buffer gas pressure (e.g., to 150 Torr for a 12-mm^3 cell [9]), which leads to a decrease in amplitude and a sharp broadening of the resonance. Therefore, this scheme provides only a small (approximately by a factor of 1.4 [9]) increase in the amplitude as compared to that in the case of circularly polarized waves.

In order to ensure the cyclic interaction and increase in the amplitude, contrast, and slope of the resonance, we propose a new method based on the use of two-photon optical pumping (Fig. 1). Let a two-component π-polarized laser field (pumping field) act on ^{87}Rb atoms in the cell (Fig. 1a):

$$\mathbf{E}_{\text{pump}} = \frac{\mathbf{e}}{2}(E_3 \exp[i(k_3 x - \omega_3 t)] + E_4 \exp[i(k_4 x - \omega_4 t)]) + \text{c.c.},$$

where one component is tuned in resonance with the $|F = 2\rangle \longrightarrow |F' = 2\rangle$ transition, and the other component, with the $|F = 1\rangle \longrightarrow |F' = 1\rangle$ transition (D_1 line in Fig. 1b). In this case, there are no induced transitions from the levels $|F = 1, m = 0\rangle$ and $|F = 2, m = 0\rangle$ because the Clebsch–Gordan coefficients C^{10}_{1010} and C^{20}_{2010} (entering into the corresponding matrix elements of the dipole moment operator) are zero. As a result of the spontaneous transitions and those induced by the pumping field, all atoms will be accumulated on the working sublevels $|1\rangle$ and $|2\rangle$. Note also that the pumping field components can be uncorrelated.

Now let us switch on a weak (relative to the pumping field) two-component σ^+ polarized field (probe field, Fig. 1a) tuned in resonance with the transitions from the ground state to the excited state with $J' = 3/2$ (Fig. 1b):

$$\mathbf{E}_{\text{probe}} = \frac{\mathbf{e}_{+1}}{2}(E_1 \exp[i(k_1 z - \omega_1 t)] + E_2 \exp[i(k_2 z - \omega_2 t)]) + \text{c.c.},$$

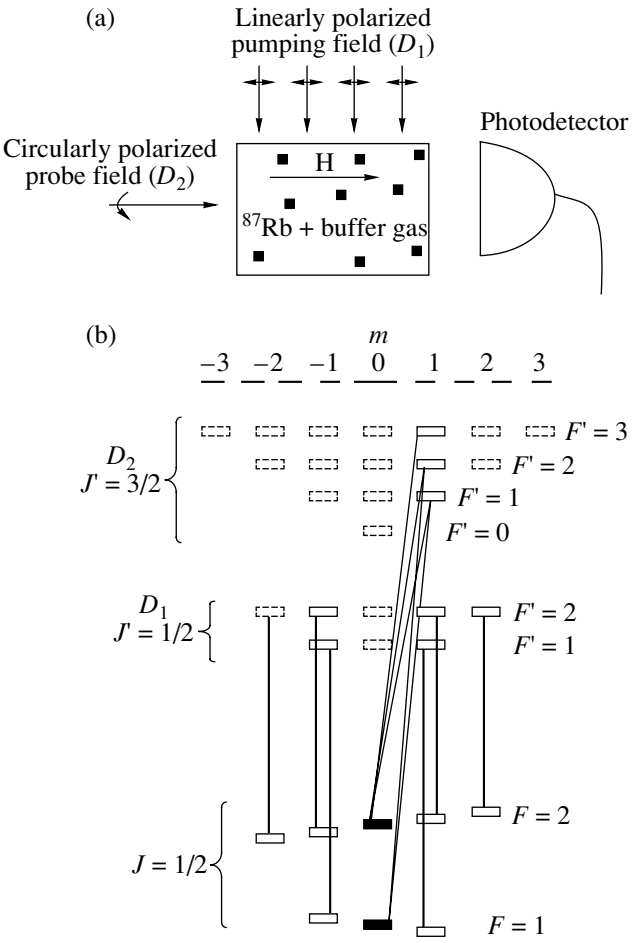

Fig. 1. Diagrams illustrating the interaction of ^{87}Rb atoms with laser fields: (a) spatial arrangement of the cell and the fields; (b) scheme of transitions in ^{87}Rb atoms induced by the optical fields (vertical lines indicate the transitions induced by the pumping field; sloped lines show the transitions induced by the σ^+ polarized field; black bars indicate the working sublevels of the ground state).

where

$$\mathbf{e}_{+1} = -\frac{1}{\sqrt{2}}(\mathbf{e}_x + i\mathbf{e}_y).$$

Variation of the frequency difference in the vicinity of Δ_{hfs} will give rise to a dark resonance whose the amplitude and contrast are much greater than those in the absence of pumping. This gain is related to the fact that, in our case, all atoms occur on the working sublevels.

We have performed numerical calculations of the parameters of dark resonance for ^{87}Rb atoms in a cell with a buffer gas at room temperature and a pressure of 10 Torr. The calculation was performed with allowance for the real hyperfine structure and Zeeman structure of energy levels, as well as for the optical pumping effects related to the radiation relaxation. We also took into account that the hyperfine components of the second

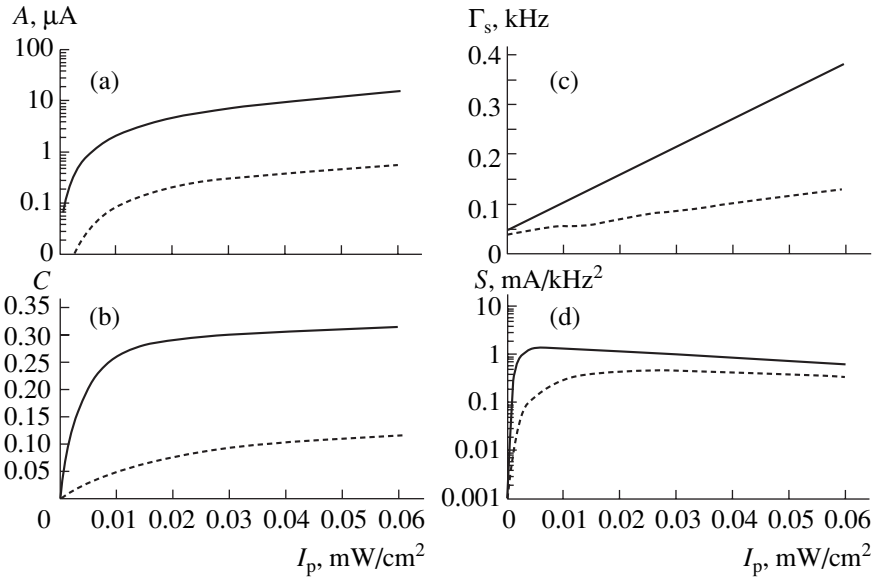

Fig. 2. Plots of the dark resonance (a) amplitude A, (b) contrast C, (c) width Γ_s, and (d) slope S versus pumping field intensity. Solid curves refer to the proposed scheme with laser pumping (I_0 = 20 mW/cm^2) noncollinear with the probing field, whereby not less that 90% of ^{87}Rb atoms occur on the working sublevels; dashed curves refer to the case of the atomic system interacting with the σ^+ polarized probing wave on D_1 line without optical pumping.

excited state $|J' = 3/2\rangle$ are not spectrally resolved as a result of the Doppler broadening (Fig. 1b).

Figure 2 shows the results of calculations that gave the values of amplitude A, contrast C, width Γ_s, and slope S as functions of the pumping field intensity I_p. For the comparison, Fig. 2 also shows the values of parameters calculated for the D_1 line in the case of a circularly polarized light in the absence of optical pumping. As can be seen, the use of noncollinear optical pumping provides for a significant increase in the contrast (32% against 12% for σ^+), amplitude, and slope of the dark resonance.

The calculations performed for noncollinear optical pumping corresponded to the case with the probing field components tuned in the vicinity of the resonance with the transitions between levels $|F = 1, J = 1/2\rangle \longrightarrow |F' = 2, J' = 3/2\rangle$ and $|F = 2, J = 1/2\rangle \longrightarrow |F' = 2, J' = 3/2\rangle$ (in other cases, the results are somewhat worse). The rate of the transverse relaxation in the ground state was $\Gamma = 2 \times 10^2$ s^{-1}, and the intensities of both components in the probing and pumping fields were assumed to be equal.

As can be seen from Fig. 2, the slope reaches a maximum for a probe field intensity I_p = 0.01 mW/cm^2 and rather weakly changes when I_p is varied within 0.005–0.015 mW/cm^2. A further increase in I_p is accompanied by a sharp increase in the signal width Γ_s at moderate increase in the contrast. If the intensity of pumping is reduced, the resonance width ceases to decrease and depends predominantly on Γ.

The short-time stability σ_y calculation using formulas [7, 8] for the quantum frequency standard employing the proposed scheme yields $\sigma_y \le 10^{-13}/\sqrt{\tau}$ for a cell volume of about 10 cm^3.

Acknowledgments. This study was supported in part by the INTAS–CNES (grant no. 03-53-5175) and the Ministry of Education and Science of the Russian Federation (project no. UR.01.01.287).

REFERENCES

1. B. D. Agap'ev, M. B. Gornyi, B. G. Matisov, and Yu. V. Rozhdestvenskiĭ, Usp. Fiz. Nauk **163** (9), 1 (1993) [Phys. Usp. **36**, 763 (1993)].
2. J. Kitching, S. Knappe, N. Vukicevic, *et al.*, IEEE Trans. Instrum. Meas. **49**, 1313 (2000).
3. M. Merimaa, T. Lindvall, I. Tittonen, and E. Ikonen, J. Opt. Soc. Am. B **20**, 273 (2003).
4. A. V. Taichenachev, V. I. Yudin, V. L. Velichanskiĭ, *et al.*, Pis'ma Zh. Éksp. Teor. Fiz. **80**, 265 (2004) [JETP Lett. **80**, 236 (2004)].
5. M. B. Gornyĭ and B. G. Matisov, Radiotekh. Élektron. (Moscow) **28**, 1783 (1983).
6. M. B. Gornyĭ and B. G. Matisov, Zh. Tekh. Fiz. **54**, 1881 (1984) [Sov. Phys. Tech. Phys. **29**, 1106 (1984)].
7. M. B. Gornyĭ, B. G. Matisov, G. M. Smirnova, and V. I. Khutorshchikov, Zh. Tekh. Fiz. **57**, 740 (1987) [Sov. Phys. Tech. Phys. **32**, 448 (1987)].
8. J. Vanier and C. Audoin, *The Quantum Physics of Atomic Frequency Standards* (Hilger, Bristol, 1989).
9. S. V. Kargapoltsev, J. Kitching, L. Hollberg, *et al.*, Laser Phys. Lett. **1**, 495 (2004).

Translated by P. Pozdeev

Technical Physics Letters, Vol. 31, No. 7, 2005, pp. 573–577. Translated from Pis'ma v Zhurnal Tekhnicheskoĭ Fiziki, Vol. 31, No. 13, 2005, pp. 78–88.

Increasing Laser Excitation Power Induces Large Blue Shift of the Photoluminescence Peak of Quantum Wells in Gallium Nitride

M. A. Jacobson, D. K. Nelson, O. V. Konstantinov, and A. V. Matveentsev

Ioffe Physicotechnical Institute, Russian Academy of Sciences, St. Petersburg, 194021 Russia

Received March 3, 2005

Abstract—It is experimentally demonstrated that, as the output power density of a nitrogen laser is increased from 10 to 1000 kW/cm^2, a peak in the photoluminescence spectrum of quantum wells (QWs) in GaN shifts by approximately 150 meV. This behavior cannot be interpreted within the framework of the ideal QW model. The observed phenomenon is theoretically explained by the presence of a "tail" in the localized density of states in the QW bandgap and by the filling of bands in the QW by nonequilibrium photogenerated charge carriers. A phenomenological expression for the density of states is proposed, which takes into account the tail in the localized density of states and provides qualitative agreement between theoretical and experimental spectra.

Introduction. Recently, Shapiro *et al.* [1] reported for the first time that an increase in the incident light power may lead to a very large blue shift of the photoluminescence (PL) peak of quantum wells (QWs) in gallium nitride (GaN), which is accompanied by broadening of the emission band. This paper is devoted to the investigation of this phenomenon. Figure 1 shows a family of the experimental PL spectra measured for various intensities of laser radiation incident onto a QW with the composition $In_{0.2}Ga_{0.8}N/GaN$. Figure 2 presents the corresponding family of theoretical spectral curves calculated for the same laser excitation powers within the framework of the ideal QW model. As can be seen, the model predicts only the second effect. A characteristic feature of the theoretical family is a sharp step at the red (long-wavelength) edge of the spontaneous emission spectrum. Such a step in the emission spectrum must correspond to a sharp edge in the density of states (DOS) of the ideal QW. According to the theory, the maximum of the spontaneous emission spectrum always adheres to this step and exhibits no blue shift (Fig. 2).

It should be noted that a sharp steplike long-wavelength edge was never observed in the experimental PL spectra of QWs. Despite the absence of this step, the blue shift is usually also not observed. For example, the red edge was absent in the PL spectra of QWs in the $GaN/Al_xGa_{1-x}N$ structures studied in our recent work [2]. However, the blue shift was also very weak, namely, not exceeding 10 meV, despite a change in the laser pumping intensity by three orders of magnitude. Apparently, there was a small tail in the localized DOS, which was sufficient to smear the step in the PL spectrum but not to produce a large blue shift. We believe that such a behavior was related to the fact that QWs in the structures studied consisted of pure GaN. In contrast, QW with the composition $In_{0.2}Ga_{0.8}N/GaN$ may exhibit strong fluctuations in the concentration of

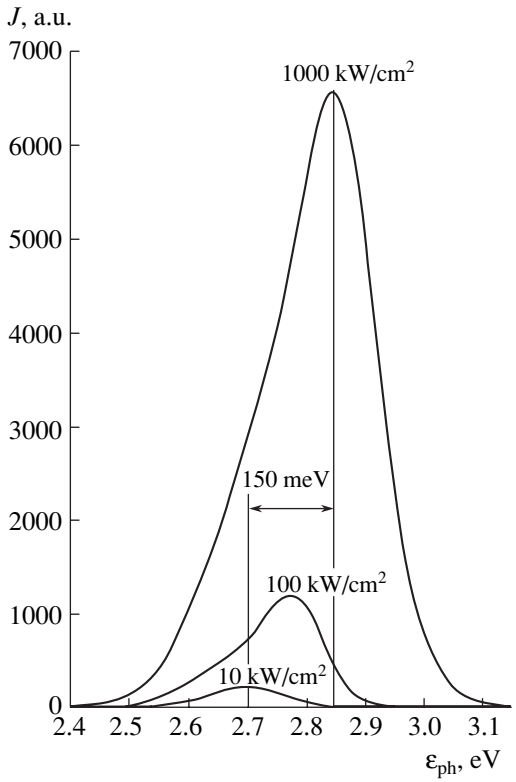

Fig. 1. Experimental PL spectra of $In_{0.2}Ga_{0.8}/GaN$ QWs with d = 30 Å measured at T = 80 K for various power densities of N_2 laser radiation (indicated at the curves). The distance between vertical lines indicates a large blue shift of 0.15 eV.

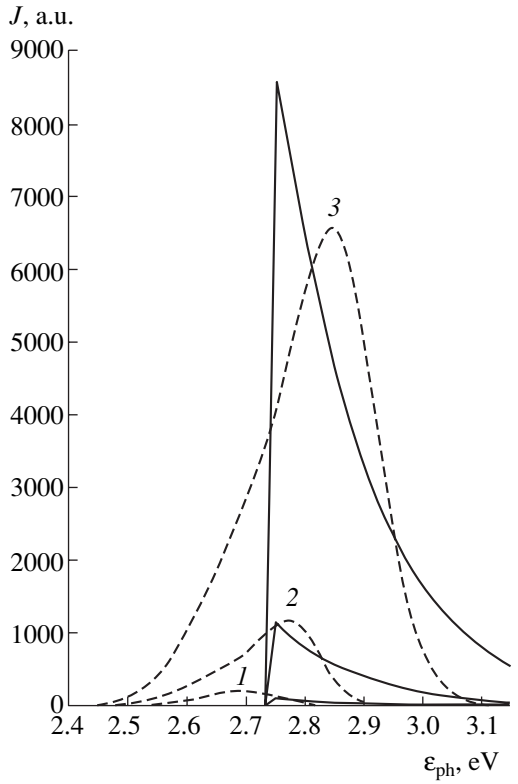

Fig. 2. Theoretical PL spectra calculated for a QW with E_g = 2.74 eV using formula (8) with neglect of the DOS tail (solid curves) for θ = 14 meV, exciting laser radiation intensities of (*1*) 10, (*2*) 100 and (*3*) 1000 kW/cm^2, and the corresponding chemical potentials for electrons μ_C = –16 (*1*), –32 (*2*), and –50 meV (*3*). Dashed curves reproduce the experimental spectra from Fig. 1.

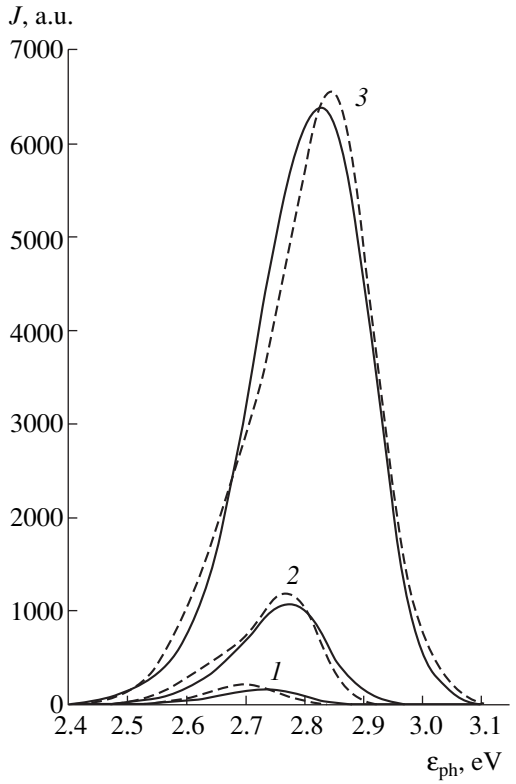

Fig. 3. Theoretical spectra (solid curves) fitted to the experimental spectra (dashed curves reproducing the PL spectra from Fig. 1) for exciting laser radiation intensities of (*1*) 10, (*2*) 100 and (*3*) 1000 kW/cm^2. The matching was provided by the Uhrbach parameter U = 48 meV, the quasi-temperature θ = 31 meV, and the chemical potentials for electrons μ_C = 163 (*1*), 75 (*2*), and 13 meV (*3*) and holes μ_V = –92 (*1*), –139 (*2*), and –181 meV (*3*).

indium that leads to the appearance of objects resembling quantum dots, featuring localized states with the DOS tails extending far into the bandgap.

This paper presents a semiempirical description of the spectrum of such localized energy levels whose DOS tail, characterized by the Uhrbach energy, influences the shape of the left-hand (long-wavelength) edge of the spectral band. This parameter can be adjusted by fitting the shape of a theoretical spectral band to the corresponding experimental curve. In the case under consideration, this parameter is about 50 meV. The right-hand (high-energy) wing of the spectral band might seem to be determined by the temperature-dependent smearing of the electron and hole state population functions. If this were the case, this smearing of the right-hand wing would be very small, namely, not exceeding 10 meV at liquid nitrogen temperature. However, an analysis of the experimental data shows that the right-hand wing smearing is significantly greater than the value corresponding to the lattice temperature and amounts to about 30 meV. In this context, it was of interest to consider the contour of the PL band for a quasi-bulk plate of singe crystal GaN [3]. The room-temperature PL measurements showed that the full width at half maximum (FWHM) of this band was approximately 80 meV, and about half of this value was due to the short-wavelength (high-energy) wing of the band. This is evidence that the conduction band edge of GaN is also smeared.

The theoretical spectra are most sensitive with respect to the bandgap width of a QW material, which was taken equal to 2.74 eV. In calculating the spectra in Fig. 2, we varied only the intensity of pumping and used the corresponding values of the Fermi quasi-level for electrons, while the Fermi quasi-level for holes was found from the condition of quasi-neutrality. Figure 3 shows theoretical spectra (solid curves) calculated using the corresponding fitting parameters and Fermi quasi-levels for pumping intensities of 10, 100, and 1000 kW/cm^2. For comparison, the dashed curves show the corresponding experimental PL spectra (reproducing the solid curves from Fig. 1). As can be seen, it is possible to reach a good agreement between theory and experiment.

Theory of spontaneous emission from the ideal QW. The theory of spontaneous recombination emis-

sion due to photogenerated carriers in the ideal semiconductor QW is constructed using the methods of quantum electrodynamics. This approach takes into account the Hamiltonian of the quantum electromagnetic field, the Hamiltonian of the electron and hole subsystems, and the Hamiltonian of the electron–hole interaction. In the linear (with respect to the field strength) approximation, this interaction is described by the term

$$\hat{V} = -\frac{e}{c}\mathbf{A}\hat{\mathbf{v}}, \quad (1)$$

where $\hat{\mathbf{v}}$ is the operator of electron velocity and $\mathbf{A}$ is the operator of vector potential of the quantum electromagnetic field (the term containing A^2 is rejected). The latter operator can be expressed as [4]

$$\mathbf{A}(\mathbf{r}, t) = \frac{c}{\sqrt{V}}\sum_{q,\alpha}\sqrt{\frac{2\pi\hbar}{\omega_q}}e^{-i\mathbf{q}\cdot\mathbf{r}}\mathbf{e}_{\alpha,q}[q_{q,\alpha}(t) + a^{+}_{-q,\alpha}(t)], \quad (2)$$

where V is the volume of the system featuring a photon with the frequency $\omega_q = cq$ and $a_{q\alpha}(t) = a_{q\alpha}e^{-i\omega_q t}$ is the operator of annihilation of the photon with wavevector q and polarization α.

Using Eqs. (1) and (2) and the Fermi golden rule, we can obtain an expression for the probability ΔW_{if} of photon emission per unit time with energy $\varepsilon = \hbar\omega_q$, with simultaneous transition of the atomic system from the initial (i) to the final (f) state. Then, we consider the spectrum of photons emitted with the given q, ω_q, escape directions within solid angle $\Delta\Omega$, and energies within interval $\Delta\varepsilon$. Now, let us pass from the photon emission probability ΔW_{if} per unit time to the spectral angular density $S(k)$ of photon emission defined as

$$S(k) = \frac{\Delta W_{if}}{\Delta\varepsilon\Delta\Omega}, \quad (3)$$

which corresponds to the probability of the transition of one electron with the given quasi-momentum k from the conduction (C) to the valence (V) band. The spectral density $I(\varepsilon)$ integrated over the momenta of all electrons is obtained by summing Eq. (3) with respect to k with allowance for the function of electron state population in the C and V bands:

$$I(\varepsilon) = \sum_k S(k) f_C(k)(1 - f_V(k)). \quad (4)$$

This value has a dimensionality of the product of inverse energy and frequency. Replacing the summation by integration, we obtain the integral spectral density

$$I(\varepsilon) = \frac{e^2}{\hbar c}\frac{A_0 m}{\hbar^3} f^{(e)} f^{(h)} \frac{\left|P_{CV}^{(x)}\right|^2}{m_0^2 c^2}\frac{\varepsilon}{(2\pi)^2}\Theta(\varepsilon - E_g), \quad (5)$$

where A_0 is the lattice unit cell area in the QW, m_0 is the free electron mass, m is the reduced effective mass of electrons and holes, and $P_{CV}^{(x)}$ is the matrix element of the x component of the operator of momentum. This matrix element includes the periodic amplitudes of the Bloch wave function with a QW unit cell period. The cell volume is $V_0 = A_0 d$, where d is the QW thickness. The total QW area A can be used for the passage from summation to integration over all values of the two-dimensional wavevector. This integral is taken with the aid of a delta function of energy and the isotropic quadratic dispersion law for the C and V bands:

$$E_C(k) = \frac{\hbar^2 k^2}{2m_C} + E_g, \quad E_V(k) = -\frac{\hbar^2 k^2}{2m_V}. \quad (6)$$

The energies $E_C(k)$ and $E_V(k)$ are measured relative to the top of the valence band, and the energy difference can be written as

$$E_C(k) - E_V(k) = \frac{\hbar^2 k^2}{2m} + E_g, \quad \frac{1}{m} = \frac{1}{m_C} + \frac{1}{m_V}, \quad (7)$$

where m_C and m_V are the effective masses of charge carriers.

The shape of the Pl line is determined by the factor

$$F(\varepsilon) = f^{(e)} f^{(h)} \varepsilon\Theta(\varepsilon - E_g), \quad (8)$$

where Θ is the unit step function, which appeared as a result of integration of the delta function with respect to the wavevector. The electron and hole state population functions $f^{(e)}$ and $f^{(h)}$ depend, in accordance with formulas (6), on the photon energy via the arguments

$$\varepsilon_C = (\varepsilon - E_g)\frac{m}{m_C}, \quad \varepsilon_V = (\varepsilon - E_g)\frac{m}{m_V}, \quad (9)$$

and they take the usual form

$$f^{(e)} = \frac{1}{e^{(\varepsilon_C - \mu_C)/\theta} + 1}, \quad f^{(h)} = \frac{1}{e^{(\varepsilon_V - \mu_V)/\theta} + 1}, \quad (10)$$

where μ_C and μ_V are the Fermi quasi-levels for electrons and holes, respectively, and θ is the temperature expressed in energy units (or the quasi-temperature

smearing). For a two-dimensional gas in the QW, the Fermi quasi-level for electrons (holes) can be analytically calculated as

$$\mu_C = \theta \ln(e^{\nu} - 1), \tag{11}$$

where $\nu = N/N_C$, $N_C = m_C\theta/(\pi\hbar^2)$, and N is the electron (hole) density (per unit area of the QW surface). Expression (8), determining the shape of the Pl line, contains a steplike function Θ, which is zero for photon energies below the bandgap width E_g and unity for energies above this value. The jumplike feature in the spectrum reflects the steplike change in the DOS for the QW, as reflected by the $\Theta(\varepsilon - E_g)$ term in the energy dependence of the DOS. As can be seen in Fig. 2, which shows the spectra calculated using formulas (8)–(11), the agreement between theory and experiment is poor: roughly speaking, the theory describes only half of the experimental spectral curve. The other half must appear due to a tail in the DOS.

Theory taking into account a tail in the DOS. In the case of crystalline solids with a sharp bandgap edge (i.e., with neglect of a tail in the DOS), the electron and hole energies (ε_C, ε_V) given by formulas (9) are positive quantities. In disordered structures, these energies may acquire negative values as well. This is also true for the localized energy levels in the bandgap. In this case, form function (8) of the spontaneous emission spectrum can be generalized and written as

$$F = G^{(e)}G^{(h)}\varepsilon, \tag{12}$$

where $G^{(e)}$ and $G^{(h)}$ are the electron and hole distribution functions, respectively, equal to the products of the corresponding DOS functions, $\rho^{(e)}$ or $\rho^{(h)}$, and the Fermi population functions, $f^{(e)}$ or $f^{(h)}$, given by formulas (10). For the ideal QW, the DOS is described by steplike functions $\rho^{(e)} = \Theta(\varepsilon_C)$ and $\rho^{(h)} = \Theta(\varepsilon_V)$, whose products with the population functions given by formulas (10) are described by the steplike function $\Theta(\varepsilon - E_g)$.

In the case of disordered systems, no exact theory capable of consistently describing the localized DOS has been developed [5], and we have to use a phenomenological expression. We adopt a priori the following expressions for the DOS:

$$\rho^{(e)} = \frac{1}{e^{-\varepsilon_C/U} + 1}, \quad \rho^{(h)} = \frac{1}{e^{-\varepsilon_V/U} + 1}, \tag{13}$$

where ε_C and ε_V are the electron and hole energies given by formulas (9) and U is the aforementioned characteristic Uhrbach energy considered here as the fitting parameter. The DOC functions (13) exhibit exponential decay in the bandgap and tend to unity in depth of the allowed energy bands. Accordingly, form function (12) describing the spectrum of recombination emission from the QW in the presence of DOS tails in the bandgap takes the following form:

$$F(\varepsilon) = \frac{\varepsilon}{e^{-\varepsilon_C/U} + 1}\frac{1}{e^{(\varepsilon_C - \mu_C)/\vartheta} + 1}\frac{1}{e^{(\varepsilon_V - \mu_V)/\vartheta} + 1}\frac{1}{e^{-\varepsilon_V/U} + 1}, \tag{14}$$

where $\varepsilon_C = (\varepsilon - E_g)m/m_C$, $\varepsilon_V = (\varepsilon - E_g)m/m_V$, and ε is the photon energy. Here, the ε_C and ε_V values are positive for photon energies greater than the bandgap width E_g and negative for energies below this value.

Now, let us determine the Fermi quasi-levels μ_C and μ_V for electrons and holes, respectively, entering into function (14). The general formula relating the Fermi quasi-level to the surface density N of the charge carriers in the presence of the DOS tail is

$$N = \frac{m_C}{\pi\hbar^2}\int_{-\infty}^{\infty}\rho(\varepsilon)f(\varepsilon)d\varepsilon, \tag{15}$$

where $\rho(\varepsilon)$ is the DOS given by formulas (13) and $f(\varepsilon)$ is the state population function given by expressions (10). The integral in relation (15) can be approximately calculated proceeding from the following considerations. The integrand exhibits a maximum at a certain value of the variable ε, which is given by the formula

$$\varepsilon_{max} = \mu\frac{u}{u + \theta}. \tag{16}$$

Then, the integrand can be considered as approximately equal to $\rho^{(e)}$ for $\varepsilon < \varepsilon_{max}$ and to $f(\varepsilon)$ for $\varepsilon > \varepsilon_{max}$. This yields an approximate expression

$$N = N_C\frac{u + \theta}{\theta}\ln\left(1 + \exp\left[\frac{\mu}{u + \theta}\right]\right), \tag{17}$$

which can be used both for electrons and holes (in which case N_C has to be replaced by N_V). For electrons, the chemical potential is a variable quantity selected so as to provide for the best agreement between theoretical and experimental spectra. Then, formula (17) can be used for determining the chemical potential of holes, which turns out to be negative in all cases. The shape of spontaneous emission spectrum (12) is determined primarily by the electron distribution function $G^{(e)}$. The position of the maximum in this spectrum is close to position (16) of the maximum of the integrand in Eq. (15), but the former peak is slightly shifted left under the influence of the hole distribution function $G^{(h)}$. This function remains virtually unchanged during variation of the electron (and, hence, the hole) potential. Thus, the growth of the spectral function and the shift of its maximum are entirely determined by

Table

μ_C, eV	μ_V, eV	N, cm^{-2}	ε_{max}, eV (theory)	ε_{max}^{ex}, eV (experiment)	$\Delta\varepsilon_{max}$, eV (theory)	$\Delta\varepsilon_{max}^{ex}$, eV (experiment)
0.163	–0.092	1.44×10^{13}	2.83	2.85	100	150
0.075	–0.139	0.84×10^{13}	2.78	2.77	50	70
0.013	–0.181	0.51×10^{13}	2.73	2.70	0	0

changes in the electron distribution function related to variation of the electron chemical potential. Comparative data on the chemical potentials for electrons and holes, the charge carrier densities in the conduction and valence bands, the positions of PL peaks, and the blue shifts are given in the table for E_g = 2.75 eV, U = 0.0484 eV, and θ = 0.0308 eV.

Finally, let us discuss the aforementioned condition of equality of the electron and hole densities. Since the QW material is pyroelectric [6], the condition of quasineutrality must, generally speaking, also include the pyroelectric charges whose real surface density may be on the order of 10^{-13} cm^{-2}. However, in the case of narrow QWs (with thicknesses not exceeding 40 Å), the surface density rapidly drops with the layer thickness to reach a level of 10^{10} cm^{-2}. Therefore, in the case of thin QWs, the pyroelectric charges can be ignored [6].

Acknowledgments. The authors are grateful to V.E. Bugrov for fruitful discussions.

REFERENCES

1. N. A. Shapiro, P. Perlin, C. Kisielowski, *et al.*, MRS Internet J. Nitride Semicond. Res. **5**, 1 (2000).
2. M. A. Jacobson, D. K. Nelson, N. Grandjean, *et al.*, Phys. Status Solidi C **1**, 487 (2002).
3. K. Motoki, T. Okahisa, N. Matsumoto, *et al.*, Jpn. J. Appl. Phys. **40**, L140 (2001).
4. A. S. Davydov, *Quantum Mechanics* (Nauka, Moscow, 1973; Pergamon, Oxford, 1976).
5. N. F. Mott and E. A. Davis, *Electronic Processes in Non-Crystalline Materials* (Clarendon Press, Oxford, 1971).
6. O. Ambacher, J. Majewski, C. Miskyv, *et al.*, J. Phys.: Condens. Matter **14**, 3399 (2002).

Translated by P. Pozdeev

Technical Physics Letters, Vol. 31, No. 7, 2005, pp. 578–580. Translated from Pis'ma v Zhurnal Tekhnicheskoĭ Fiziki, Vol. 31, No. 13, 2005, pp. 89–94.

Effect of Alternating-Sign Plastic Straining on the Shape Memory Effects in Nickel Titanium

S. P. Belyaev*, A. E. Volkov, M. E. Evard, and M. L. Leskina

St. Petersburg State University, St. Petersburg, 199164 Russia

** e-mail: spb@smel.math.spbu.ru*

Received March 10, 2005

Abstract—The effects of shape memory, martensite transformation plasticity, and two-way shape memory in nickel titanium (TiNi) prestrained in an alternating-sign regime have been studied. The reversible deformation and the temperature-dependent deformation kinetics in the temperature interval of martensite transformation were independent of the degree of prestraining. It is concluded that an increase in the density of dislocations does not significantly influence the mechanical behavior of nickel titanium in the vicinity of the martensite transformation. The results of computer simulation based on the structural analytical theory are in satisfactory agreement with experiment. © *2005 Pleiades Publishing, Inc.*

The effects of reversible inelastic deformation during the martensite transformation (MT) in nickel titanium (TiNi) are highly sensitive to thermomechanical prehistory of the material, in particular, to the magnitude and method of preliminary plastic straining [1–4]. The effect of plastic straining is related, first, to the development of internal stresses (which produce orienting action on the microscopic shear involved in the transformation) and, second, to an increase in the density of dislocations (leading to a growth of the effective "friction force" during the motion of phase boundaries and, hence, to a change in the temperature-dependent deformation kinetics). In the experiments involving plastic straining, an increase in the density of defects is usually accompanied by variations of the long-range fields of oriented stresses, so that both these factors jointly influence the mechanical behavior of alloys during the MT.

We believe that it is possible to decrease the role of oriented internal stresses by means of a preliminary plastic straining of a material in a symmetric cycle involving a change in the sign of stresses. Apparently, in the absence of a special direction of deformation, all of the observed phenomena will be related only to an increase in the density of dislocations. This will allow us to evaluate the role of this factor in the formation of mechanical properties of nickel titanium in the temperature interval of the MT.

This paper presents the results of investigations of the effect of preliminary alternating-sign plastic straining on the properties of nickel titanium.

The experiments were performed with an equiatomic TiNi alloy. The samples were prepared as described in [1–3]. Preliminary torsion straining was performed at $T = 600$ K, so that the stress-induced MT was impossible and only the dislocation channel of plasticity was activated. The alternating-sign torsion was carried out in one or several mechanical treatment cycles in a regime with fixed strain amplitude. The plastic strain per cycle was assumed to be equal to a double width of the mechanical hysteresis loop.

After setting a certain plastic strain level, the samples were loaded at a constant torque to a stress of $\tau = 20$ MPa and cooled so as to pass via the temperature interval of the MT. The observed accumulation of deformation in the course of the MT (MT plasticity) was measured. After cooling down to room temperature, the torque was removed and the sample was heated, which was accompanied by the recovery of deformation. When the deformation was completely recovered, the thermal cycle in the temperature interval of the MT was carried out and the two-way shape memory was determined. Then, the sample was again heated to 600 K and subjected to additional alternating-sign straining, after which the above procedures were repeated. As a result, the plastic strain γ_p of the sample was increased step by step, with intermediate measurements of the reversible deformation characteristics. The MT temperatures were determined from the deformation–temperature dependences obtained in the cycle of cooling under load and heating without load.

The results of our experiments presented in Fig. 1a show that, as the magnitude of the alternating-sign straining is increased, there is no significant tendency to increase or decrease in the forward or reverse MT temperatures. This behavior differs from that observed in the case of unidirectional straining [3, 4].

Figure 1b (open circles) presents data on the effect of alternating-sign plastic straining on the single and two-way shape memory effects. As can be seen, preliminary straining to a level above 70% does not affect the ability of nickel titanium to reversibly deform in the

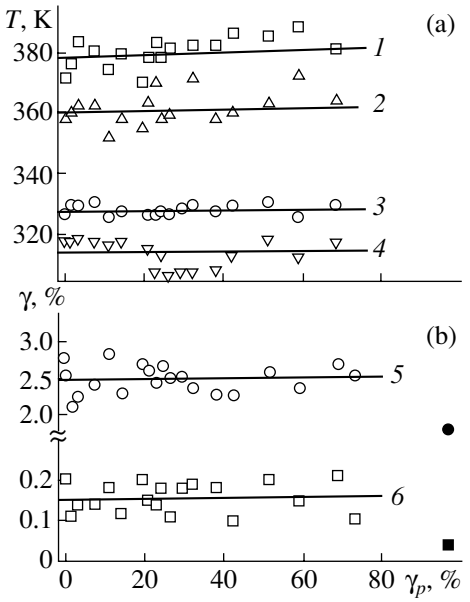

Fig. 1. Experimental dependences of the reverse MT (*1*) start and (*2*) finish temperatures, the forward MT, (*3*) start and (*4*) finish temperatures, the shape memory (*5*), and the two-way shape memory (*6*) versus preliminary plastic strain γ_p.

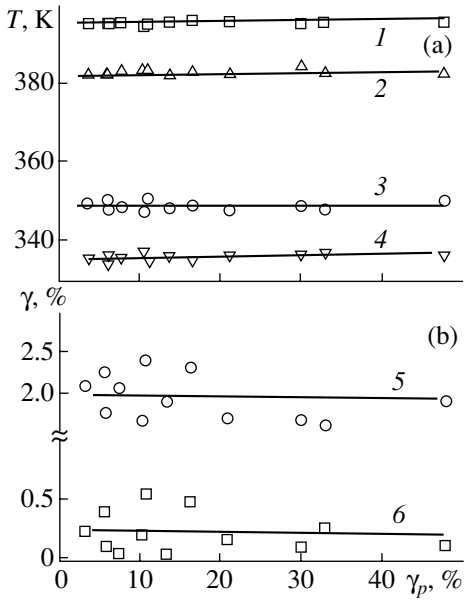

Fig. 2. Computer-simulated dependences of the reverse MT (*1*) start and (*2*) finish temperatures, the forward MT (*3*) start and (*4*) finish temperatures, the shape memory (*5*), and the two-way shape memory (*6*) versus preliminary plastic strain γ_p.

course of the MT. From this, we conclude that an increase in the density of defects without the formation of long-range oriented fields of internal stresses does not significantly influence the mechanical behavior of nickel titanium in the vicinity of the MT. This conclusion was confirmed by the results of an additional experiment, in which a sample after plastic prestraining to 73% was subjected to alternating-sign torsion in an asymmetric cycle (straining to 1.3% in one direction and to 2.6% in the opposite direction). The measurements performed after this treatment showed evidence of a significant change in the single and two-way shape memory (Fig. 1b, black symbols) in comparison to the case of symmetric straining. Evidently, the asymmetry in the straining cycle must be accompanied by the accumulation of oriented stresses, and these stresses account for the observed changes.

Thus, our experimental results indicate that the short-range interaction of phase boundaries and dislocations generated by the plastic straining does not play a significant role in the formation of shape memory in TiNi alloys.

We have also performed a computer simulation of the properties of a prestrained TiNi alloy using a structural analytical model [5] in a variant stipulating sequential averaging of microdeformations over the volume of a single grain in a polycrystalline sample and over the entire set of grains [6]. Plastic straining in the austenite state was simulated with allowance for possible slip along the {110} and {100} planes at various shear stresses, as described in [7, 8]. The level of internal stresses in each grain was assumed to be proportional to the stain mismatch between the grain and its environment [9]:

$$\rho_{kl} = C_p C_{klij}(\varepsilon_{ij}^0 - \varepsilon_{ij}),$$

where ρ_{kl} is the stress tensor in the grain, C_{klij} is the tensor of elastic moduli of the grain, ε_{ij}^0 is the average inelastic strain in the polycrystalline sample, ε_{ij} is the inelastic strain in the grain, and C_p is a constant coefficient. The constant parameters of the model were selected so as to insure that the theoretical cures describing the deformation accumulation and recovery in the course of thermal cycling of a nonprestrained sample would fit to the experimental data.

The results of computer simulation are presented in Fig. 2. A comparison of the calculated and experimental dependences shows their satisfactory agreement, so that the proposed theoretical model can be used for predicting the behavior of prestrained materials featuring the MT.

Acknowledgments. This study was supported in part by the Russian Foundation for Basic Research (project no. 04-01-00406), the INTAS Foundation (grant no. 03-5547), and the Presidential Program for Support of the Leading Scientific Schools in Russia (projects nos. NSh-2180.2003.1 and NSh-2288.2003.1).

REFERENCES

1. A. E. Volkov and I. V. Inochkina, in *Proceedings of the 35th Seminar on the Topical Problems of Strength, Pskov, 1999*, Chap. 2, pp. 619–623.
2. S. P. Belyaev, A. E. Volkov, and I. V. Inochkina, Vestn. Tambov. Univ. **5**, 293 (2000).
3. S. P. Belyaev, A. E. Volkov, I. V. Inochkina, *et al.*, in *Proceedings of the 35th International Seminar on the Topical Problems of Strength, Vitebsk, 2000*, pp. 689–693.
4. V. E. Gyunter, T. Yu. Maletkina, and A. A. Klopotov, Prikl. Mekh. Tekh. Fiz. **39**, 175 (1998).
5. V. A. Likhachev and V. G. Malinin, *Analytical Structural Theory of Strength of Materials* (Nauka, St. Petersburg, 1993) [in Russian].
6. M. E. Evard and A. E. Volkov, J. Eng. Mater. Technol. **121**, 102 (1999).
7. M. E. Evard and A. E. Volkov, in *Proceedings of the International Symposium on Shape Memory Alloys: Fundamentals, Modeling, and Industrial Applications, Montreal, 1999*, pp. 177–183.
8. A. E. Volkov and M. E. Evard, in *Proceedings of the 35th Seminar on the Topical Problems of Strength, Pskov, 1999*, Chap. 2, pp. 321–325.
9. A. E. Volkov and I. V. Inochkina, in *Nonlinear Problems of the Mechanics and Physics of Deformable Solids: A Collection of Works of the Novozhilov Scientific School* (St. Petersburg, 2000), Issue 3, pp. 220–225.

Translated by P. Pozdeev

Technical Physics Letters, Vol. 31, No. 7, 2005, pp. 581–583. Translated from Pis'ma v Zhurnal Tekhnicheskoĭ Fiziki, Vol. 31, No. 14, 2005, pp. 1–6.

Non-Alloy Cr/Au Ohmic Contacts in the Technology of Planar Beam-Lead GaAs *p–i–n* Diodes

S. E. Aleksandrov, V. V. Volkov, V. P. Ivanova, Yu. S. Kuz'michev, and Yu. V. Solov'ev

St. Petersburg State Technical University, St. Petersburg, Russia
"Svetlana–Elektronpribor" Corporation, St. Petersburg, Russia

Received January 20, 2005

Abstract—The characteristics of non-alloy Cr/Au ohmic contacts in planar beam-lead GaAs *p–i–n* diodes have been studied. The room-temperature reduced contact resistance in the structures studied was 2×10^{-6} Ω cm^2. The obtained parameters of *p–i–n* diodes allow these devices to be used as limiters in radar protection systems.

Introduction. GaAs-based limiter *p–i–n* diodes intended for microwave applications must obey increased requirements with respect to the main diode parameters such as the serial resistance and capacitance. The capacitance can be decreased by reducing the area of the active region in the diode mesa structure, but this leads to an additional increase in the serial resistance of the metal–semiconductor junction. In the epitaxial GaAs-based *p–i–n* diode structures, the ohmic contacts to the *p*-type epilayers are usually made of Zn/Au and AuBe–Au, which provide for a reduced contact resistance on a level of 10^{-5} Ω cm^2. Unfortunately, the insufficiently tight adhesion of these materials to the epilayer does not ensure the rigid attachment of beam leads in the existing *p–i–n* diode technology.

We have studied the possibility of using a non-alloy Cr/Au ohmic contact to the *p*-type GaAs epilayers. It was established that the application of such materials provides for a sufficiently low contact resistance (~2×10^{-6} Ω cm^2) and ensures good adhesion at the metal–semiconductor interface. The proposed contacts have been successfully implemented in the technology of planar GaAs-based *p–i–n* diodes with beam leads for microwave applications.

Experimental. As is known from published data [1–3], the simplest way to obtain an ohmic junction is to bring a metal layer into contact with a strongly doped semiconductor region. We have studied the electrical characteristics of non-alloy Cr/Au ohmic contacts to strongly doped *p*-type GaAs epilayers. The experiments were performed on test heterostructures grown by metalorganic chemical vapor deposition (MOCVD) on semiinsulating GaAs substrates (commercial AGChP-8 grade). The epilayers had the following parameters (thickness and dopant concentration): p^+ layer, $h_p = 0.3$ μm, $N_{p^+} = (1–2) \times 10^{19}$ cm^{-3}; base $n(i)$ layer, $h_{n(i)} = 1$ μm, $N_{n(i)} = 1 \times 10^{14}$ cm^{-3}.

The technology of metal–semiconductor test structures (adapted to the entire diode fabrication) included the formation of ohmic contacts (Cr, $h = 0.1$ μm) by magnetron sputtering, vacuum thermal deposition of metallization (Au, $h = 0.2$ μm), and explosive photolithography. The mesa structure was obtained by etching in a peroxide–ammonia mixture (H_2O_2–NH_4OH–H_2O, 1 : 1 : 20)

Structure and electrical characteristics of non-alloy Cr/Au ohmic contacts to p^+-GaAs epilayer in *p–i–n* diodes

Upper semiconductor layer (h, N_p)	Metallization (h_{Cr}/h_{Au})	Annealing regime	Reduced contact resistance ρ_c, Ω cm^2
p^+-GaAs (0.3 μm, 1×10^{19} cm^{-3})	Cr/Au (0.1/0.2 μm)	–	$(6–7) \times 10^{-6}$
p^+-GaAs (0.3 μm, 1×10^{19} cm^{-3})	Cr/Au (0.1/0.2 μm)	420°C, 30 min (H_2 atmosphere)	$(3–5) \times 10^{-6}$
p^+-GaAs (0.3 μm, 2×10^{19} cm^{-3})	Cr/Au (0.1/0.2 μm)	–	$(4–5) \times 10^{-6}$
p^+-GaAs (0.3 μm, 2×10^{19} cm^{-3})	Cr/Au (0.1/0.2 μm)	420°C, 30 min (H_2 atmosphere)	$(2–4) \times 10^{-6}$

1063-7850/05/3107-0581$26.00

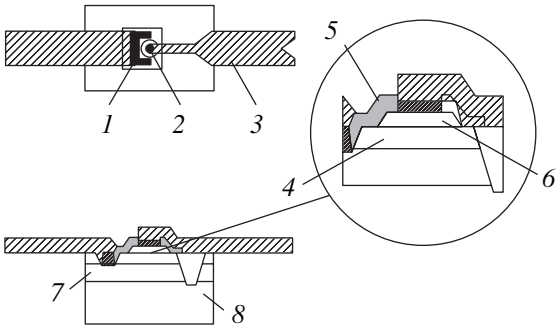

Fig. 1. Schematic diagram of a planar beam-lead GaAs *p–i–n* diode: (*1*) ohmic contact to n^+-GaAs epilayer; (*2*) ohmic contact to p^+-GaAs epilayer; (*3*) beam lead; (*4*) *n*(*i*)-GaAs epilayer; (*5*) SiO_2 insulator; (*6*) p^+-GaAs epilayer; (*7*) n^+-GaAs epilayer; (*8*) semiinsulating GaAs substrate.

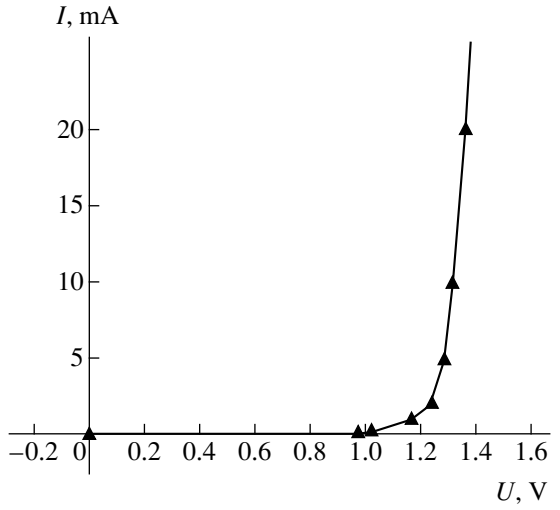

Fig. 2. The typical *I–U* curve of a planar beam-lead GaAs *p–i–n* diode with the following parameters: base *n*(*i*)-GaAs epilayer thickness, 1 μm; R_d = 4–5 Ω (I_{dir} = 10 mA); U_{dis} = 33 V (I_{inv} = 0.01 mA); C_0 = 0.015–0.017 pF.

down to the semiinsulating substrate. The etching process was controlled by measuring the breakdown voltage between probes on the epilayer surface. The electrical characteristics of the obtained ohmic contacts to the p^+ epilayers were determined using the long line technique [4].

Results and discussion. The electrical characteristics of the ohmic contacts to p^+-GaAs epilayers are presented in the table. The current–voltage (*I–U*) curves had a linear shape even without fusion. In order to prevent the diffusion of chromium into gold, which takes place at temperatures above 300°C, the stage of Cr/Au metallization was followed by the galvanic deposition of a 4-μm thick Au layer. The diffusion of chromium into *p*-type GaAs epilayer under the conditions studied (annealing temperature and duration) is insignificant [5]. The annealing for 30 min at T = 420°C in hydrogen led to a decrease in the reduced contact resistance, while a good adhesion of the ohmic contact to the epilayer was retained at a level ensuring the rigid attachment of the beam leads to the diode structure.

As can be seen from data in the table, the reduced contact resistance of the obtained non-alloy Cr/Au ohmic contacts ($\rho_c^{Cr/Au} = (2–4) \times 10^{-6}$ Ω cm^2) is comparable with the values reported for AuBe alloy contacts ($\rho_c^{Au/Be} = (2–5) \times 10^{-6}$ Ω cm^2). However, the proposed Cr/Au contacts provide for a more reliable adhesion at the metal–semiconductor interface, thus ensuring the rigid attachment of beam leads in the technology of GaAs *p–i–n* diodes.

The proposed non-alloy Cr/Au ohmic contacts were implemented in planar beam-lead GaAs *p–i–n* diodes, which were capable of operating in the microwave frequency range. We have developed a new planar design with "air bridges" (Fig. 1), which made it possible to obtain devices with a small size of the active region. This choice of the diode design was justified by two main factors. First, the use of beam leads provides for the simplicity of the device assembly in a slot-waveguide line of a microwave tract. Second, the presence of air bridges decreases the parasitic specific capacitance of the beam-lead metallization and, hence, the total serial capacitance of the device [9].

The working epitaxial diode structures grown by MOCVD on GaAs substrates (AGChP-8 grade) comprised a buried n^+ layer (h = 5 μm), doped with Si to 5×10^{18} cm^{-3}, a base *n*(*i*) layer (h = 1 μm), and a p^+ layer (0.3 μm) doped with Be to $(1–2) \times 10^{19}$ cm^{-3}. The mesa structure was formed using photolithography and liquid-phase etching. The *p–n* junction was passivated by silicon dioxide. Then, an AuGe–Ni-Au alloy ohmic contact was formed on the n^+ epilayer and a non-alloy Cr/Au contact, on the p^+ epilayer. Finally, the air bridges were formed and the chips were separated. Figure 2 shows the typical *I–U* curve of the planar *p–i–n* diode with the proposed ohmic contact. The main parameters of the ohmic contacts were as follows: serial resistance, R = 4–5 Ω (I = 10 mA); zero-bias capacitance, $C^{(0)}$ = 0.015–0.017 pF.

The obtained beam-lead GaAs *p–i–n* diodes were successfully tested as protective limiters in high-power microwave systems. In the millimeter wavelength range (λ = 3–8 mm), these devices ensured reliable operation at a power of up to 100 W, while the transmission losses did not exceed 1 dB and the damping introduced in the limitation regime was 12 dB.

Conclusions. Using non-alloy Cr/Au ohmic contacts, it is possible to provide for a reduced contact resistance as low as $\rho_c = 2 \times 10^{-6}$ Ω cm^2. Implementation of the proposed ohmic contact in the technology of beam-lead GaAs *p–i–n* diodes ensures a high useful yield with respect to electrical parameters and provides

for a reliable adhesion of the ohmic contact to the GaAs epilayer, which is necessary for the rigid attachment of the beam leads to the diode structure. The developed planar GaAs *p–i–n* diodes meet all requirements for the elements of protective semiconductor devices for microwave systems, such as radars operating in the millimeter wavelength range.

REFERENCES

1. S. Hatatani, L.-Q. Guo, J.-H. Oh, *et al.*, J. Cryst. Growth **170**, 297 (1997).
2. F. Dimroth, U. Schubert, F. Schienle, and A. W. Bett, J. Electron. Mater. **29**, 47 (2000).
3. C. H. Chen, M. Hargis, J. M. Woodall, and M. R. Melloch, Appl. Phys. Lett. **74**, 3140 (1999).
4. M. Shur, *GaAs Devices and Circuits* (Plenum, New York, 1987).
5. S. S. Khludkov, O. B. Koretskaya, and A. V. Tyazhev, Fiz. Tekh. Poluprovodn. (St. Petersburg) **38**, 274 (2004) [Semiconductors **38**, 262 (2004)].
6. T. Sanada and O. Wada, Jpn. J. Appl. Phys. **19**, 491 (1980).
7. A. Piotrowska, A. Guivarch, and G. Pelous, Solid-State Electron. **26**, 179 (1983).
8. S. V. Evstigneev and D. S. Shipitsin, Fiz. Obrazov. Vyssh. Uchebn. Zaved. **5** (1), 85 (1999).
9. V. V. Chikun, Élektron. Tekh., Ser. Élektron. SVCh, No. 8, 13 (1991).

Translated by P. Pozdeev

Technical Physics Letters, Vol. 31, No. 7, 2005, pp. 584–587. Translated from Pis'ma v Zhurnal Tekhnicheskoĭ Fiziki, Vol. 31, No. 14, 2005, pp. 7–15.

Microwave Oscillations in the Acceleration Channel of SPD-ATON Stationary Plasma Thruster

K. P. Kirdyashev, A. I. Bugrova, A. I. Morozov, A. V. Desyatskov, R. K. Kirdyashev, and V. K. Kharchevnikov

Fryazino Branch, Institute of Radio Engineering and Electronics, Russian Academy of Sciences, Fryazino, Moscow oblast, Russia

Moscow Institute of Radio Engineering, Electronics, and Automatics (Technical University), Moscow, Russia

Nuclear Fusion Institute, Russian Research Center Kurchatov Institute, Moscow, Russia

Received March 1, 2005

Abstract—The parameters of microwave plasma oscillations in the acceleration channel of an SPD-ATON stationary plasma thruster have been measured. There is a stable correlation between the microwave intensity, on the one hand, and the magnetic field configuration in the region of plasma acceleration and the formation of plasma flow detached from the channel wall, on the other hand. The experimental data agree with the notion about the contribution of the electron scattering on microwave oscillations to the anomalous transverse conductivity of plasma in the acceleration channel. © *2005 Pleiades Publishing, Inc.*

As is known, the acceleration of plasma in a stationary plasma thruster (SPT) is accompanied by the generation of microwave oscillations, which is related to the instability of the electron component of plasma in the acceleration channel and in the output plasma flow [1]. The nonequilibrium character of the electron velocity distribution function is determined by the influence of the electric field, the ionization of a working medium in the course of plasma acceleration, and the interaction of the plasma flow with dielectric walls in the acceleration channel of the SPT. The main factors of this plasma–wall interaction are the scattering of the electron drift flows, the anomalous erosion, and the secondary electron emission from the channel wall. The microwave oscillations generated in the course of the plasma instability development may provide conditions for the turbulent mixing of various groups of electrons in the plasma acceleration region and for the anomalous electron mobility across the external magnetic field.

In SPTs of the traditional design, the interaction of the plasma flow with dielectric walls in the acceleration channel is an important factor: the scattering of electrons on the walls provides for the anomalous transverse conductivity of plasma in the acceleration region and for the discharge current formation. A mechanism of the near-wall plasma conductivity was justified and experimentally studied in [2]. SPTs of the second generation are characterized by special conditions for the realization of the anomalous transverse plasma conductivity in the acceleration channels, where the magnetic field configuration [3] is such that plasma flows detached from the walls are formed with a small divergence angle and the limiting parameters ensuring the maximum SPT efficiency.

It is natural to suggest that, under such conditions, the scattering of electrons on microwave oscillations excited in the acceleration channel is among the factors responsible for the anomalous transverse conductivity of plasma in the channel. In order to check for the possibility that this mechanism is operative, we have experimentally studied the microwave oscillations excited in the acceleration channel for various magnetic field configurations in the region of plasma acceleration. The influence of this magnetic field on the plasma acceleration regime consists in the formation of plasma flows differently interacting with the acceleration channel walls.

The experiments were performed on a prototype SPT setup of the SPD-ATON type with an external channel diameter of 60 mm, which was previously described in [4]. The working substance was xenon, which was supplied via a gas distribution system at a mass flow rate of 2 mg/s in a buffer region and 0.4 mg/s in a cathode compensator cavity. The magnetic field configuration in the channel and the shape of the output plasma flow could be modified by changing currents in coils of the magnetic system. When the magnetic field lines were oriented in the radial direction at the acceleration channel edge, the field produced a focusing effect and a plasma flow detached from the channel acquired a nearly cylindrical shape. In the regimes with magnetic field lines sloped relative to the channel axis, the output plasma flow had a cone shape with a relatively large angle of divergence; in such regimes, the engine thrust exhibited a significant decrease.

We have studied the SPT regimes with various magnetic field configurations and a discharge current in the channel maintained constant (about 2.05 A) at a nomi-

1063-7850/05/3107-0584$26.00 © 2005 Pleiades Publishing, Inc.

nal voltage of 300 V. It should be noted that the indicated discharge current in our setup (as well as in all plasma systems of the SPT type) significantly exceeds the values calculated proceeding from the pair electron collisions in the acceleration region.

The fields of plasma microwaves were measured using inductively coupled double-lead microwave probes. One probe was introduced into the acceleration channel via a gap in the dielectric wall and positioned at a distance of 20 mm from the anode. Another probe was introduced into the output plasma flow and could be moved in the axial and radial directions. The use of microwave probes occurring at a floating potential ensured the necessary dc decoupling in the regions of discharge plasma with distributed electric field. As a rule, the microwave probes are employed for measuring the relative characteristics and monitoring the microwave field distribution in the volume of plasma. The difficulties encountered in the measurements of absolute intensities and spectral characteristics of microwave oscillations are related to the uncertainty of the microwave probes coupling to the plasma wave field, the influence of plasma on the receiving properties of the probe, and the resonance properties of the measuring circuit. In this context, we have performed calibration experiments in the frequency range studied and measured the intensity of thermal plasma oscillations in a standard gas-discharge noise generator using a method described in [5].

The spectral range of plasma microwave fields in the acceleration channel was covered by measuring devices with the frequency tunable within 1.05–2.15, 1.95–4.0, and 3.85–7.15 GHz. The spectrum of microwave oscillations in a stationary regime was recorded using the method of sequential measurements in the three channels, with matching of the results obtained in the overlapping frequency intervals. The sequential spectra were measured by varying the frequency of measuring devices at a rate of 10–15 MHz/s, which ensured the monitoring of spectral components within a frequency band of 1–10 MHz. Features of the envelope of microwave oscillations in the acceleration channel and the output plasma flow were measured with variable time resolution. For the spectral measurements and the analysis of field distributions near the channel wall, the time resolution was 0.1–1.0 s. In the regime of measurements at particular frequencies, which were used for the evaluation of frequency and spatial correlations in the spikes of nonstationary microwave oscillation components, the resolution was improved to 100–200 μs.

In order to establish relationships between the results of local microwave measurements and the parameters of a plasma flow in the acceleration channel, we used the radial distributions of the electron density n_e, the electron temperature T_e, and the plasma potential ΔU_r obtained previously [4] with the aid of movable Langmuir probes. Using these correlations, we have estimated the thermal level of microwave oscillations at various frequencies and separated the frequency intervals corresponding to the excitation of oscillations as a result of the development of instability of the electron component of plasma flow in the channel.

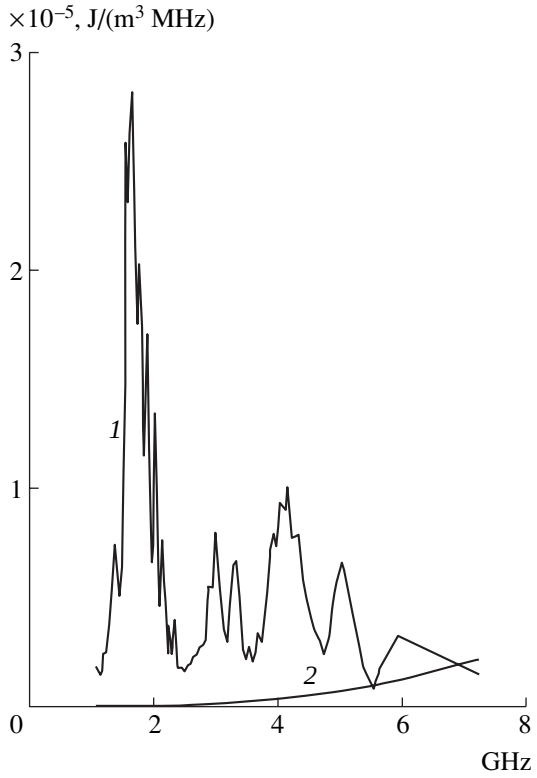

Fig. 1. The experimental spectrum of plasma microwave oscillations (curve *1*) in a near-wall region of the accelerating channel of SPD-ATON in comparison to the thermal noise level (curve *2*). The measurements were performed in a focusing magnetic field using a microwave probe spaced by 1 mm from the dielectric channel wall.

The results of our measurements showed that microwave oscillations with frequencies up to 6.5 GHz were excited in the plasma acceleration channel. The intensity of these oscillations in some frequency regions was 2–3 orders of magnitude higher than the thermal level (Fig. 1). The main maximum of the microwave spectrum is observed at 1–2.5 GHz, which corresponds to ω_{Pe} in the peripheral region of the plasma flow (ω_{Pe} is the Langmuir frequency of electrons). As can be seen in Fig. 1, the wide-band spectra of plasma oscillations are rather involved and exhibit quasi-monochromatic components. This spectral structure is reproduced in repeated measurements under fixed discharge conditions, which allows the formation of these microwave spectra to be related to processes in the acceleration channel of the SPT. The frequency separation of the quasi-monochromatic components observed in the region of 1–2 GHz was 400–450 MHz, which corresponds to the cyclotron frequencies of electrons in the region of the acceleration channel for a magnetic induction of 0.014–0.016 T. The observed variations in the

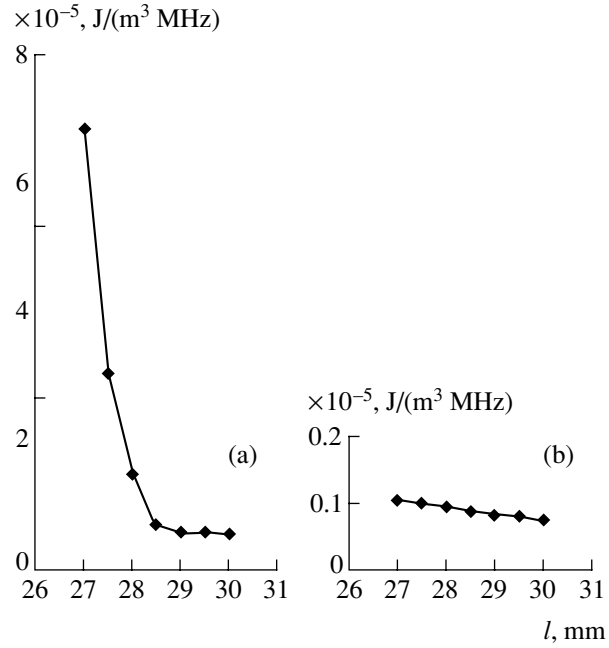

Fig. 2. Radial distributions of the intensity of microwave oscillations near the acceleration channel wall (outer channel radius, 30 mm) for the magnetic field of (a) focusing and (b) traditional configuration.

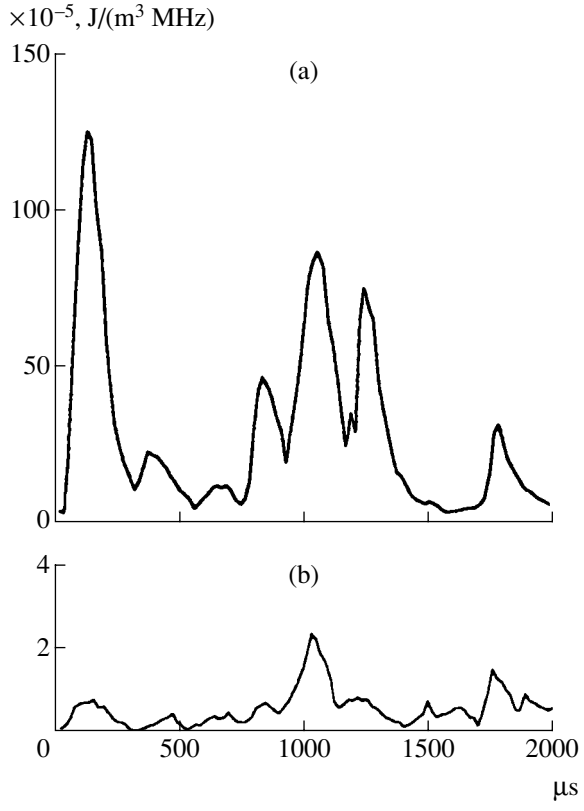

Fig. 3. Oscillograms of the envelopes of microwave oscillations (a) near the acceleration channel wall and (b) in the output plasma flow measured using microwave probes situated at a distance of 29 mm from the channel axis.

microwave spectrum (against the background of a general decrease in the intensity) are related to several factors, including (i) the presence of discrete components at the harmonics of the electron cyclotron frequency, (ii) incomplete matching between the microwave probes and plasma in the channel, and (iii) possible errors of the method of calibration with respect to the standard source of plasma microwave oscillations.

Differences in the regimes of plasma flow formation depending on the magnetic field configuration in the acceleration region are manifested in the microwave field distribution in the channel cross section (Fig. 2). The plasma flow detached from the channel walls exhibits a sharp increase in the intensity of oscillations when the probe is moved toward the center of the circular channel. In contrast, a rather insignificant radial variation of the intensity is observed under the conditions corresponding to the formation of a cone-shaped plasma flow interacting with the channel walls. On the passage to the regime of detached plasma flow formation, the intensity of oscillations exhibits a characteristic jump and increases by a factor of 25–50 as compared to that in the SPT regime with a traditional configuration of the magnetic field.

In determining the microwave field intensity in the plasma acceleration channel, it is necessary to take into account the nonstationary character of the envelope of microwave oscillations (Fig. 3), which exhibits a significant (up to 20 dB) decrease in the spike intensity in the output plasma flow. The envelope exhibits a random character (the coefficient of correlation between the intensity of spikes in the channel and in the output plasma flow does not exceed 0.5). In view of this pulsed character of the envelope, it is necessary to take into account the smoothening effect of the equipment on the results of measurements presented in Figs. 1 and 2. With allowance for this effect, the energy density of the nonstationary component of oscillations in the 1–3 GHz frequency range reaches 10^{-3}–10^{-2} J/(m^3 MHz). This value is 4–5 orders of magnitude higher than the thermal level of electric field oscillations in the plasma.

The results of our experiments lead to two conclusions that are important for understanding the character of processes in the acceleration channel of SPD-ATON thruster. According to the first conclusion, plasma in the acceleration channel occurs in a substantially nonequilibrium state and is characterized by the development of beam instability related to the acceleration of electrons in the peripheral region of the plasma flow. The possible instability of plasma in a radial electric field was also indicated by the results of potential measurements in the channel [4], according to which the formation of a plasma flow detached from the walls leads to a potential drop by 35–40 V over a distance of 0.2–0.3 mm. The radial component of the electric field near the wall reaches 10^2–10^3 V/cm, which is significantly higher than the critical field $E_D \approx 4\pi e^4/(n_e/T_e)$ corresponding to the acceleration of electrons in peripheral regions of the

plasma flow [6]. The formation of radial electron beams must give rise to the Langmuir oscillations of electrons in the channel, which is confirmed by the results of our spectral measurements (Fig. 1).

The second conclusion is related to the evaluation of the contribution of the electron scattering on microwave oscillations excited in the acceleration channel to the anomalous transverse conductivity of plasma in the channel. The possibility of the appearance of this contribution is related to the fact that the maximum excitation of microwave oscillations is observed for the magnetic field configuration leading to the formation of a plasma flow detached from the channel walls. The necessary estimates of the efficiency of a turbulent mechanism involved in the electron scattering in the channel and the formation of the anomalous transverse conductivity in the plasma flow can be obtained using a model of the accelerating Hall's plasma layer [7]. According to this model, the effective frequency of electron scattering on microwave oscillations can be expressed as

$$\nu_{ef} = (2W_{Pe}/n_e\varepsilon_{er})^{1/2}\omega_{Pe}, \quad (1)$$

where W_{Pe} is the energy density of the Langmuir electron oscillations, and $\varepsilon_{er} = e\Delta U_r$ is the energy of fast electrons (determined from the plasma potential jump near the channel wall). Using the results of the microwave intensity measurements, the energy density of electron oscillations was evaluated as $W_{Pe} = 3 \times 10^{-3}$–$10^{-2}$ J/m^3 in a frequency band of $\Delta f = 1$ GHz. The effective frequency of electron scattering on microwave oscillations according to formula (1) amounts to (1–2) $\times$ 10^9 s^{-1}. The discharge current j_D formed in the plasma acceleration region is determined by the transverse electron mobility $b_{e\perp}$ in the channel [8]:

$$\begin{aligned} j_D &= en_e b_{e\perp} E_z S_C, \\ b_{e\perp} &= (e/m_e)\nu_{ef}/(\omega_{Be}^2 + \nu_{ef}^2), \end{aligned} \quad (2)$$

where E_z is the longitudinal electric field component in the acceleration region, ω_{Be} is the cyclotron frequency of electrons, and S_C is the transverse cross section of the current-carrying region of the channel. According to relations (2), the transverse conductivity of plasma in the experimental regimes of SPD-ATON with a discharge current of $j_D = 2.05$ A is provided at $\nu_{ef} = (1–5) \times 10^{-8}$ s^{-1} for the frequency of electron pair collisions within 10^5–10^6 s^{-1}. Thus, the obtained experimental results showed that the formation of plasma flows detached from the SPT channel walls and the appearance of anomalous transverse conductivity in the plasma are related to the excitation of microwave oscillations in the acceleration channel.

REFERENCES

1. K. P. Kirdyashev and A. I. Morozov, Fiz. Plazmy **25**, 326 (1999) [Plasma Phys. Rep. **25**, 293 (1999)].
2. A. I. Bugrova, A. I. Morozov, and V. K. Kharchevnikov, Fiz. Plazmy **16**, 1469 (1990) [Sov. J. Plasma Phys. **16**, 849 (1990)].
3. A. I. Morozov, A. I. Bugrova, A. V. Desyatskov, *et al.*, Fiz. Plazmy **23**, 635 (1997) [Plasma Phys. Rep. **23**, 587 (1997)].
4. A. I. Bugrova, A. V. Desyatskov, V. K. Kharchevnikov, *et al.*, in *Proceedings of the 3rd International Conference on Spacecraft Propulsion, Cannes, 2000*, pp. 881–884.
5. K. P. Kirdyashev, *Microwave Processes in Plasma-Dynamic Systems* (Énergoatomizdat, Moscow, 1982), p. 142 [in Russian].
6. H. Driecer, Phys. Rev. **117**, 329 (1960).
7. V. I. Aref'ev and K. P. Kirdyashev, Zh. Tekh. Fiz. **45**, 527 (1975) [Sov. Phys. Tech. Phys. **20**, 330 (1975)].
8. *Physics and Application of Plasma Accelerators*, Ed. by A. I. Morozov (Nauka i Tekhnika, Minsk, 1974) [in Russian].

Translated by P. Pozdeev

Technical Physics Letters, Vol. 31, No. 7, 2005, pp. 588–590. Translated from Pis'ma v Zhurnal Tekhnicheskoĭ Fiziki, Vol. 31, No. 14, 2005, pp. 16–21.

Ion Focusing and Declusterization in Alternating Quadrupole Electric Field

V. V. Pervukhin

Nikolaev Institute of Inorganic Chemistry, Siberian Division, Russian Academy of Sciences, Novosibirsk, Russia

e-mail: pervv@che.nsk.su

Received February 21, 2005

Abstract—A new method of ion focusing at elevated pressures in an alternating quadrupole electric field is described and characterized. Using the proposed technique, it is possible to increase the sensitivity of mass-spectrometric techniques employing ionization at elevated pressures (such as ionization by glow discharge or chemical ionization at atmospheric pressure), with the simultaneous elimination of cluster ions. © *2005 Pleiades Publishing, Inc.*

In using mass-spectrometric techniques employing ionization at elevated pressures (such as ionization by glow discharge or chemical ionization at atmospheric pressure), it is important to provide the focusing of ions so as to deliver them without losses to the region of analysis. For the study of nucleation processes, we have developed a new method for gas phase ionization using a limited-current discharge [1]. This discharge is created inside the sample introduction chamber by means of a usual crown discharge initiated in air between a point electrode and the injection tube (acting as the floating electrode). This process is essentially a kind of the ionization by glow discharge, and it is much like the chemical ionization at atmospheric pressure in being sensitive to impurities possessing a high proton affinity.

This study was aimed at assessing the possibility of ion focusing in a quadrupole electric field in rough vacuum under conditions of limited-current discharge ionization. In mass spectrometers of the ion trap type, the pressure is intentionally increased so as to collect ions at the center [2].

Use of the limited-current discharge ionization encounters some difficulties. One problem is related to the unavoidable formation of cluster ions, which significantly interfere in the analysis. In this context, it was of interest to study the possibility that heating in an alternating electric field would produce the declusterization of ions.

Limited-current discharge source. Figure 1 shows a schematic diagram of the proposed system of gas introduction and ionization. This system employs a three-stage scheme of differential pumping. A sample is introduced in the first stage via stainless steel tube *1* with a cone-shaped nozzle with a 0.5-mm-diam hole. This region is evacuated by a mechanical pump operating at 5 l/s, which provides for a pressure of 6 Torr at the first stage of differential pumping.

In this chamber, the gas is ionized by limited-current discharge, which is created by a usual crown discharge initiated in air between point *2* and the sample injection tube *1* (acting as the floating electrode). As a result, electric discharge is also initiated between the nozzle edge and the counter electrode *3*, with the current limited by the crown discharge current. The current was measured with a microampermeter in the counter electrode circuit.

Quadrupole lens. Ions created in the first stage are supplied (via a 3-mm-diam hole in the counter electrode) into quadrupole lens *4* comprising four 120-mm-long stainless steel rods with a diameter of 10 mm, to which a sinusoidal voltage is applied with a frequency of 10–100 kHz and an amplitude of 0–500 V. The rods (connected in pairs as depicted in Figs. 1a and 1b) are arranged so that their centers form a square with a side length of 11.5 mm.

Figure 1 also shows the results of our computer simulation of the ion focusing under the action of a quadru-

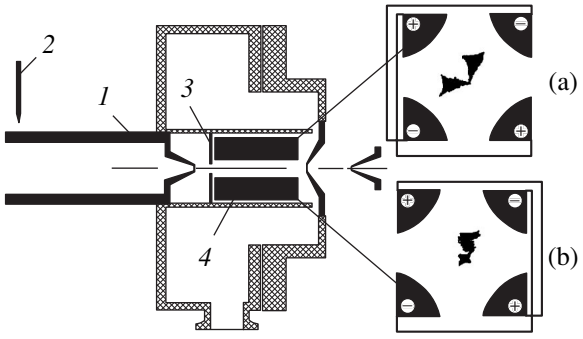

Fig. 1. Schematic diagram of the experimental installation and the results of computer simulations of the ion trajectories showing the ion focusing under the action of an alternating quadrupole electric field (see the text for explanations).

1063-7850/05/3107-0588$26.00 © 2005 Pleiades Publishing, Inc.

pole electric field. The simulations were performed using a SIMION 3D (Ver. 6.0) program package [3], which calculated the ion trajectories in the electric and magnetic fields generated between arbitrarily arranged electrodes.

We have used two models in order to take into account the elevated pressures in the ionization region. The first of these was the linear retardation (drag) model, in which the motion of ions was described by the following equation:

$$\frac{e\mathbf{E}}{m} = \frac{d^2}{dt^2}\mathbf{r} - D\frac{d}{dt}\mathbf{r}, \quad (1)$$

where e is the ion charge, m is the ion mass, $\mathbf{r}$ is the radius vector, D is the linear retardation coefficient, and $\mathbf{E}$ is the time-dependent electric field strength.

The second model treated ion interactions as the elastic collisions with immobile balls and described the collision probability as proportional to $\exp(-Vt/\lambda)$, where V is the ion velocity and λ is the ion mean free path between collisions. According to this model, the angle of divergence upon collision depends on the impact parameter. This parameter was determined with the aid of a random number generator, and the divergence angle was proportional to the interaction cross section with a given impact parameter.

Figures 1a and 1b show the typical ion trajectories simulated using to the first and second model, respectively. The model parameters were selected so as to correspond to a pressure of about 1 Torr, a molecular mass of the background gas equal to 28 amu, and an ion mass of 100 amu. The ion mean free path was taken equal to 3×10^{-3} cm [4], and the linear retardation was calculated by comparing formula (1) to an expression for the ion drift in an electric field, $\mathbf{V} = (b_0/P)\mathbf{E}$, where P is the background gas pressure and $b_0 \sim 2 \times 10^3$ (cm^2 Torr)/(V s) [5]. As can be seen, the application of a quadrupole electric field drives ions toward the center of the quadrupole lens, thus providing their focusing. Both models give generally identical results, but the ion trajectories in the linear retardation model virtually converge to a point, while the model of elastic collisions with immobile balls yields a certain finite region to which the ions are focused. Apparently, the former model is rough and the latter case is more realistic.

It should be noted that both models used in the trajectory simulation showed that the focusing is highly sensitive to the background gas pressure and the electric field parameters (amplitude and frequency). Indeed, in the case of a large coefficient of linear retardation or a small ion mean free path (which corresponds to high pressures), the ion diffusion toward the center becomes very slow and the focusing is virtually absent. In contrast, in the case of parameters corresponding to low pressures, the amplitude of ion oscillations becomes very large and the particles are lost on

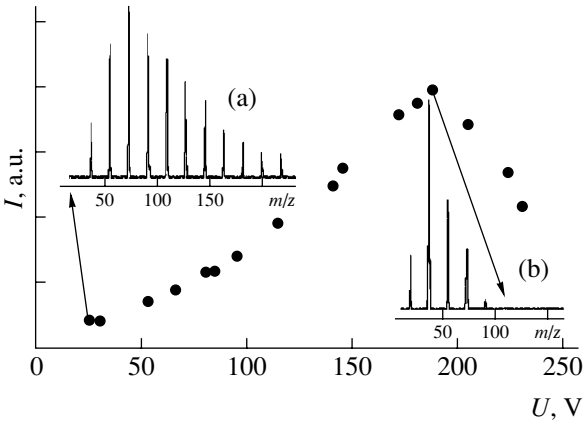

Fig. 2. A plot of the total ion current I versus amplitude U of the alternating voltage applied to electrodes of the quadrupole lens. The insets show the mass spectra obtained at the indicated points, corresponding to (a) low and (b) high applied voltages.

electrodes. Analogous effects are observed upon variation of the electric field amplitude and frequency.

For the experimental investigation of ion focusing in an alternating quadrupole electric field, the ions passing through the quadrupole lens are extracted via a 0.6-mm-diam nozzle to the second stage of differential pumping (0.6 Torr) and supplied to a mass analyzer. The conditions of mass spectrometry were described in detail elsewhere [6].

Figure 2 shows the results of these experiments. As can be seen, an increase in the amplitude of the alternating electric field with a frequency of 100 kHz is initially accompanied by the monotonic growth of the total ion current. This growth is observed up to a voltage of 180 V, after which the total current begins to decrease (in accordance with the results of calculations). It should be noted that, for the background pressures (~6 Torr) used in this study, the voltage amplitude could not be increased above 250 V because of the gas discharge between electrodes.

Another phenomenon accompanying the ion focusing in the alternating quadrupole electric field is the declusterization of ions. Indeed, the field accelerates ions relative to the neutral molecules. As a result, the energy of ions colliding with the neutral molecules increases, which leads to a growth in the ion temperature. Since most ions at elevated pressures exist in the form of clusters (in the case of air, these are water clusters), an increase in the internal temperature leads to evaporation of the cluster shell.

The insets in Fig. 2 show the mass spectra of the laboratory air measured at (a) 25 V and (b) 180 V amplitude of the ac voltage applied to the electrodes of the quadrupole lens. In both cases, the mass spectra represent a series of water clusters $H^+(H_2O)_n$. However, the most intense cluster ion observed at a lower voltage amplitude corresponds to $n = 4$ (the cluster with $n = 1$

is not detected), while the maximum peak observed at a higher voltage corresponds to $n = 2$. These results confirm the effect of ion declusterization in intense alternating electric fields.

Conclusions. One of the main factors limiting the sensitivity of mass-spectrometric techniques employing ionization at elevated pressures are the losses of ions transported from the region of high pressure to vacuum. These losses are mostly related to the impossibility of providing effective ion focusing in a constant electric field at a background pressure above 10^{-3} Torr. We used the ionization by limited-current discharge and showed the possibility of increasing the sensitivity of mass spectrometry by means of ion focusing at elevated pressures in an alternating quadrupole electric field. It was also demonstrated that the focusing of ions in an alternating quadrupole electric field is accompanied by their declusterization.

REFERENCES

1. V. B. Mikheev, P. M. Irving, N. S. Laulainena, *et al.*, J. Chem. Phys. **116**, 10772 (2002).
2. J. F. J. Todd, Mass Spectrom. Rev. **10**, 3 (1991).
3. D. A. Dahl, SIMION 3D Version 6.0 User's Manual, 1995; http://citeseer.ist.psu.edu/article/dahl95users.html.
4. S. C. Brown, *Basic Data of Plasma* (AIP, New York, 1993).
5. S. L. Pozharov and P. K. Khabibulaev, *Diagnostics of the Ion Composition of Plasmas* (Tashkent, 1987) [in Russian].
6. V. V. Pervukhin, R. R. Ibragimov, and V. M. Moralev, Prib. Tekh. Éksp., No. 5, 122 (1997) [Instrum. Exp. Tech. **40**, 700 (1997)].

Translated by P. Pozdeev

Technical Physics Letters, Vol. 31, No. 7, 2005, pp. 591–594. Translated from Pis'ma v Zhurnal Tekhnicheskoĭ Fiziki, Vol. 31, No. 14, 2005, pp. 22–29.

Thermal Effects in Amorphous YBaCuO Layers under High-Power Laser Action

V. D. Okunev[a,*], V. A. Isaev[a], P. Gierlowski[b], A. Klimov[b], and S. Lewandowski[b]

[a] *Donetsk Physicotechnical Institute, National Academy of Sciences of Ukraine, Donetsk, Ukraine*

[b] *Institute of Physics, Polish Academy of Sciences, 02668 Warsaw, Poland*

** e-mail: okunev@mail.fti.ac.donetsk.ua*

Received February 8, 2005

Abstract—We have studied the effect of pulsed UV laser radiation (KrF, $\hbar\omega = 5.01$ eV, $\tau = 25$ ns) on the optical transmission and temperature distribution in amorphous YBaCuO layers. The interaction of laser radiation with such layers exhibits an adiabatic character, with an exponential decrease in the temperature in depth of the sample. The slope of the temperature profile is determined by the optical absorption coefficient for the radiation employed. The specific heat capacity of amorphous YBaCuO is $c = 1.15$ J/(g K). © *2005 Pleiades Publishing, Inc.*

The interaction of optical radiation with high-temperature superconductors (HTSCs) attracts much attention, which is related to the unique nature of charge carriers in such materials. Indeed, the existence of HTSC compounds (such as YBaCuO) in a dielectric form stimulates the investigation into phenomena related to the charge carrier generation, the dielectric–metal transition, and the nonequilibrium superconductivity. Using laser radiation, it is possible to enhance the effects caused by the photogeneration of nonequilibrium carriers [1], to influence the atomic order in a target [2–4], and to observe phase transitions under nonequilibrium conditions. Such experiments are especially interesting in disordered systems characterized by a high mobility of structural elements [5–7].

The knowledge of thermal processes, which play an important role in practically all phenomena of this kind, requires the quantitative evaluation of changes ΔT in the average temperature of irradiated YBaCuO films. Attempts at determining ΔT using the well-known formula

$$\Delta Q = cm\Delta T \qquad (1)$$

(where ΔQ is the energy increment, c is the heat capacity, and m is the mass) lead to considerable uncertainties, which are caused by a large scatter in the available data on the heat capacity of YBaCuO (related to the strong dependence of this characteristic on the temperature and structure of samples [8–12]).

This situation leads to the need for experimental determination of the temperature of samples. We have performed such measurements using a structure that is depicted in the inset to Fig. 1. The structure comprises a quartz glass substrate (transparent for the laser radiation employed) covered by a thin (~1000 Å) copper film with a calibrated temperature dependence of the resistance. By measuring changes in the resistance of this copper film, it was possible to estimate the temperature of a sample under the action of laser pulses. The samples were prepared by depositing amorphous YBaCuO layers onto the copper-covered glass substrates. The deposition was performed by sputtering a stoichiometric $YBa_2Cu_3O_{7-\delta}$ target in an oxygen atmosphere (P = 270 mTorr) with the aid of a KrF excimer laser ($\hbar\omega$ = 5.01 eV, $\tau = 25$ ns, $f = 10$ Hz, $F = 1.5$ J/cm^2). The conditions of layer growth, except for the substrate temperature ($T_s = 300$ K) and type (quartz glass), were close to

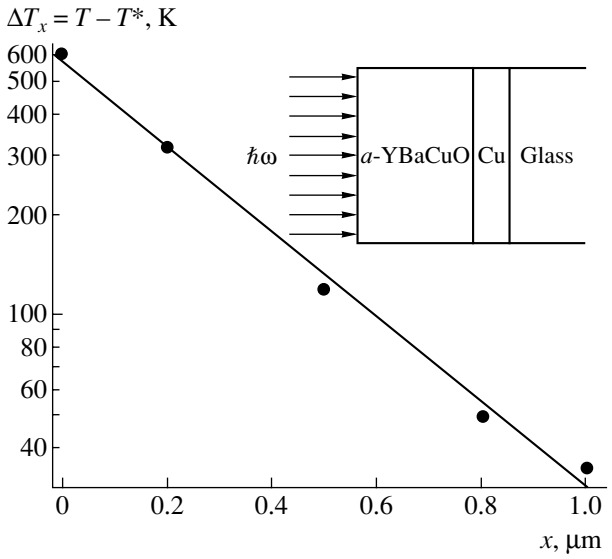

Fig. 1. Temperature variation in depth of amorphous YBaCuO films irradiated by laser pulses with an energy density of 0.1 J/cm^2. The inset shows a schematic diagram of the sample and the experimental arrangement.

1063-7850/05/3107-0591$26.00 © 2005 Pleiades Publishing, Inc.

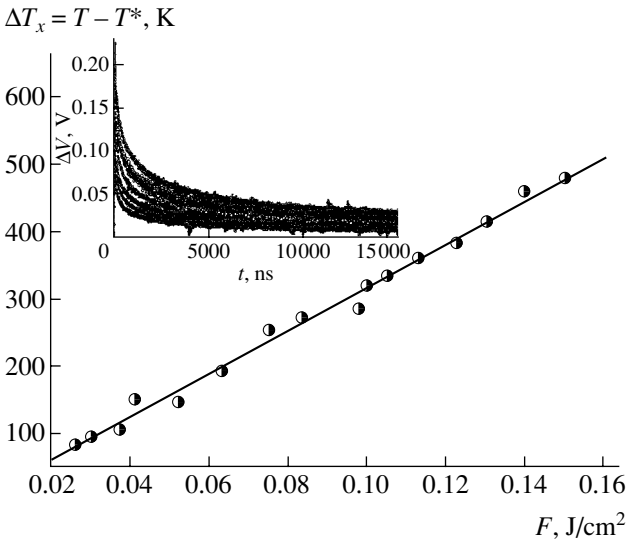

Fig. 2. A linear relation between the local temperature in the amorphous layer (x = 0.2 μm) and the laser energy density. The inset shows oscillograms of the response signal (temperature kinetics) of a copper temperature sensor.

the optimum regime for obtaining epitaxial crystalline YBaCuO films in the on-axis geometry relative to the plasma plume [13]. In subsequent experiments, the obtained sample structures were exposed to radiation of the same KrF laser, but these exposures were carried out in air (outside the vacuum chamber) at T = 295 K. The maximum laser energy density ($F < 0.3$ J/cm^2) was below the sputter threshold for the YBaCuO target [14]. In addition, we checked the structure (by X-ray diffraction) and measured the optical transmission spectra of irradiated samples.

The dependence of the copper film resistance on the laser pulse energy showed no hysteresis depending on the direction of energy variation. This behavior was related to the short duration of laser pulses and to the low susceptibility of glassy YBaCuO layers to crystallization.

If the optical absorption coefficient is independent of the laser radiation intensity, the transmitted radiation is attenuated according to the exponential law,

$$I = I_0 f(R) \exp(-\alpha_{\mathrm{YBCO}}^{(0)} d), \quad (2)$$

where d is the amorphous layer thickness and $f(R)$ is a function of the reflection coefficient R (in the simplest case, $f(R) = 1 - R$). If the heat exchange during the laser pulse action can be ignored and the YBaCuO layer heating can be considered as a purely adiabatic process, the temperature increment $\Delta T_x = T - T^*$ (where T is the local temperature in the sample and T^* is the ambient temperature) is proportional to the laser radiation intensity and obeys a relation analogous to formula (2):

$$\Delta T_x = T_0 f(R) \exp(-\alpha_{\mathrm{YBCO}}^{(T)} x), \quad (3)$$

where x is the coordinate measured in the direction of radiation propagation. Assuming that the copper film completely absorbs radiation transmitted through the YBaCuO layer (this assumption agrees with the results of measurements), the energy balance in the system can be written as

$$J = \Delta Q_{(\mathrm{YBCO})} + \Delta Q_{(\mathrm{Cu})}, \quad (4)$$

where J is the absorbed laser pulse energy. The amount of energy absorbed in the amorphous film and converted into heat (per unit surface area) is

$$\Delta Q_{(\mathrm{YBCO})} = c_{(\mathrm{YBCO})} m \Delta T \sim \frac{1}{d} \int_0^d \exp(-\alpha_{\mathrm{YBCO}}^{(T)} x) dx. \quad (5)$$

The temperature response (ΔT_x) as a function of the laser energy density is described by a linear dependence (Fig. 2). An analysis of the oscillograms showing the time variation of the copper film resistance under the action of laser pulses (see the inset in Fig. 2) indicated that the inertia of the amorphous layer–copper film–glass substrate system (determined by the processes of heat redistribution) is two to three orders of magnitude greater than the laser pulse duration. Therefore, in considering the amorphous film heating by laser radiation, we can ignore the process of heat transfer. For the adiabatic interaction of laser radiation with the structure depicted in Fig. 1, the temperature at the interface between the YBaCuO layer with thickness d_i and the Cu film is $T_{di} = f(R_{\mathrm{YBCO}}) T_0 \exp(-\alpha_{\mathrm{YBCO}}^{(T)} d_i)$. On the passage to the copper film–substrate interface, the temperature decreases to $T_{\mathrm{Cu–G}} = f(R_{\mathrm{YBCO}}) T_0 \exp(-\alpha_{\mathrm{YBCO}}^{(T)} d_i) f(R_{\mathrm{YBCO–Cu}}) \exp(-\alpha_{\mathrm{Cu}} d_{\mathrm{Cu}})$. When the temperatures on the copper film surfaces become $f(R_{\mathrm{YBCO}}) T_0 \exp(-\alpha_{\mathrm{YBCO}}^{(T)} d_i) f(R_{\mathrm{YBCO–Cu}})$ and $f(R_{\mathrm{YBCO}}) T_0 \exp(-\alpha_{\mathrm{YBCO}}^{(T)} d_i) f(R_{\mathrm{YBCO–Cu}}) \exp(-\alpha_{\mathrm{Cu}} d_{\mathrm{Cu}})$, the average temperature of this film increases by

$$\Delta T_i = \frac{f(R_{\mathrm{YBCO}}) T_0 \exp(-\alpha_{\mathrm{YBCO}}^{(T)} d_i) f(R_{\mathrm{YBCO–Cu}}) [1 - \exp(-\alpha_{\mathrm{Cu}} d_{\mathrm{Cu}})]}{\varphi}, \quad (6)$$

where φ depends on the procedure of temperature averaging over the copper film thickness (in the simplest case, φ = 2). By the same token, the average temperature increment for the amorphous YBaCuO layer with thickness d_j is

$$\Delta T_j = \frac{f(R_{\mathrm{YBCO}})T_0 \exp(-\alpha^{(T)}_{\mathrm{YBCO}} d_j) f(R_{\mathrm{YBCO-Cu}})[1 - \exp(-\alpha_{\mathrm{Cu}} d_{\mathrm{Cu}})]}{\varphi}. \quad (7)$$

Thus, the ratio of temperature increments $\Delta T_i/\Delta T_j$ for two YBaCuO films with thicknesses d_i and d_j is

$$\frac{\Delta T_i}{\Delta T_j} = \exp[-\alpha^T_{\mathrm{YBCO}}(d_j - d_i)]. \quad (8)$$

This ratio is independent of some parameters of the sample structure, the measuring system, and the procedure of temperature averaging over the copper film thickness. As can be seen from formulas (6)–(8), the α^T_{YBCO} value can be determined even without the requirement of complete absorption of laser radiation by the metal film. Proceeding from the experimental data for YBaCuO layers with thicknesses $d_1 = 2000$ Å and $d_2 = 5000$ Å, we obtained $\alpha^T_{\mathrm{YBCO}} = 3.26 \times 10^4$ cm^{-1}, while the $\Delta T_i/\Delta T_j$ ratio determined for two YBaCuO films with thicknesses $d_i = 0.5$ μm and $d_j = 1.0$ μm yielded $\alpha^T_{\mathrm{YBCO}} = 2.46 \times 10^4$ cm^{-1}. The average result is $\alpha^T_{\mathrm{YBCO}} = 2.86 \times 10^4$ cm^{-1}, which coincides to within 15% with the optical absorption coefficient of $\alpha^0_{\mathrm{YBCO}} = 2.5 \times 10^4$ cm^{-1} for $\hbar\omega = 5$ eV.

The results of processing of the data on the optical transmission of radiation with $\hbar\omega = 5$ eV by the YBaCuO films with various thicknesses in the region where the transmission is independent of the laser pulse energy showed that the reflection coefficient is about 10%. For $R_{\mathrm{YBCO}} = 0.1$, we obtained $T_0 = 684$°C. Using the procedure described above, we have also determined the temperature in several other points. As expected, the temperature variation in depth of the YBaCuO layer has an exponential character (Fig. 1) and is described by relation (3) with $\alpha^T_{\mathrm{YBCO}} = 2.9 \times 10^4$ cm^{-1}.

Figure 3 shows the optical transmission spectra of a film with $d = 2500$ Å measured before and after laser irradiation (45 pulses with the energies varying from 30 to 270 mJ cm^2). As can be seen from the model of the density of states in YBaCuO depicted in the inset to Fig. 3, the edges of the valence (E_{V}) and conduction (E_{C}) bands are smeared, and the density of states has extended tails [7]. The intensity of optical transitions (O2p ⟶ Cu3d) via a gap with charge transfer (E_{CT}) is small and is determined for the most part by the presence of a small number of crystalline clusters known to act as the sources of internal stresses and localized states in amorphous films [6, 7, 15]. Owing to the localization of electron states in the Cu3d^{10} band, the role of the conduction band is performed by the Cu4s^1 band, while the optical absorption edge is shifted to $\hbar\omega >$ 4 eV [7].

The obtained YBaCuO samples were stable with respect to laser irradiation: changes in the optical transmission spectra of irradiated samples were small and only noticeable in the middle part of the spectrum. Indeed, these changes did not exceed 2–3% at $\hbar\omega \cong$ 5 eV and were one order of magnitude greater at $\hbar\omega =$ 2.5–4.5 eV. It should be noted that the optical spectra of HTSCs at $\hbar\omega > 4$ eV are weakly sensitive even to significant changes in the structure, such as the phase transitions from amorphous to crystalline state [7, 16]. Moreover, the combination of the low susceptibility of the amorphous YBaCuO layers to crystallization and the short duration of laser pulses in our experiments allowed the film structure to remain virtually unchanged even at high (up to the melting point) temperatures. The temperature profile in depth of the amorphous YBaCuO layer is described by the relation $T_x = f(R_{\mathrm{YBCO}})T_0 \exp(-\alpha^{(T)}_{\mathrm{YBCO}} x)$. Then, the average temperature in the amorphous layer is

$$T_{\mathrm{av}} = \frac{1}{d} f(R_{\mathrm{YBCO}})T_0 \int_0^d \exp(-\alpha^{(T)}_{\mathrm{YBCO}} x)dx = \frac{1}{\alpha d} f(R_{\mathrm{YBCO}})T_0[1 - \exp(-\alpha^{(T)}_{\mathrm{YBCO}} d)]. \quad (9)$$

Using relation (1), the heat capacity can be expressed as $c = \Delta Q/m\Delta T$. For $F = 0.1$ J/cm^2 and $d = 2.5 \times 10^{-5}$ cm, we obtain $T_{\mathrm{av}} = 467.3$°C. This yields $c = 1.15$ J/(g K), which is somewhat greater than the value $c = 1.0$ J/(g K)

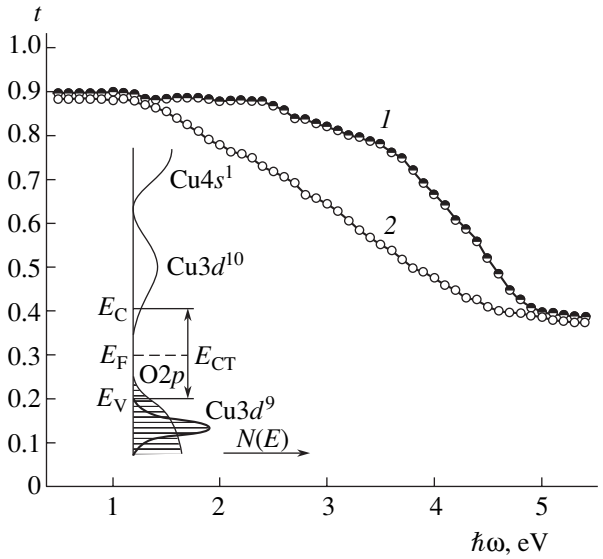

Fig. 3. Optical transmission spectra of an amorphous YBaCuO film with a thickness of $d = 2500$ Å measured (*1*) before and (*2*) after laser irradiation. The inset shows a model of the density of states for amorphous YBaCuO.

reported for crystalline $YBa_2Cu_3O_{7-\delta}$ [8] at high temperatures.

Acknowledgments. The authors are grateful to Z.A. Samoilenko and E.I. Pushenko for carrying out the X-ray diffraction investigation of samples.

This study was supported in part by the Polish Government Grant No. 2P03B04423.

REFERENCES

1. R. Adam, W. Kula, R. Sobolewski, *et al.*, Appl. Phys. Lett. **67**, 3801 (1995).
2. A. Bock, R. Kursten, M. Bruhl, *et al.*, Phys. Rev. B **54**, 4300 (1996).
3. Y. B. Li, C. Shelley, L. F. Cohen, *et al.*, J. Appl. Phys. **80**, 2929 (1996).
4. M. N. Iliev, H. U. Habermeier, M. Cardona, *et al.*, Physica C **279**, 63 (1997).
5. N. F. Mott and E. A. Davis, *Electronic Processes in Non-Crystalline Materials* (Clarendon, Oxford, 1979; Mir, Moscow, 1982).
6. J. Konopka, V. D. Okunev, Z. A. Samoilenko, *et al.*, Physica C **341**–**348**, 2147 (2000).
7. V. D. Okunev, Z. A. Samoilenko, A. Abal'oshev, *et al.*, Phys. Rev. B **62**, 696 (2000).
8. S. Otsubo, T. Minamikawa, Y. Yonezawa, *et al.*, Jpn. J. Appl. Phys. **29**, L73 (1990).
9. P. C. Shan, Z. Celik-Butler, D. P. Butler, *et al.*, J. Appl. Phys. **80**, 7118 (1996).
10. Yu. D. Varlamov, A. N. Volkov, M. R. Predtechenskiĭ, *et al.*, Sverkhprovodimost: Fiz. Khim. Tekh. **5**, 1736 (1992).
11. M. Onuki, T. Fujiyoshi, H. Ohsumi, *et al.*, Physica C **235**–**240**, 1383 (1994).
12. H. Fujishiro, M. Ikebe, T. Naito, *et al.*, Physica C **235**–**240**, 825 (1994).
13. V. D. Okunev, Z. A. Samoilenko, A. Abal'oshev, *et al.*, Appl. Phys. Lett. **75**, 1949 (1999).
14. R. K. Singh and J. Narayan, Phys. Rev. B **41**, 8843 (1990).
15. V. D. Okunev, Z. A. Samoilenko, V. M. Svistunov, *et al.*, J. Appl. Phys. **85**, 7282 (1999).
16. V. D. Okunev and T. A. D'yachenko, Fiz. Tverd. Tela (St. Petersburg) **35**, 3076 (1993) [Phys. Solid State **35**, 1514 (1993)].

Translated by P. Pozdeev

Technical Physics Letters, Vol. 31, No. 7, 2005, pp. 595–596. Translated from Pis'ma v Zhurnal Tekhnicheskoĭ Fiziki, Vol. 31, No. 14, 2005, pp. 30–33.

Specific Features of the Frequency Dependence of the Horizontal Magnetic Field Components in the Ultralow and Extremely Low Frequency Range

E. D. Tereshchenko, A. E. Sidorenko, V. F. Grigor'ev, A. N. Vasil'ev, L. A. Sobchakov, and A. V. Vasil'ev

Polar Geophysical Institute, Kola Scientific Center, Russian Academy of Sciences, Murmansk, Russia
All-Russia Institute of High-Power Radio Engineering, St. Petersburg, 194021 Russia
e-mail: general@pgi.ru

Received September 27, 2004

Abstract—The frequency dependence of the horizontal magnetic field components in the ultralow and extremely low frequency range has been experimentally studied using an artificial signal source. The experimental data significantly differ from the results of calculations performed using the model of a homogeneous Earth's surface layer. © *2005 Pleiades Publishing, Inc.*

Artificial electromagnetic fields in the ultralow (ULF) and extremely low (ELF) frequency range can be effectively used both for studying the state of the ionosphere [1] and for deep probing of the Earth's Crust [2]. This Letter presents for the first time the results of experiments on the generation and measurement of electromagnetic fields in the range of frequencies from 1 to 130 Hz. The aim of our study was to determine the frequency dependence of the amplitude of horizontal magnetic field components in the ULF and ELF range.

The experiments were performed on the Kola peninsula. The field was generated at eight frequencies in the range from 1 to 130 Hz. The time of the source operation at each frequency was 10–15 min. The electromagnetic field was generated by a horizontal antenna with a length of 56.5 km and was detected by a specially designed induction magnetometer at a distance of 80 km from the source. The magnetometer was equipped with two orthogonal antennas oriented relative to the magnetic meridian (with H component directed toward the magnetic north, D component oriented westward, and an eastern magnetic declination of 11°). The receiving antennas comprised identical coils of about 2.3×10^5 turns wound on ferrite cores, which were mounted on special rigid nonmagnetic bases and arranged at a distance of at least 150 m from any commercial 50-Hz interference source.

The detected signal at each frequency was accumulated for a time of up to 3 min and digitally processed, which provided for a quite good signal-to-noise ratio. The signal was digitized at a frequency of 5 kHz synchronously in two channels corresponding to the D and H components. The useful signal was separated within a frequency band of 0.05 Hz. Statistical processing of the experimental data yielded averaged amplitudes of the D and H components at eight frequencies in the range studied.

Figures 1 and 2 show the results of these measurements. For comparison, we also present the results of calculations of the H_x and H_y components corresponding to the experimental geometry, which were performed within the framework of the model of a homogeneous Earth's surface layer with a conductivity of $\sigma = 4.7 \times 10^{-5}$ S/m.

According to this model, the H_x and H_y components for a linear horizontal radiator in the presence of an Earth–atmosphere interface are given by the formulas

$$H_x = \frac{J_x}{2\pi} y \left[\frac{I_1\left(\frac{\rho_2\kappa_1}{2}\right)K_1\left(\frac{\rho_2\kappa_1}{2}\right)}{\rho_2^2} - \frac{I_1\left(\frac{\rho_1\kappa_1}{2}\right)K_1\left(\frac{\rho_1\kappa_1}{2}\right)}{\rho_1^2} \right], \quad (1)$$

$$H_y = \frac{J_x}{2\pi}\left[\frac{\kappa_1^2}{8}\int_{-L}^{L}\left[I_0\left(\frac{\rho\kappa_1}{2}\right)K_0\left(\frac{\rho\kappa_1}{2}\right) - I_2\left(\frac{\rho\kappa_1}{2}\right)K_2\left(\frac{\rho\kappa_1}{2}\right)\right]d\eta + \frac{L+x}{\rho_1^2} I_1\left(\frac{\rho_1\kappa_1}{2}\right)K_1\left(\frac{\rho_1\kappa_1}{2}\right) \right. \quad (2)$$

$$\left. + \frac{L-x}{\rho_2^2} I_1\left(\frac{\rho_2\kappa_1}{2}\right)K_1\left(\frac{\rho_2\kappa_1}{2}\right)\right],$$

1063-7850/05/3107-0595$26.00 © 2005 Pleiades Publishing, Inc.

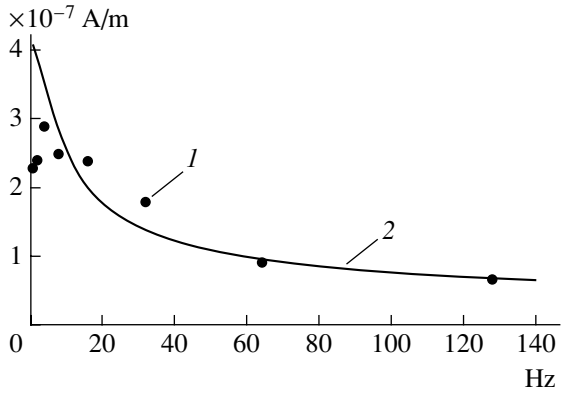

Fig. 1. Frequency dependence of the *D* component of the magnetic field strength: (points *1*) experimental data; (curve *2*) results of model calculations.

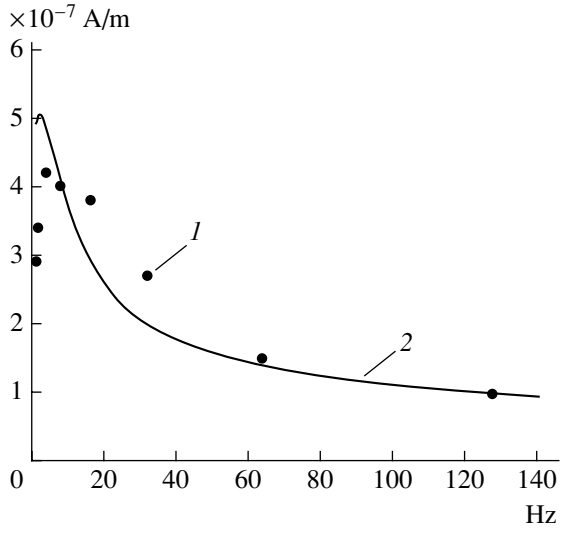

Fig. 2. Frequency dependence of the *H* component of the magnetic field strength: (points *1*) experimental data; (curve *2*) results of model calculations.

where J_x is the current in the radiator; (x, y) are the coordinates of the point of observation; I and K are the modified Bessel functions; $2L$ is the radiator length; ρ is the distance to the current point of integration over the antenna with the abscissa η; $\kappa_1 = (1 - i)/\sqrt{\omega\sigma\mu_0/2}$, i is the imaginary unity; f is the frequency; $\omega = 2\pi f$ is the cyclic frequency; σ is the conductivity of the Earth's surface layer; and μ_0 is the magnetic constant. The time dependence was selected in the form of $\exp(-i\omega t)$.

As can be seen from Figs. 1 and 2, there are significant differences in the 1–50 Hz frequency interval between experimental data and the results of calculations using the model of a homogeneous Earth's surface layer. The discrepancy is especially pronounced in the region of 1–8 Hz.

Taking into account that the skin layer thickness Z_c is related to the frequency and conductivity as $Z_c = 503/\sqrt{f\sigma}$, we may conclude that the assumption concerning the homogeneity of the Earth's surface layer is valid on the Kola peninsula only to within a depth of 15–20 km. Deeper layers may possess differing conductivities. In particular, a layer of higher conductivity occurs at a depth of about 40 km.

REFERENCES

1. M. Füllekrug, A. C. Fraser-Smith, and K. Schlegel, Europhys. Lett. **59**, 626 (2003).
2. M. N. Berdichevskii, *Electrical Surveying by Means of Telluric Currents* (Nedra, Moscow, 1968; National Lending Library for Science and Technology, Boston Spa, 1963).

Translated by P. Pozdeev

Technical Physics Letters, Vol. 31, No. 7, 2005, pp. 597–599. Translated from Pis'ma v Zhurnal Tekhnicheskoĭ Fiziki, Vol. 31, No. 14, 2005, pp. 34–39.

Vacuum Gauges with Emitters Based on Carbon Nanotubes

S. J. Kim

Division of Electronics and Electrical Engineering, Kyungnam University, Masan, 631701 Korea

e-mail: sjki1216@kyungnam.ac.kr

Revised manuscript received March 15, 2005

Abstract—New vacuum gauges with emitters based on carbon nanotubes (CNTs) are described. The relation between the field emission from CNTs and the residual pressure in the vacuum chamber is considered. The operation of the proposed pressure sensor obeys the electric discharge theory based on the Paschen law, whereby the pressure is determined by measuring the discharge current as a function of the concentration of a gas (air) ionized as a result of the collisions with electrons emitted from CNTs. © *2005 Pleiades Publishing, Inc.*

In recent years, it has been convincingly demonstrated that carbon nanotubes (CNTs) offer a wide range of potential applications, such as electron emitters [1, 2], room-temperature transistors [3], hydrogen accumulators [4], and chemical sensors [5]. Special attention of researchers has been devoted to the process of field electron emission from CNTs, which is explained by the excellent emission characteristics of these materials. However, investigations in this direction are mostly concentrated on studying the possibility of creating CNT-based flat field-emission displays, since these devices offer broad commercial prospects and a huge market.

This Letter presents a new promising application of CNTs in vacuum gauges, where these materials are also used as effective electron emitters. As a rule, the level of vacuum is evaluated by measuring changes in the pressure-sensitive physical properties (thermal conductivity, electric discharge, ionization probability, etc.), which depend on the residual gas pressure. The modern arsenal of devices intended for vacuum measurements is very broad, including Geissler tubes, Pirani and Penning gauges, and ionization transducers. This paper will demonstrate the possibilities of a new vacuum gauge, in which CNTs are used as field electron emitters.

The proposed vacuum sensor device has a three-layer structure comprising the emitter, insulating spacer, and anode. The electron emitters (CNTs) were grown on 4-inch *p*-Si(100) single crystal wafers. The substrate surface was first coated by sputter-deposited titanium and then with an electron-beam-deposited 10-nm-thick film of iron, which served as a catalyst for the CNT growth. The catalyst layer was patterned using the photolithographic, masking, and lift-off techniques, so as to ensure homogeneous CNT growth on a 2×2 mm area. Prior to CNT growth, the wafers were separated into 12×12 mm [6, 7]. The CNTs were grown by chemical vapor deposition (CVD), whereby C_2H_2 flow was passed via the reactor at a flow rate of 30 cm^3/s. The CNTs were deposited for 10 min onto substrates kept at a temperature of 850°C. The structure of a CNT electron emitter is schematically depicted in Fig. 1a. The emitter was insulated from the anode by a 500-μm-thick layer (spacer) of Pyrex glass engraved using the sand-blast method so as to provide the access

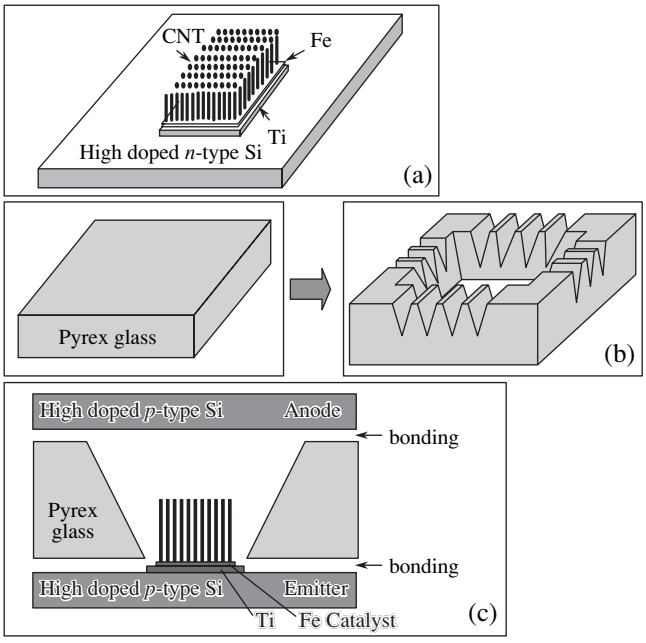

Fig. 1. Schematic diagrams illustrating the vacuum gauge design and technology: (a) CNT electron emitter; (b) Pyrex glass spacer manufactured by sand-blast technology; (c) device assembly (see the text for explanations).

1063-7850/05/3107-0597$26.00 © 2005 Pleiades Publishing, Inc.

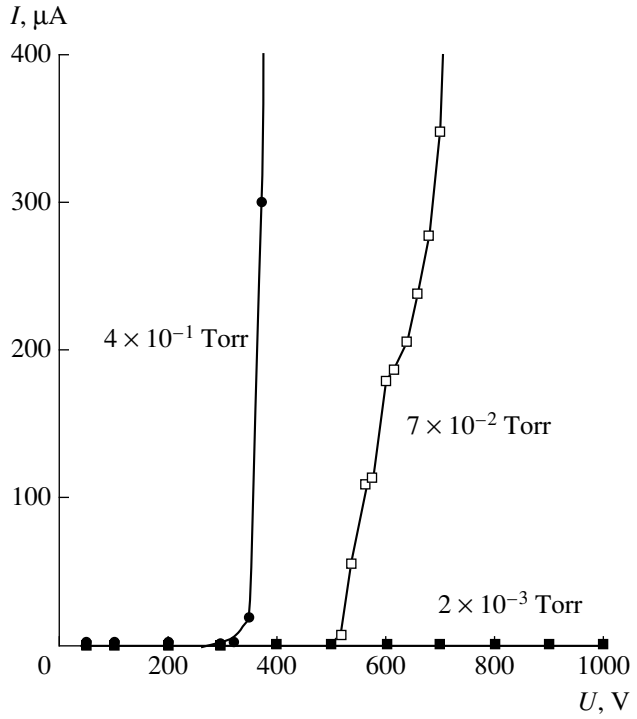

Fig. 2. Current–voltage characteristics of the CNT electron emitter measured at various pressures.

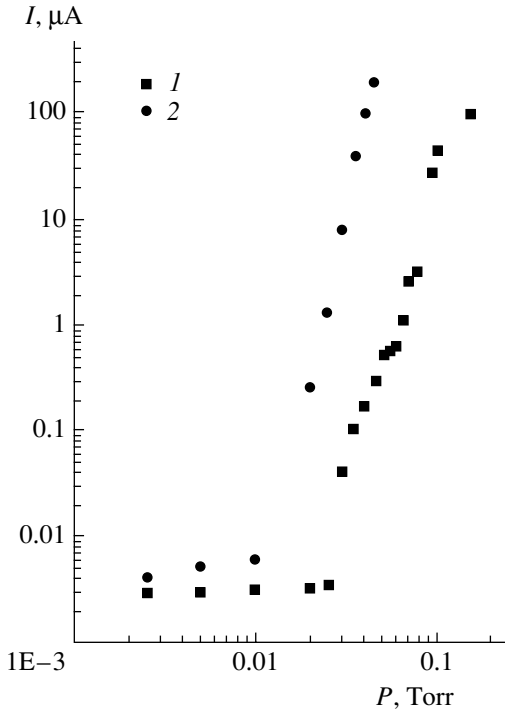

Fig. 3. Plots of the discharge current versus residual gas pressure at an applied voltage of (*1*) 500 and (*2*) 1000 V.

of air to the region of the emitter and to the surface covered with a protective mask (Fig. 1b). The CNT electron emitters and the anode electrodes made of heavily doped silicon were assembled with glass spacers as depicted in Fig. 1c and bonded by Si/glass anodic process at 400°C.

The field emission measurements were performed using a voltage source with U_{max} = 1000 V (which corresponded to an electric field strength of 2×10^6 V/m) connected via a current-limiting resistor. The measurements were performed in a range of pressures from 10^{-1} to 10^{-3} Torr. The upper limit was determined by the appearance of glow discharge (initiated at 10^{-1} Torr). The discharge current was measured using a Keithley 2425 Source Meter.

Electrons emitted from CNTs move in the applied electric field toward the anode and collide with neutral molecules of the residual gas. These collisions produce some ionization, which implies the formation of secondary electrons and positive ions. The appearance of secondary electrons is manifested by an increase in the current, which is proportional to the residual gas concentration. We have studied the field emission at various residual gas pressures. Figure 2 shows the current–voltage (*I–U*) characteristics measured for two levels of vacuum in the system. In a relatively high vacuum (i.e., at a relatively low residual gas pressure) of 2×10^{-3} Torr, the current does not exceed 1 μA at an applied voltage of up to 1 kV. In contrast, the current exhibits a sharp increase above 500 V at a pressure of 7×10^{-2} Torr, and even below 400 V at 4×10^{-1} Torr. The current buildup observed at a relatively high pressure is probably due to the appearance of secondary electrons as a result of the electron impact ionization.

Figure 3 shows plots of the current versus residual gas pressure at various applied constant voltages (500 and 1000 V). As can be seen, the current exhibits a sharp increase when the pressure reaches a certain critical level (this threshold being dependent on the voltage). This implies that there is a certain minimum gas concentration that is necessary for the formation of the secondary electron cascade. The critical gas pressure was about 3×10^{-2} Torr at 500 V, and about 1×10^{-2} Torr at 1000 V, thus decreasing with an increase in the voltage.

To summarize, new vacuum sensors were manufactured using CNT-based electron emitters in silicon-glass-anode structures fabricated using the conventional silicon technology. The field emission in these devices was studied as a function of the residual gas pressure. The obtained results show that the proposed vacuum sensors can be used as vacuum gauges in the range of pressures from 10^{-1} to 10^{-3} Torr.

Acknowledgments. The author is grateful to the laboratory headed by Prof. Nakayama (Osaka Univer-

sity, Japan) for kindly providing the technology of titanium and iron deposition.

This study was supported by the Academic Research Foundation of the Kyungnam University (2004 Program).

REFERENCES

1. N. S. Lee, D. S. Chung, I. T. Han, *et al.*, Diamond Relat. Mater. **10**, 265 (2001).
2. S. A. Gavrilov, E. A. Ilichev, E. A. Poltoratskiĭ, *et al.*, Zh. Tekh. Fiz. **55** (1), 108 (2004) [Tech. Phys. **49**, 108 (2004)].
3. P. Avouris, J. Appenzeller, R. Martel, *et al.*, Proc. IEEE **91**, 1772 (2003).
4. H. Zhang, Y. Chen, S. Li, *et al.*, J. Appl. Phys. **94**, 6417 (2003).
5. M. Penza, G. Cassano, P. Aversa, *et al.*, Appl. Phys. Lett. **85**, 2379 (2004).
6. S. Fan, M. G. Chapline, N. R. Franklin, *et al.*, Science **283**, 512 (1999).
7. C. J. Lee, D. W. Kim, T. J. Lee, *et al.*, Chem. Phys. Lett. **312**, 461 (1999).

Translated by P. Pozdeev

Technical Physics Letters, Vol. 31, No. 7, 2005, pp. 600–602. Translated from Pis'ma v Zhurnal Tekhnicheskoĭ Fiziki, Vol. 31, No. 14, 2005, pp. 40–44.

Imaging Traps in Oxide Semiconductors with the Aid of Thermostimulated Electron Emission

S. N. Nagornykh[a,*] and V. I. Pavlenkov[b,]**

[a] *Nizhni Novgorod State Pedagogical University, Nizhni Novgorod, Russia*
[b] *Arzamas State Pedagogical University, Arzamas, Russia*
*e-mail: *@algoritm@sandy.ru; **@agpi@nts.ru*
Received March 2, 2005

Abstract—The patterns of thermostimulated electron emission from an iron–nickel alloy reveal fluctuations in the density of charged point defects in the surface oxide layer of the alloy sample. *© 2005 Pleiades Publishing, Inc.*

As is known, partly disordered semiconductors feature fluctuations in the density of charged defects, which lead to bending of the conduction band bottom, fluctuations of the energy of charged impurities, etc. [1, 2]. It would be difficult to image such fluctuations by measuring the hopping conductivity, since this characteristic significantly depends on the volume properties of a given semiconductor and the role of contacts is unknown. Various surfaces have been imaged using the phenomenon of thermionic emission [3], but the stationary current and the temperature are usually so high that the emitter acquires equilibrium electron and atomic structures.

The phenomenon of thermostimulated electron emission has been employed for the investigation of various materials at lower temperatures and currents. For this reason it was possible to study, for example, the kinetics of the density of defects (divacancies) created by ion bombardment of the rear sample surface (opposite to that where the electron emission was measured) [4] or the electric-field-induced modulation of the defect (impurity) energy [5]. Therefore, it may be expected that the thermostimulated electron emission will also be sensitive with respect to the fluctuations of defects, such as electron traps, in the near-surface layers of solids. The aim of this study was to image such fluctuations by measuring the thermostimulated electron emission from oxidized metal surfaces in vacuum (10^4 Pa) with the aid of a microchannel plate and a luminescent screen [6].

The experiments were performed with the aid of a FNS-5 alloy prepared by sintering an iron–nickel powder mixture used in filters. The oxide layer on this alloy represents a partly disordered, weakly doped compensated semiconductor with a high density of point defects, including oxygen vacancies (donors) and interstitial metal atoms (acceptors) on the surface of metal particles linked by diffusion bridges.

In the course of thermal stimulation, the sample surface image on the luminescent screen exhibited the following changes:

(i) $T < 200$°C, no luminescence;

(ii) $T = 200$–220°C, separate scintillations;

(iii) $T = 230$–300°C, bright spots (Fig. 1a);

(iv) $T = 300$–330°C, emission from most of the surface (Fig. 1b);

(v) $T > 330$°C, quenching of the luminescence (Fig. 1c).

The observed variations in the distribution of the electron emission intensity over the sample surface in the quasi-stationary case can be explained by changes in the distribution of the free electron density in the oxide layer under the action of an external medium with white noise [2]. In our case, the role of the external medium is played by the thermoactivated diffusion process of a change in the area of bridges between particles of the alloy characterized by a large intensity of diffusion jumps and a large viscosity.

The observed pattern of changes in the distribution of the electron emission current density over the sample surface can be interpreted as follows:

(i) The oxygen vacancies are not ionized and the free electron density in the oxide layer is zero ($n = 0$);

(ii) The process of thermoionization of the oxygen vacancies is initiated, but the temperature is low and the ionization rate is small (n fluctuates around zero, and zero is the most probable value);

(iii) The most probable n value in some local regions becomes nonzero, since electrons are accumulated at the sites of depression of the conduction band bottom;

(iv) The electron emission proceeds from the entire surface, rather from the areas with increased density of oxygen vacancies;

1063-7850/05/3107-0600$26.00

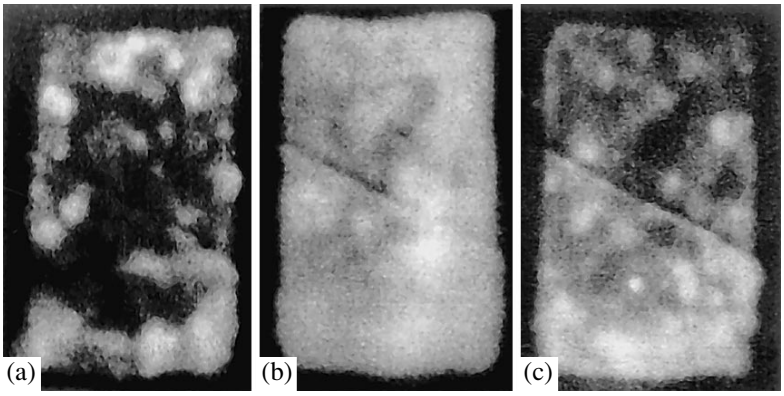

Fig. 1. Temperature-dependent variations in the distribution of the electron emission current density over the surface of a Fe–Ni alloy (FNS-5) observed at T = 230 (a), 270 (b), and 340°C (c) and a thermostimulation rate of 0.45 K/s. The size of the image obtained with the aid of a microchannel plate and a luminescent screen is 8×11 mm at a resolution of 2 lines/mm.

(v) Devastation of the filled oxygen vacancies leads to a decrease in the area of emitting surface regions and eventually $n \approx 0$.

It should be noted that a change in the relief of the conduction band bottom in the course of thermostimulated electron emission is accompanied by variations in the size and arrangement of bright spots on the sample surface image.

The approximation of the strongly compensated weakly doped semiconductor [1] takes into account the presence of large-scale fluctuations in the density of charged defects, which interact with each other according to the Coulomb law and modify the position of the Fermi level relative to the conduction band bottom. The screening radius is related to the total concentration of impurities $N_t = N_A + N_D$ (acceptors and donors, respectively) and the degree of compensation $K = N_A/N_D$ ($K \approx 1$). The contribution of free electrons to the screening can be ignored. Under these conditions, the average magnitude of fluctuations in the electron potential energy in the field of charged defects is

$$\gamma(r) = e^2 N_t^{2/3}/\kappa\nu^{1/3}, \quad (1)$$

where e is the electron charge, κ is the permittivity of the medium, and ν is the average concentration of neutral donors. This average magnitude corresponds to the screening radius

$$e = 2^{2/3} N_t^{-1/3}/(1-K)^{2/3}. \quad (2)$$

The same magnitude must be characteristic of the quasi-stationary fluctuations in the density of the emission current ($J \sim \nu$) from the oxide, since the accumulation of positively charged impurities in a certain region of the semiconductor causes the transport of electrons to this region and their localization at the oxygen vacancies. Therefore, the screening radius may correspond to the size of the surface region with increased rate of the thermostimulated electron emission. Fluctuations in the ν value are equivalent to the motion of a particle (fluctuon) with friction along the ν coordinate in the random potential. It should be noted that an analysis in terms of the Blokhintsev equation also assumes the existence of immobile fluctuons [7], but these particles are not taken into consideration here.

Using the experimental temperature dependence of the thermostimulated electron emission current, we have calculated some parameters of a surface oxide film on the iron–nickel alloy studied [8]: ε = 1.19 eV; χ = 1.15 eV; density of oxygen vacancies on the oxide surface, $N_t = 3 \times 10^{20}$ m^{-3}; density of neutral oxygen vacancies at a temperature of the onset of stimulation, 10^{16} m^{-3}; degree of compensation, K = 0.99997. Substituting these values and formulas (1) and (2), we can estimate the average values of the screening radius (2×10^{-3} m) and the magnitude of fluctuations of the conduction band bottom (0.05 eV). The average size of electron emission fluctuations observed in Fig. 1c agrees with the estimate obtained for the screening radius. Variations of the average ε value within 0.05 eV must lead, according to [8], to a shift in the temperature position of the emission maximum approximately by 30°C, which is manifested by a temperature-dependent variation in the distribution of the active emission regions over the sample surface.

The distribution function of the probability of emitting regions (bright spots) determined for the patterns in Fig. 1 corresponds to a solution of the stationary Fokker–Planck–Kolmogorov equation for the ν kinetics (Ferhulst–Arnold bifurcation) [2]. This function can be written as

$$p_s(x) = N_0 x^{2\lambda/\sigma^2 - 1} \exp(-2x/\sigma^2), \quad (3)$$

where σ^2 is the external noise intensity, λ is a predetermined parameter, and N_0 is the normalization factor. Depending on the temperature, the system features the

sequential realization of three particular cases: $\lambda < 0$, $0 \le \lambda < \sigma^2/2$ (Fig. 1a), and $\lambda > \sigma^2/2$ (Fig. 1b). These cases correspond to the three distribution functions.

By analogy with [1], a disorder in the oxygen vacancies corresponds to the Poisson distribution. For this reason, we may ascertain that the typical screening radius estimated using relation (2) corresponds to the experimentally observed dimensions of active emission regions on the sample surface. Thus, we have demonstrated that the near-surface fluctuations in the density of neutral defects on the oxidized Fe–Ni (FNS-5) alloy can be imaged with the aid of thermostimulated electron emission.

REFERENCES

1. B. I. Shklovskii and A. L. Efros, *Electronic Properties of Doped Semiconductors* (Nauka, Moscow, 1979; Springer-Verlag, New York, 1984).
2. W. Horsthemke and M. Malek Mansour, Z. Phys. B **24**, 397 (1976).
3. A. V. Druzhinin, Izv. Akad. Nauk SSSR, Ser. Fiz. **25**, 730 (1961).
4. V. A. Panteleev, S. N. Ershov, V. V. Chernyakhovskiĭ, and S. N. Nagornykh, Pis'ma Zh. Éksp. Teor. Fiz. **23**, 688 (1976) [JETP Lett. **23**, 633 (1976)].
5. U. Brunsmann and I. Scharmann, in *Proceedings of the 4th International Symposium on Exoelectron Emission and Dosimetry, Liblice, 1973*, pp. 137–141.
6. N. I. Lapin, S. N. Nagornykh, V. I. Pavlenkov, *et al.*, in *Proceedings of the 42nd International Conference on Modern Problems of Strength, Kaluga, 2004*, p. 105.
7. M. A. Krivoglaz, Usp. Fiz. Nauk **111**, 617 (1973) [Sov. Phys. Usp. **16**, 856 (1973)].
8. S. N. Nagornykh and V. I. Pavlenkov, Pis'ma Zh. Tekh. Fiz. **31** (4), 1 (2005) [Tech. Phys. Lett. **31**, 132 (2005)].

Translated by P. Pozdeev

Technical Physics Letters, Vol. 31, No. 7, 2005, pp. 603–604. Translated from Pis'ma v Zhurnal Tekhnicheskoĭ Fiziki, Vol. 31, No. 14, 2005, pp. 45–49.

Thermal Effects in Homogeneously Heated Samarium Sulfide Single Crystals

V. V. Kaminskiĭ* and S. M. Solov'ev

Ioffe Physicotechnical Institute, Russian Academy of Sciences, St. Petersburg, 194021 Russia

** e-mail: Vladimir.Kaminski@mail.ioffe.ru*

Revised manuscript received February 16, 2005

Abstract—In the course of thermal cycling, which involved heating to $T \sim 500$ K followed by cooling, samarium sulfide (SmS) single crystals exhibited sudden temperature drops with a magnitude of up to 125 K. This effect can be related to a semiconductor–metal phase transition characteristic of SmS. © *2005 Pleiades Publishing, Inc.*

In a previous study devoted to emf generation in samarium monosulfide (SmS) single crystals under conditions of homogeneous heating in the absence of external temperature gradients [1], we observed significant (up to 125 K) drops in the sample temperature, which accompanied the appearance of emf. This paper reports the results of a more thorough investigation into this phenomenon.

The experiments were performed on single crystal samples of SmS with dimensions ~2.5 × 2 × 1 mm, which were cut via the [100], [010], and [001] cleavage planes. The material had a resistivity of ρ = 0.02–0.03 Ω cm and a Hall conduction electron density of $n \sim 6 \times 10^{18}$ cm^{-3}. The experimental procedure was analogous to that described in [1]. The sample was heated in a container filled with a vacuum oil. The system design reliably eliminated the appearance of any external temperature gradients (and, hence, spurious emf components) in the course of heating. The sample temperature was monitored by two thermocouples, the junctions of which were fixed on the opposite edges of the sample. The signals from the thermocouples and the output voltage U of the SmS sample were fed via an analog-to-digital (ADC) converter into a personal computer, processed, and displayed at a temporal resolution of 0.1428 s.

The results of monitoring of the temperatures on both sample edges, their difference ΔT, and the output signal U are presented in the figure. In the course of heating to 387 K, the temperatures of both edges grow synchronously (curves *1* and *2* coincide), which is evidence of the absence of temperature gradients across the sample. Upon further heating, one of the sample edges exhibits drops (curve *2*) with a magnitude of up to ΔT = 125 K and a duration of up to 8 min. These temperature oscillations are terminated when the sample is cooled to T = 440 K on both ends (curves *1* and *2*, t = 77.5 min). At T < 440 K, the temperatures of both ends synchronously decrease.

One possible explanation of the observed thermal effects is based on the notion about the isostructural (NaCl–NaCl) first-order transition from semiconductor to metal phase, which is characteristic of SmS. This phase transition in SmS takes place under various mechanical actions, in particular, upon hydrostatic compression to ~650 MPa [2]. The mechanism of this phase transition is related to the screening of the electron potential of samarium ions by the conducting electrons, so that the phase transition onset corresponds to the critical density of these electrons. The conducting electrons are from 4*f* levels of samarium ions ($E_f \approx$ 0.23 eV, $N_f = 1.8 \times 10^{22}$ cm^{-3}) and the donor impurity levels ($E_i \approx 0.05$ eV, $N_i = (1–5) \times 10^{20}$ cm^{-3}), which cor-

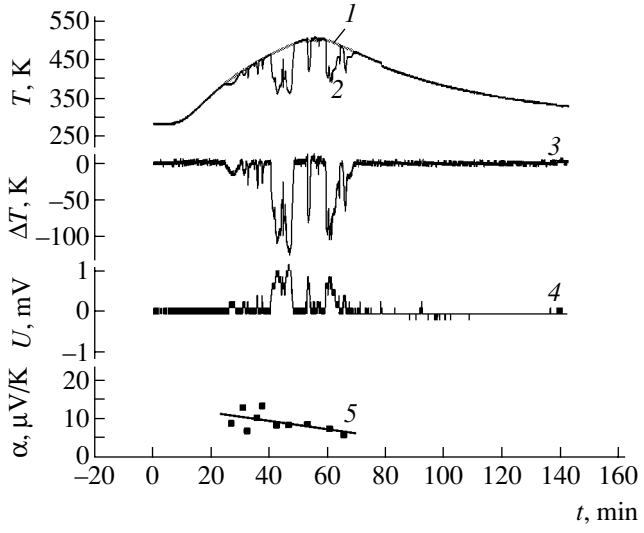

The dynamics of variation of (*1*, *2*) the temperature measured on the opposite edges of a sample, (*3*) the temperature difference between these edges, (*4*) the corresponding emf, and (*5*) the thermo emf in the course of heating and cooling of an SmS single crystal.

1063-7850/05/3107-0603$26.00 © 2005 Pleiades Publishing, Inc.

respond to the defect ions of Sm^{2+} occupying vacancies in the sulfur sublattice [3].

The pressure-induced phase transition proceeds in two stages: stage 1 features a jumplike increase in the concentration of conducting ions due to the activation from impurity levels ($Sm^{2+} \longrightarrow Sm^{3+} + e$), and stage 2 features an analogous change in the valence of samarium ions occurring at the crystal lattice sites, by means of electron activation from the 4*f* levels. Both these transitions (of the Mott type) are terminated by pushing-out the E_i and 4*f* levels to the conduction band. Note that stage 1 stimulates the realization of stage 2 by supplying a sufficiently large number of electrons to the conduction band [4].

Let us explain the observed thermal effect on a qualitative level, proceeding from the above model. Note that the concentration of defect samarium ions (N_i) in SmS in the general case is not the same in various parts of a sample. Apparently, this factor accounts for the observed difference in behavior of the opposite ends in the course of heating (N_i values on the two edges are not the same) and gives rise to temperature gradients.

According to [5], SmS crystals heated to $T > 450$ K transform into a high-temperature phase, which is characterized by the activation energy of conducting electrons $E_f = 0.18$ eV and the thermo emf $\alpha \sim 10$ μV/K. In contrast, the α value in the low-temperature phase is about ten times higher, and the activation energy of conducting electrons is 0.05 eV. From this we may infer that the high-temperature phase probably corresponds to such a state of SmS in which stage 1 of the phase transition is already terminated, while stage 2 has not yet started, since the pressure is absent and the 4*f* levels do not approach the conduction band bottom due to the baric shift.

According to [1], a transition to the high-temperature phase may begin already at $T > 375$ K. Thus, in the present study, the sample at $T > 387$ K might occur in the high-temperature state, since $\alpha = U/\Delta T$ calculated using the data corresponding to curves *3* and *4* is on the order of 10 μV/K (curve *5*). The validity of this calculation of α stems from the complete identity of the geometry of our present experiment and that used for the study of thermo emf. The peaks in curves *3* and *4* coincide on the time scale. The points on curve *5* were calculated using the peak values of *U* and Δ*T*.

As the temperature is increased further, conditions for the realization of stage 2 of the phase transition in SmS are created at one of the edges (curve *2*). Thermal fluctuations from 4*f* levels lead to the appearance of a critical density of conducting electrons that is sufficient to provide a strong screening of Sm^{2+} ions. As a result, all electrons on the 4*f* levels are delocalized to fall within the conduction band. However, this collective excitation is accompanied by a local decrease in the temperature, which leads to a decrease in the electron density below critical and to violation of the conditions necessary for the realization of stage 2. As a result, the final (metallic) state of the phase transition in SmS in the absence of external pressure cannot be stabilized. The magnitude of the temperature effect can be evaluated as follows. The energy absorbed for the collective excitation of 4*f* electrons to the conduction band must be on the order of $E_f N_f$. In the absence of heat exchange, this will correspond to a decrease in the temperature $\Delta T = E_f N_f / C$, where $C = 1.8$ J/(cm^3 K) is the specific heat capacity of semiconducting SmS [6]. This evaluation yields $\Delta T \sim 300$ K, which is quite consistent with the values found in experiment ($\Delta T \leq 125$ K), where the condition of zero heat exchange was not observed.

A decrease in the temperature of the whole sample, which begins at $T \sim 440$ K, corresponds to a transition of the sample to the low-temperature state described in [1]. The temperature jumps are no longer observed at $T < 440$ K, since the density of conducting electrons and, hence, the degree of screening of the Coulomb potential of samarium ions, are significantly reduced.

Thus, the observed phenomenon of temperature drops can be explained within the framework of the proposed model of the phase transition in SmS. A more thorough analysis of this phenomenon, as well as alternative explanations of the observed effects, based on the optical and X-ray diffraction data will be presented in subsequent publications.

Acknowledgments. The authors are grateful to A.V. Golubkov for kindly providing the SmS samples for investigation and to L.N. Vasil'ev, M.M. Kazanin, and I.A. Smirnov for fruitful discussions and useful remarks concerning this publication.

REFERENCES

1. V. V. Kaminskiĭ and S. M. Solov'ev, Fiz. Tverd. Tela (St. Petersburg) **43**, 423 (2001) [Phys. Solid State **43**, 439 (2001)].
2. I. A. Smirnov and V. S. Oskotskiĭ, Usp. Fiz. Nauk **124**, 241 (1978) [Sov. Phys. Usp. **21**, 117 (1978)].
3. V. V. Kaminskiĭ, A. V. Golubkov, and L. N. Vasil'ev, Fiz. Tverd. Tela (St. Petersburg) **44**, 1501 (2002) [Phys. Solid State **44**, 1574 (2002)].
4. V. V. Kaminskiĭ, V. A. Kapustin, and I. A. Smirnov, Fiz. Tverd. Tela (Leningrad) **22**, 3568 (1980) [Sov. Phys. Solid State **22**, 2091 (1980)].
5. M. M. Kazanin, V. V. Kaminskiĭ, and S. M. Solov'ev, Zh. Tekh. Fiz. **70** (5), 136 (2000) [Tech. Phys. **45**, 659 (2000)].
6. V. V. Kaminskiĭ, Fiz. Tverd. Tela (Leningrad) **20**, 1742 (1978) [Sov. Phys. Solid State **20**, 1008 (1978)].

Translated by P. Pozdeev

Technical Physics Letters, Vol. 31, No. 7, 2005, pp. 605–607. Translated from Pis'ma v Zhurnal Tekhnicheskoĭ Fiziki, Vol. 31, No. 14, 2005, pp. 50–56.

Magnetoresistance of $La_{0.67}Ca_{0.33}MnO_3$ Films Grown on Substrates with Orthorhombically Distorted Unit Cells

Yu. A. Boikov* and V. A. Danilov

Ioffe Physicotechnical Institute, Russian Academy of Sciences, St. Petersburg, 194021 Russia

** e-mail: yu.boikov@mail.ioffe.ru*

Received February 28, 2005

Abstract—We have studied the structure and magnetoresistance of 40-nm-thick epitaxial $La_{0.67}Ca_{0.33}MnO_3$ (LCMO) films grown by laser deposition on (001)-oriented $NdGaO_3$ (NGO) substrates. The manganite layers were oriented so that the *b* axis was perpendicular to the substrate plane and occurred under the action of inhomogeneous biaxial mechanical stresses. The negative magnetoresistance of the LCMO films in the vicinity of the ferromagnetic spin ordering was about 71% ($\mu_0 H = 1$ T). The observed azimuthal anisotropy of the magnetotransport properties of 40-nm-thick LCMO/(001)NGO films can be explained within the framework of a model of anisotropic magnetoresistance taking into account the presence of the preferred orientation of the spontaneous magnetization. © *2005 Pleiades Publishing, Inc.*

Introduction. Thin layers of perovskitelike manganites of the $La_{1-x}(Ca,Sr)_xMnO_3$ type are promising materials for magnetoresistive transducers and IR radiation sensors [1, 2]. The electron properties of such manganite films depend on their structure, composition (*x* value in the above formula), type and magnitude of mechanical stresses, etc. One of the main factors responsible for the elastically stressed state of a heteroepitaxial film is the tight contact between the film and a substrate made of a material with different crystal lattice parameters. Use of the substrates with a considerable mismatch *m* between the crystal lattice parameters usually leads [3] to depression of the temperature of ferromagnetic spin ordering in a thin manganite layer as compared to the value in bulk crystals. The effective lattice mismatch is defined as $m = (a_L - a_S)/a_S$, where a_L and a_S are the crystal lattice parameters of deposited layer and the substrate, respectively. Data available in the literature on the effect of azimuthally inhomogeneous mechanical stresses on the electro- and magnetotransport parameters of manganite films are rather fragmentary.

Experiment. We have studied the electric resistance and the magnetoresistance of thin $La_{0.67}Ca_{0.33}MnO_3$ (LCMO) manganite films grown by means of laser deposition (KrF, $\lambda = 248$ nm, $\tau = 30$ ns) on (001)-oriented $NdGaO_3$ (NGO) substrates. The technological parameters of the growth of LCMO/NGO films were reported in detail elsewhere [4]. Data on the film structure, orientation, and crystal lattice parameters in the lateral directions and along the normal to the substrate surface were obtained by X-ray diffraction ($CuK_{\alpha 1}$, $\omega/2\theta$ and ϕ scans; rocking curves). The dc resistance *R* of the LCMO films was measured in the van der Pauw geometry in the absence of magnetic field or in a magnetic field of $\mu_0 H = 0$–5 T. The magnetic field was oriented parallel to the substrate plane. The resistivity ρ was calculated as $\rho = \pi dR/\ln 2$ [5], where $d = 40$ nm is the manganite layer thickness. The film thickness *d* was determined from data on the width of the satellite Laue peaks present in the X-ray diffractograms.

Experimental results and discussion. Neodymium gallate (NGO) and LCMO have isomorphous structures and possess close temperature coefficients of linear expansion [6, 7]. The epitaxial growth of LCMO films (orthorhombic unit cell, $a_1 = 5.454$ Å, $b_1 = 7.704$ Å, $c_1 = 5.468$ Å [8]) is possible on NGO substrates (orthorhombic unit cell, $a_2 = 5.426$ Å, $b_2 = 5.502$ Å, $c_2 = 7.706$ Å [7]) with (001) and (110) orientations. The effective lattice mismatch between LCMO films and (001)NGO substrates is usually determined using the parameters of pseudocubic lattices of LCMO ($a_3 = 5.858$ Å [7]) and NGO ($a_4 = 3.851$ Å [8]), which yields $m \sim 0.2\%$. In order to determine the type and magnitude of mechanical stresses operating in a 40-nm-thick LCMO/NGO film, it is necessary to know the exact orientation of the film relative to the orthorhombically distorted substrate.

The obtained X-ray diffraction data ($\omega/2\theta$ and ϕ scans) showed that the 40-nm-thick LCMO/NGO films were free of secondary phase inclusions and had clear predominant orientations both in the substrate plane and in the normal direction. The X-ray diffractograms exhibited no reflections of complex structure indicative of the relaxation of mechanical stresses in the films. The peaks due to the manganite layer in the $\omega/2\theta$ scans obtained for the incident and reflected beams occurring in the plane perpendicular to the (001)NGO plane were observed only for the 2θ values correspond-

1063-7850/05/3107-0605$26.00

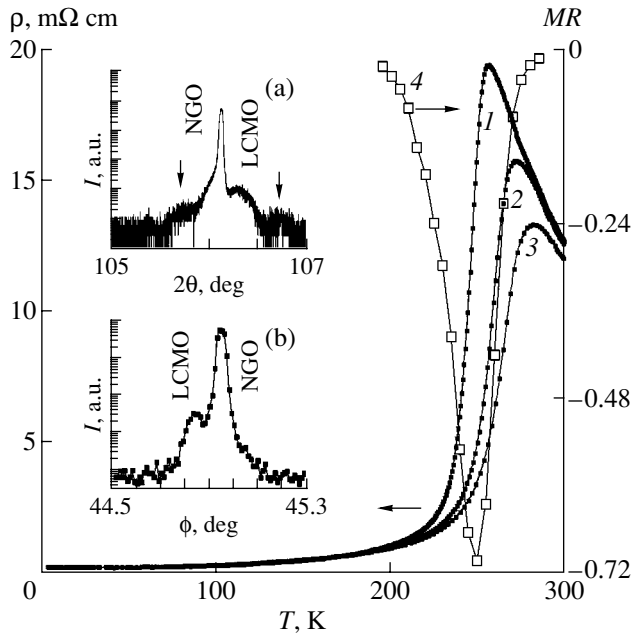

Fig. 1. Temperature dependences of the (*1*–*3*) resistivity ρ measured at $\mu_0 H = 0$ (*1*), 1 (*2*) and 2 T (*3*) and (*4*) magnetoresistance $MR = [\rho(\mu_0 H = 1\ \text{T}) - \rho(\mu_0 H = 0)]/\rho(\mu_0 H = 0)$ of a 40-nm-thick LCMO film grown on an (001)NGO substrate. The inset (a) shows a fragment of the ω/2θ X-ray diffractogram in the vicinity of the Bragg reflection for (008) NGO (arrows indicate the Laue satellite peaks due to the manganite film). The inset (b) shows a fragment of the ϕ scan for (111)LCMO and (111)NGO reflections (indices of pseudocubic lattices). A mutual shift of the peaks from manganite film and substrate is 0.1°.

ing to the crystal lattice parameter in the normal direction $a_\perp = 7.701 \pm 0.003$ Å.

The inset (a) in Fig. 1 shows a fragment of the X-ray diffractogram in the vicinity of the Bragg reflection from (008)NGO. The $a_\perp$ value virtually coincides with the parameter b_1 of the unit cell of LCMO, which indicates that the magnetic layers are *b*-oriented. This conclusion well agrees with the published results obtained by high-resolution electron microscopy [9]. Thus, the *m* value for the LCMO layer grown on (001)NGO depends on the matching of a_1 and c_1 values of the manganite film to the parameters of a flat lattice of the substrate plane. A comparison of the above values of a_1 and c_1 in LCMO and the a_2 and b_2 values in NGO shows that the minimum *m* values can be obtained only provided that the [100] and [001] directions in the manganite layer are parallel to the [100] and [010] directions in the substrate. In this case, the film will occur under the action of compressive mechanical stresses along the [100] direction (the mismatch between a_1 and a_2 is about 0.5%) and tensile stresses in the [001] direction (where the lattice mismatch is 0.6%).

In order to decrease the energy of elastic stresses in the film–substrate system, the unit cell parameter in the manganite layer in the [100] direction somewhat decreases, while that in the [001] direction somewhat increases (these parameters may not coincide with the corresponding NGO parameters; in addition, the unit cell in the film can be azimuthally rotated about a certain preferred direction in the substrate). This accommodation is manifested by a significant (~0.1°) relative shift of the peaks from the film and substrate in the ϕ scan (see inset (b) in Fig. 1). It should be noted that the "asymmetry" of mechanical stresses (compressive in one and tensile in the other direction) arising in the LCMO film as a result of the large orthorhombic distortion of the unit cell of NGO does not lead [4] to a change in the effective volume of the unit cell in the manganite film.

Figure 1 shows the temperature dependence of the resistivity ρ of a 40-nm-thick LCMO/NGO film measured in various magnetic fields. A sharp peak observed at $T_M = 255$ K well agrees with the data for bulk samples and the epitaxial LCMO films treated at high temperatures [10]. As the magnetic field intensity is increased, the resistivity decreases and the maximum of $\rho(T)$ shifts toward higher temperatures (Fig. 1). A peak in the magnetoresistance $MR = [\rho(\mu_0 H = 1\ \text{T}) - \rho(\mu_0 H = 0)]/\rho(\mu_0 H = 0)$ of 40-nm-thick LCMO/NGO films was observed at a temperature about 5 K below T_M. The negative MR(250 K) exceeded 70% (Fig. 1). At temperatures close to T_M, the magnetic field favors a growth of the ferromagnetic domains in the manganite layer (at the expense of the inclusions of paramagnetic and antiferromagnetic phases) and leads to a decrease in the spatial misorientation of spins of the manganese ions. A decrease in the temperature and an increase in *H* lead to an increase in the length and density of the highly conductive ferromagnetic "percolation channels" in the volume of the film, which results in the observed sharp drop in the resistivity.

Figure 2 shows the plots of ρ versus *H* for a 40-nm-thick LCMO/NGO film measured at $T = 92$ K using the probing current **I** perpendicular and parallel to the field **H** (the magnetic field in both cases is parallel to the Mn–O–Mn chains in the manganite layer). For $\mu_0 H < 0.12$ T, the resistivity increases with the magnetic field intensity for $\mathbf{H} \perp \mathbf{I}$, but decreases for $\mathbf{H} \parallel \mathbf{I}$ (Fig. 2). This behavior is indicative of a significant azimuthal anisotropy of the magnetoresistance in the 40-nm-thick LCMO/NGO films studied.

The dependence of the resistivity of ferromagnetic metals on the angle γ between the magnetization **M** and the electric current *I* can be described using the relation,

$$\rho = \rho_1(M) + \rho_2(M)\sin^2\gamma, \qquad (1)$$

where $\rho_1(M)$ is the isotropic component of the resistivity and $\rho_2(M)$ is the difference between the resistivities measured for $\mathbf{M} \parallel \mathbf{I}$ and $\mathbf{M} \perp \mathbf{I}$ (according to [11, 12], the difference $\rho_2(M)$ in ferromagnetic metals is negative, while that in LCMO is positive). The curves pre-

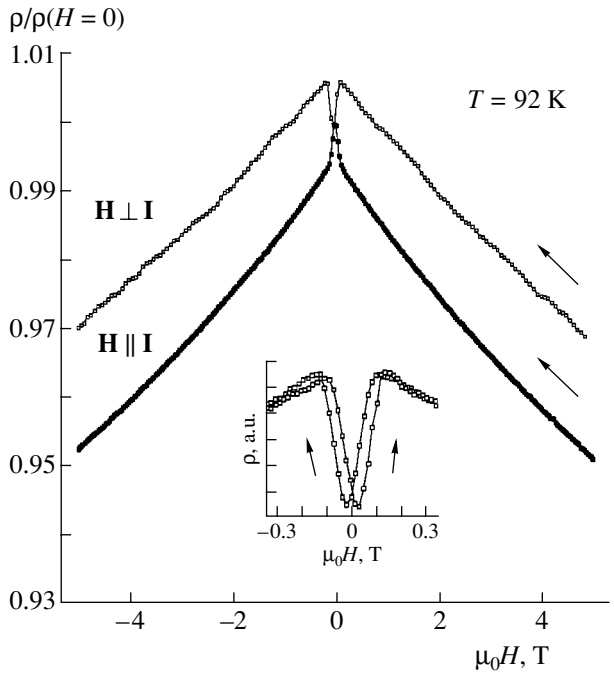

Fig. 2. Plots of the resistivity $\rho(H)/\rho(H = 0)$ versus magnetic field ($\mu_0 H$) for a 40-nm-thick LCMO/NGO film measured at $T = 92$ K using the probing current **I** perpendicular (**H** ⊥ **I**) and parallel (**H** ∥ **I**) to the magnetic field (the magnetic field in both cases is parallel to the Mn–O–Mn chains in the manganite layer). The inset shows fragments of the $\rho(H, T = 92\ \text{K})$ curves measured for H in the vicinity of zero (**H** ⊥ **I**).

sented in Fig. 2 qualitatively agree with relation (1), if we take into account that the direction of spontaneous magnetization in LCMO/NGO films is parallel to the diagonal between Mn–O–Mn chains [13]. Using the obtained $\rho(H)$ curves (see Fig. 2 and the inset to this figure), it was possible to evaluate the magnitude of the anisotropy field for a 40-nm-thick LCMO/NGO film as $\mu_0 H_K(92\ \text{K}) \approx 0.11$ T. Such an evaluation was hindered in [13] by a strong paramagnetic signal from a neodymium gallate substrate. As the temperature decreases, the $\mu_0 H_K$ value increases to reach ~0.2 T at 4.2 K. The $\rho(H)$ curves presented in the inset to Fig. 2 clearly reveal a hysteresis, which is indicative of a significant coercive field for the azimuthally rotated magnetic domains in 40-nm-thick LCMO/NGO films.

For $0.2\ \text{T} < \mu_0 H < 2$ T, the $\rho(H)$ value exhibits a decrease with increasing magnetic field. This behavior is explained by a decrease in the spatial misorientation of spins of manganese ions situated in the vicinity of small-angle grain boundaries and by a decrease in the electron–magnon interaction. It was demonstrated [4] that the manganite films consist of crystalline grains with lateral dimensions within 20–30 μm. For $\mu_0 H > 2$ T, the resistivity of the manganite film exhibits an almost linear decrease with increasing field, which is related to the absence of damping of the spin waves [4].

In conclusion, it is necessary to emphasize that the above analysis of mechanical stresses operative in the LCMO/NGO films shows that the observed predominant azimuthal orientation of magnetization may either have a magnetocrystalline nature (as was pointed out in [13]) and/or arise as a result of the inhomogeneous elastic deformation of the manganite layer by the substrate.

Acknowledgments. This study was supported in part by the Presidium of the Russian Academy of Sciences within the framework of the Program "Low-Dimensional Quantum Nanostructures" (project No. 9B19) and by the Russian Foundation for Basic Research (project no. 04-02-16212a).

REFERENCES

1. M. Pannetier, C. Fermon, G. Le Goff, *et al.*, Science **304**, 1648 (2004).
2. A. Goyal, M. Rajeswari, R. Shreekala, *et al.*, Appl. Phys. Lett. **71**, 2535 (1997).
3. Yu. A. Boikov, R. Gunnarsson, and T. Claeson, J. Appl. Phys. **96**, 435 (2004).
4. Yu. A. Boĭkov, V. A. Danilov, and A. Yu. Boĭkov, Fiz. Tverd. Tela (St. Petersburg) **45**, 649 (2003) [Phys. Solid State **45**, 681 (2003)].
5. T. I. Kamins, J. Appl. Phys. **42**, 4357 (1971).
6. M. Sasaura, S. Miyazawa, and M. Mukaida, J. Appl. Phys. **68**, 3643 (1990).
7. P. Dai, J. Zhang, H. A. Mook, *et al.*, Phys. Rev. B **54**, R3694 (1996).
8. R. W. G. Wyckoff, *Crystal Structures* (Interscience, New York, 1964), Vol. 2, p. 409.
9. O. I. Lebedev, G. Van Tendeloo, S. Amelinckx, *et al.*, Phys. Rev. B **58**, 8065 (1998).
10. Yu. A. Boĭkov, T. Klaeson, and A. Yu. Boĭkov, Zh. Tekh. Fiz. **71** (10), 54 (2001) [Tech. Phys. **46**, 1260 (2001)].
11. E. D. Dahlberg and K. Riggs, J. Appl. Phys. **63**, 4270 (1988).
12. J. O'Donnell, M. Onellion, M. S. Rzchowski, *et al.*, Phys. Rev. B **55**, 5873 (1997).
13. N. D. Mathur, M.-H. Jo, J. E. Evetts, and M. G. Blamire, J. Appl. Phys. **89**, 3388 (2001).
14. B. Raquet, M. Viret, E. Sondergard, *et al.*, Phys. Rev. B **66**, 024433 (2002).

Translated by P. Pozdeev

Technical Physics Letters, Vol. 31, No. 7, 2005, pp. 608–610. Translated from Pis'ma v Zhurnal Tekhnicheskoĭ Fiziki, Vol. 31, No. 14, 2005, pp. 57–61.

Calculating Parameters of High-Power He–Ne Lasers Operating at λ = 0.63 μm

V. V. Lipskii and V. E. Privalov

St. Petersburg State Technical University, St. Petersburg, 195251 Russia

Received December 28, 2004

Abstract—The existing methods of calculation of the parameters of He–Ne lasers agree with experiment for laser powers not exceeding 30–50 mW. We propose a method applicable to lasers operating at λ = 0.63 μm with a maximum output power exceeding 100 mW. © *2005 Pleiades Publishing, Inc.*

The demand for high-power He–Ne lasers is predicated upon their wide use in holography, Raman spectroscopy [1], and photodynamic therapy [2]. Using the available commercial lasers (such as LG-38, LGN-215, LGN-220, and LGN-222) it is possible to obtain an output power level of only about 80 mW on the fundamental TEM_{00q} mode, although it was reported that 108 mW was obtained with a folded cavity [3] and 320 mW was achieved in a multimode lasing regime [4]. However, the latter laser is not used in practice because of its large weight and size.

In this context, it is important to develop methods for estimating the lasing power, the beam diameter and divergence, and the stability of parameters for high-power He–Ne lasers operating in a single-mode regime. Previously, we reported [5] on calculation of the output power of an LGN-222 laser for five wavelengths in the red spectral range. It was found that the maximum power at λ = 0.63 μm is limited to a level of 84 mW.

In this study, as well as in [5], we use a formula for the laser power in the regime of weak signal amplification:

$$P = AG_m[1 - (a_s/G_m)^{1/2}]^2 \pi S_0^2[1 - \exp(-2r_0^2/S_0^2)], \quad (1)$$

where $A = 30$ W/cm^2 is the saturation coefficient, G_m is the total unsaturated amplification coefficient at the center of the Doppler-broadened contour for Ne atoms, a_s is the sum of losses, S_0 is the beam radius at the output mirror, and r_0 is the capillary radius.

As is known, the unsaturated amplification coefficient is given by the formula [6, 7]

$$G_m = 3 \times 10^{-4}(l/2r_0), \quad (2)$$

where l is the length of the active part of the capillary; the output beam radius is

$$S_0 = (\lambda L/\pi)^{1/2}[L(R-L)]^{1/4}, \quad (3)$$

where λ is the lasing wavelength, R is the radius of curvature of the planar-spherical cavity, and L is the cavity length.

The aim of this study was to assess the possibility of reaching a laser power level of $P_{las} \geq 100$ mW for a radiator size such as in LGN-222. According to formula (1), this can be achieved through an increase in G_m and S_0 and a decrease in a_c. In the case under consideration, the factor $[1 - \exp(-2r_0^2/S_0^2)]$ is close to unity. However, the S_0 value is limited from above by the reduced radius r_0 ensuring the necessary gain G_m in a single-mode regime, while the minimum losses in the cavity ($a_{c,min}$) are limited from below by dissipative losses. For this reason, we have assessed the possibility of increasing P_{las} at the expense of G_m increase by doubling the l value. In practice, this can be achieve using a folded Π-shaped cavity in the base radiator unit of LGN-222 [3].

In order to evaluate the level of losses (a_s), we took into account the absorption losses (a_1) in each Brewster window of parallel active elements, the losses (a_2) for reflection from cavity mirrors, the diffraction losses (a_3), and the auxiliary losses (a_4).

According to [7], the absorption losses per pass in two 2-mm-thick quartz windows are $a_{11} = 1.5 \times 10^{-3}$, which yields a total of $a_1 = 3 \times 10^{-3}$. The reflection losses in the cavity mirror manufactured by vacuum deposition of ZrO_2 and SiO_2 onto a quartz substrate can also be estimated as $a_{21} = 1.5 \times 10^{-3}$ [7], which yields for a cavity with two main and two rotating mirrors $a_2 = 6 \times 10^{-3}$.

The level of diffraction losses a_3 was evaluated by determining the Fresnel numbers for an equivalent con-

1063-7850/05/3107-0608$26.00

focal cavity [6]. These Fresnel numbers were calculated as

$$N_1 = a^2/(\lambda L)[g_1/g_2(1-g_1g_2)]^{1/2}, \quad (4a)$$

$$N_2 = a^2/(\lambda L)[g_2/g_1(1-g_1g_2)]^{1/2}, \quad (4b)$$

where a is the cavity aperture and g is the cavity parameter calculated as $g_i = 1 - L/R_i$ ($i = 1, 2$).

The N values were calculated for two cavity apertures determined by the capillary radii $r_{01} = 1.5$ mm and $r_{02} = 1.6$ mm, which were selected from the condition of lasing at the fundamental TEM_{00q} mode using the method described in [6]. The capillaries of active elements for LGN-215 and LGN-222 lasers are selected within these very limits. The results of these calculations are presented in Table 1.

The auxiliary losses were previously estimated as $a_4 = 1 \times 10^{-3}$ [7]. However, we adopted a double value, $a_4 = 2 \times 10^{-3}$, so as to take into account the additional active element and two rotating cavity mirrors. Thus, the total minimum losses are $a_s = 4.1 \times 10^{-2}$ for the cavity with $r_0 = 1.5$ mm and $a_s = 2.7 \times 10^{-2}$ for the cavity with $r_0 = 1.6$ mm.

The results of P_{las} calculations for the minimum and typical a_s values are summarized in Table 2. As can be seen from these data, the level of $P_{las} \geq 100$ mW can be achieved for $r_0 = 1.5$ mm with an increase in the losses up to $a_s = 6.0 \times 10^{-2}$, and, for $r_0 = 1.6$ mm, with the losses $a_s = 5.0 \times 10^{-2}$. The maximum level of P_{las} achieved for the minimum losses with $r_0 = 1.6$ mm is still higher.

The output laser beam radius calculated using formula (3) is $S_0 = 0.9$ mm. The laser beam divergence is given by the formula [6]

$$\Theta = 2/(kR)^{1/2} + 3.83/(ak), \quad (5)$$

where $k = 2\pi/\lambda$ is the wavenumber, a is radius of the cavity diaphragm, and $R = 2L(g_1/(1-g_2))^{1/2} = 9.7$ m is the confocal parameter. In this formula, the first term takes into account the divergence related to the cavity configuration, while the second term reflects the diffraction divergence arising at the aperture of the active element. In our case, $\Theta = 0.46$ mrad. It should be noted that the results of calculation using formula (5) virtually coincide with the value obtained using the formula from [8]: $\Theta = 1.27\lambda/(2S_0) = 0.45$ mrad.

The stability of the generation parameters can be evaluated by introducing a concept of the critical misalignment angle Ψ_c [9] at which the generation drops to zero. It was shown [10] that misalignment of the mirrors of a flat cavity by Ψ is equivalent to the introduction of additional losses

$$\alpha_{ad} \approx 3.3ka\Psi/(N_1)^{1/2}. \quad (6)$$

In the case under consideration, the cavity is almost flat ($R_1 = 10$ m; $R_2 = \infty$) and the permissible losses caused by misalignment can be evaluated as [6]

$$a_{ad} = 2G_m 1 - a_s, \quad (7)$$

where a_s are the losses of the completely aligned cavity.

Substituting formula (7) into relation (6), we can evaluate the critical misalignment angle for the total losses $a_s = 5 \times 10^{-2}$ as $\Psi_c = 0.015$ mrad; for the minimum losses, $a_s = 2.7 \times 10^{-2}$, we obtain $\Psi_c = 0.016$ mrad. These estimates of the critical misalignment angle are approximate and do not take into account the misalignment of rotating mirrors. The stability of the laser output power and the spatial (beam) characteristics depends both on the calculated Ψ_c value and on the features of laser design and should be determined in experiment.

In conclusion, it should be noted that the proposed approach is consistent with a quite general model of gas-discharge lasers [1].

Table 1

No.	r_0	N_1	N_2	$a_{31} \times 10^2$	$a_{32} \times 10^{-2}$	$a_3 \times 10^2$
1	1.5	0.73	0.46	1	5	3
2	1.6	0.83	0.52	0.2	3	1.6

Table 2

No.	$r_k = 1.5$ mm		$r_k = 1.6$ mm	
	$a_s \times 10^2$	P, mW	$a_s \times 10^2$	P, mW
1	4.1	133.2	2.7	151.1
2	5.0	118.9	3.0	142.4
3	6.0	105.5	4.0	122.9
4	7.0	93.8	5.0	106.9
5			6.0	94.3

REFERENCES

1. *Handbook of Optical Holography,* Ed. by H. J. Caulfield (Academic, New York, 1978), Vol. 2.

2. *Proceedings of the 11th Conference on Lasers for Medicine, Biology and Ecology, St. Petersburg, 2001*, Ed. by A. V. Ivashchenko and V. E. Privalov.
3. V. V. Lipskiĭ and V. E. Privalov, Opt. Spektrosk. **69**, 459 (1990) [Opt. Spectrosc. **69**, 274 (1990)].
4. W. Schenermann and G. J. Retter, Opt. Laser Technol. **2**, 45 (1971).
5. Y. M. Bondarchuk, D. S. Krysjuk, and V. V. Lipsky, Proc. SPIE **4316**, 104 (2000).
6. E. F. Ishchenko and Yu. M. Klimkov, *Optical Quantum Oscillators* (Sov. Radio, Moscow, 1968) [in Russian].
7. A. Mallik, in *Proceedings of the Symposium on Quantum Electronics and Optoelectronics, Bombay, 1974.*
8. D. C. O'Shea, W. R. Callen, and W. T. Rhodes, *Introduction to Lasers and Their Applications* (Addison Wesley, Reading, 1977).
9. D. C. Sinclair, Appl. Opt. **3**, 1067 (1964).
10. L. A. Vainshtein, *Open Cavities and Open Waveguides* (Sov. Radio, Moscow, 1976) [in Russian].
11. S. I. Mol'kov, Doctoral Dissertation (St. Petersburg State Technical University, St. Petersburg, 2004).

Translated by P. Pozdeev

Technical Physics Letters, Vol. 31, No. 7, 2005, pp. 611–612. Translated from Pis'ma v Zhurnal Tekhnicheskoĭ Fiziki, Vol. 31, No. 14, 2005, pp. 62–66.

Design and Technology of Monolithic GaAs *p–i–n* Diode Limiters for the Millimeter Wavelength Range

V. V. Volkov, V. P. Ivanova, Yu. S. Kuz'michev, and Yu. V. Solov'ev

"Svetlana–Elektronpribor" Corporation, St. Petersburg, Russia

Revised manuscript received February 14, 2005

Abstract—The design and production technology of monolithic planar GaAs *p–i–n* diode limiters for the microwave wavelength range are described. The limiter provides protection of receiving equipment in radar systems at an input signal power up to 100–200 W. The transmission losses do not exceed 1 dB, while the level of damping introduced in the limitation regime is 16–18 dB. © *2005 Pleiades Publishing, Inc.*

The input circuits of radar systems operating in the microwave wavelength range, based on planar lines of the microstrip, slot, and other types, are frequently protected from overloading with the aid of semiconductor limiter devices. The relatively small dimensions of such devices allow the task of increasing the switched power to be solved at the level of circuit design. The problem of further miniaturization of the semiconductor limiter devices is still important and can be solved, by analogy with the case of microwave semiconductor devices of certain other classes, by the passage to monolithic integrated devices, whereby all the active and passive elements and the transmission line segments are manufactured in a common technological cycle [1].

One of the main difficulties encountered in the development of high-power semiconductor devices intended for operation in a short-wave region of the millimeter wavelength range is related to the small transverse cross section of the waveguide, which implies the impossibility of arranging a large number of discrete elements in the microwave tract. A solution to this problem is offered by a complex approach to the design of such systems based on the use of monolithic integrated circuits representing an inseparable part of the waveguide tract. The implementation of solid state multidiode structures, comprising a window oriented across the waveguide, significantly simplifies the design and reduces the cost of semiconductor limiter devices [1–6].

This Letter describes the design and technology of monolithic GaAs *p–i–n* diodes, which can be used as the elements of limiter devices. The diodes are manufactured in the form of a monolithic planar array on a semiinsulating substrate and involve specially developed insulating "air bridges," which make it possible to reduce the active region of the limiter and to minimize the serial resistance and capacitance of the device.

The design of monolithic GaAs *p–i–n* diode limiters. The proposed device is a planar waveguide structure containing a "volume window" with an array of thin-base ($h_{n(i)} = 1$ μm) *p–i–n* diodes manufactured in a single technological cycle on a semiinsulating ⟨110⟩-oriented single crystal GaAs substrate and bounded by a gold beam lead over the base perimeter.

The multidiode matrix (Fig. 1) consists of two diode chains, each comprising eight serially connected diodes. The multidiode structure is self-controlled and requires no external bias voltage. The power dissipated in the diodes is removed via the gold beam lead to the case.

The technology of monolithic diode limiters. The epitaxial heterostructures were grown by metalorganic chemical vapor deposition (MOCVD) on semiinsulating GaAs substrates (commercial AGChP-8 grade). The epilayers had the following parameters (thickness and dopant concentration): p^+ layer, $h_p = 0.3$ μm, $N_{p^+} = (1–2) \times 10^{19}$ cm^{-3}; Be-doped base $n(i)$ layer, $h_{n(i)} = 1$ μm, $N_{n(i)} = 1 \times 10^{13}$ cm^{-3}; Si-doped buried n^+ layer, $h_{n^+} = 5$ μm, $N_{n^+} = 5 \times 10^{18}–1 \times 10^{19}$ cm^{-3}.

The ohmic contacts were obtained by metallization using vacuum thermal deposition, explosive photoli-

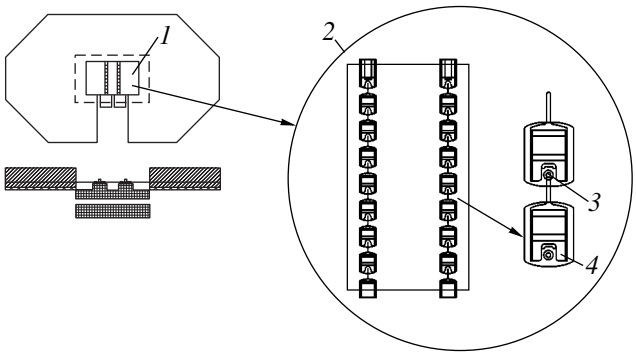

Fig. 1. Schematic diagram of a monolithic planar GaAs *p–i–n* diode limiter: (*1*) general view; (*2*) active region; (*3*) ohmic contact to p^+-GaAs epilayer; (*4*) ohmic contact to n^+-GaAs epilayer.

1063-7850/05/3107-0611$26.00 © 2005 Pleiades Publishing, Inc.

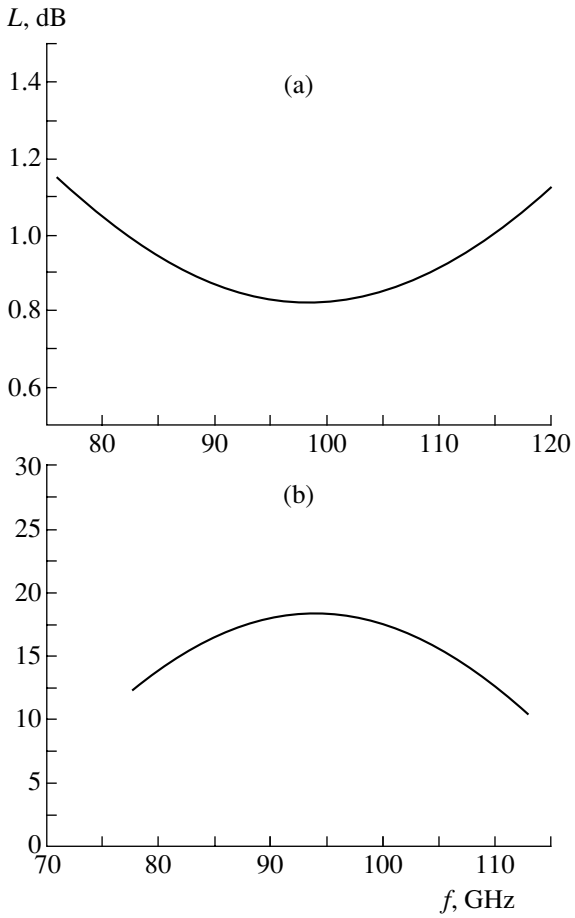

Fig. 2. The typical microwave characteristics of a monolithic planar GaAs *p–i–n* diode limiter: (a) transmission losses in the low-power operation regime; (b) damping losses in the high-power operation regime.

thography, and liquid-phase etching. A non-alloy Cr/Au contact was formed on the p^+ epilayer, and an AuGe–Ni–Au alloy contact was formed on the n^+ epilayer, after which the structure was annealed for 30 min in hydrogen at $T = 420$°C [7]. The mesa structure was obtained by etching in a peroxide–ammonia mixture down to the buried n^+ layer. The etching process was controlled by measuring the breakdown voltage between point probes on the epilayer surface. The *p* region was bounded by etching down the *n*(*i*) layer. The electrical characteristics of the obtained ohmic contacts were monitored in the course of diode fabrication using the long line technique. The resistivity of the Cr/Au ohmic contacts was $\rho_c^{Cr/Au} = (2–4) \times 10^{-6}\ \Omega\ cm^2$ and that of the AuGe–Ni–Au contact was $(1–2) \times 10^{-6}\ \Omega\ cm^2$.

The device structure was protected by the plasma-chemical deposition of a silicon dioxide layer, followed by opening windows for contact pads. The integral output contact of the diode limiter was obtained through Cr/Au metallization, followed by the galvanic deposition of a gold layer. The serial resistance and zero-bias capacitance of the diode limiter were measured in the working frequency range. Finally, the wafers were thinned to 30–40 μm by means of chemicodynamic polishing, and then separated into chips by chemical etching upon rear-side photolithography.

Results and discussion. The serial resistance of the diode chain at a working current of $I = 10$ mA was $R = 31–33\ \Omega$; the breakdown voltage was $U_{dis} = 180–200$ V ($I = 10$ μA); and the zero-bias capacitance was $C^{(0)} = 0.002–0.003$ pF. The proposed technology provides for a high homogeneity of the device parameters, which is an especially important factor for semiconductor limiter devices.

The obtained monolithic GaAs *p–i–n* diode limiter ensured reliable operation in the $f = 92–94$ GHz frequency range ($\lambda = 3$ mm) at a high level of pulse power (100–200 W). The transmission losses did not exceed 1 dB (Fig. 2a) and the damping introduced in the limitation regime was within 15–18 dB (Fig. 2b).

To summarize, we have developed the design and production technology of monolithic planar GaAs *p–i–n* diode limiters. The proposed technology provides for a high homogeneity of the device parameters and ensures a high useful yield. The device parameters for operation at a high input power level meet all requirements to the elements of protective semiconductor devices for microwave systems operating in the millimeter wavelength range.

REFERENCES

1. A. M. Ropiĭ, A. M. Starik, and K. K. Shutov, *Microwave Protection Devices* (Radio i Svyaz', Moscow, 1993) [in Russian].
2. C. V. Koshevaya, Ya. I. Kishenko, and M. I. Smoilovskiĭ, Izv. Vyssh. Uchebn. Zaved., Radioélektron. **32** (10), 56 (1989).
3. E. Alekseev, D. Pavlidis, V. Ziegler, *et al.*, in *Proceedings of the 20th IEEE GaAs IC Symposium, Atlanta, 1998*, pp. 177–180.
4. A. Armstrong and Y. Anand, IEEE Trans. **31**, 238 (1983).
5. J. Putnam, M. Fukuda, P. Staecker, and Y.-N. Yun, in *Proceedings of the 16th IEEE GaAs IC Symposium, 1994*, pp. 333–336.
6. E. Alekseev, D. Pavlidis, J. Dickmann, and T. Hackbarth, in *Proceedings of the 18th IEEE GaAs IC Symposium, Orlando, 1996*, pp. 285–288.
7. V. V. Volkov, N. A. Maleev, and V. M. Ustinov, Fiz. Tekh. Poluprovodn. (St. Petersburg) **33**, 346 (1999) [Semiconductors **33**, 345 (1999)].

Translated by P. Pozdeev

Technical Physics Letters, Vol. 31, No. 7, 2005, pp. 613–615. Translated from Pis'ma v Zhurnal Tekhnicheskoĭ Fiziki, Vol. 31, No. 14, 2005, pp. 67–72.

Experimental Investigation of the Current-Induced Breakage of Metal-Coated Polymer Films

P. N. Bondarenko and O. A. Emel'yanov*

St. Petersburg State Technical University, St. Petersburg, Russia

** e-mail: oae2@mail.wplus.net*

Received March 11, 2005

Abstract—We have experimentally studied the phenomenon of current-induced breakage of thin (~20- to 30-nm-thick) metal films deposited onto poly(ethylene terephthalate) (PETP) and poly(propylene) (PP) substrates. Two mechanisms leading to the current-induced breakage of the metal film are established, which are characterized by different average threshold current densities: $j_H \sim 1.5 \times 10^{10}$ A/m^2 and $j_L \sim 0.7 \times 10^{10}$ A/m^2. The possible nature of these mechanisms is discussed. © *2005 Pleiades Publishing, Inc.*

In evaluating the ultimate characteristics of modern capacitive energy storages, it is necessary to take into account certain physical limitations imposed on the rate of discharge of the high-voltage capacitors employed in such devices. The rate of energy transfer to a load, $\partial W_{\text{eff}}/\partial t$, is determined, on the one hand, by the characteristics of polarization processes and by the electric field strength in a working insulator. Some general relationships for these factors were recently obtained within the framework of the electrodynamics of continuum [1, 2]. On the other hand, the maximum discharge current, $I_{\max} \sim \partial W_{\text{eff}}/\partial t$, is also limited by the stability of plates of the high-voltage capacitors. It is commonly accepted that a decrease in the properties of such capacitors is related to the Joule-heating-induced electrothermal degradation of plates, which is developed primarily at the sites of considerable inhomogeneity of the electric field, such as the plate edges and contact zones.

For relatively thick electrode systems, with a characteristic plate thickness on the order of several units or tens of microns, the laws of such degradation are well known and are taken into account in the design of pulse capacitors [3]. At the same time, many of the modern metal-film capacitors (MFCs) employ metal-coated insulators, in which the thickness of a deposited metallization (zinc, aluminum) layer is on the order of several tens of nanometers, which provides for the self-recovery of the capacitor upon a breakdown of the working insulator. However, the working current densities in such MFCs are significantly increased (up to 10^7–10^9 A/m^2). Theoretically, this makes possible the influence of mechanisms related to the electrodynamic and thermoelastic phenomena in thin metal-coated electrodes. Such phenomena were briefly mentioned in [4, 5]. It is also possible that the metallization layers can be broken by a mechanism analogous to the mechanism of metal film breakage in integrated circuits, which is related to the electromigration of vacancies [6]. The passage of high-density currents may change the structure of a microrelief of thin metal films as a result of the formation and orientation of nanodefects. Recently, such nontrivial effects were realized and studied in [7, 8].

The stability of metallization layers apparently also significantly depends on the state of the polymer–metal interface. In particular, the adhesion of a metal layer to the polymer substrate eventually determines the thermal and mechanical stability of this interface and the mechanical strength of the film [9]. It should also be noted that an important role in the breakage of metal films on polymer substrates can be played by the highly specific spatial effects related to the thermodynamics of the process of continuity violation [10]. Unfortunately, published data concerning thin metallization layers on polymer films employed in MFCs are very limited. The lack of detailed information about the mechanisms of current-induced breakage of thin metallization layers on polymer films has inspired us to perform the corresponding experimental and theoretical investigations.

This Letter presents experimental data on the current-induced breakage of thin (~20–30 nm) aluminum and zinc metallization layers obtained by thermal deposition in vacuum onto 10-μm-thick poly(ethylene terephthalate) (PETP) and poly(propylene) (PP) substrates, respectively. The samples had the shape of curved stripes (Fig. 1a) cut from metal-coated polymer films. A test voltage from a pulse generator was applied to rectangular polished steel electrodes *1* and *2* pressed to a horizontal sample. The central region of each sample contained an artificial defect *3* in the form of a transverse ~100-μm-wide band (scratch) deprived of the metal coating. The presence of this defect led to an additional increase in the current density at the sample edge and allowed us to trace the dynamics of metallization breakage depending on the applied test voltage (current).

1063-7850/05/3107-0613$26.00

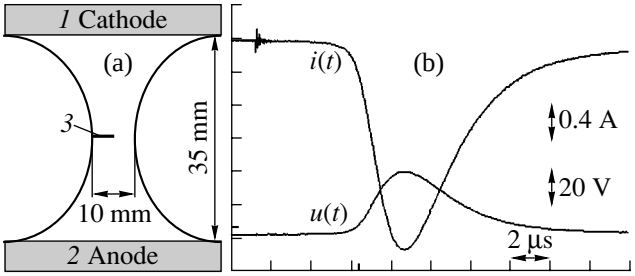

Fig. 1. (a) Schematic diagram of the sample and (b) typical oscillograms of voltage and current in a sample.

Figure 1b shows the typical oscillograms of the voltage and current pulses in a sample. For a voltage pulse amplitude of $U_m \geq 30$ V, we observed a crack originating at the artificial defect and propagating across the current lines. Evaluation of the corresponding average current density in a sample with aluminum metallization gave $j_H \sim 1.5 \times 10^{10}$ A/m^2. Each pulse (e.g., at $U_m \approx 32$ V) resulted in additional propagation of the crack, which traveled over a characteristic distance of ~100 μm. This transverse propagation of the crack eventually resulted in the complete breakage of the sample neck (Fig. 2a). This mechanism of breakage is probably related to a significant Joule heat evolution at the crack apex. It is possible that the electrodynamic and thermoelastic effects also influence the process of metal film breakage in this system.

It was expected that a decrease in the voltage pulse amplitude to a certain threshold U_H would result in the arrest of crack propagation. However, the experiments at $U_m \approx 25$ V revealed an unusual behavior, whereby the crack did not cease to grow but only decreased in the transverse size, changed the propagation direction at a right angle, and kept moving toward the positive electrode. Figure 2b clearly demonstrates this behavior for

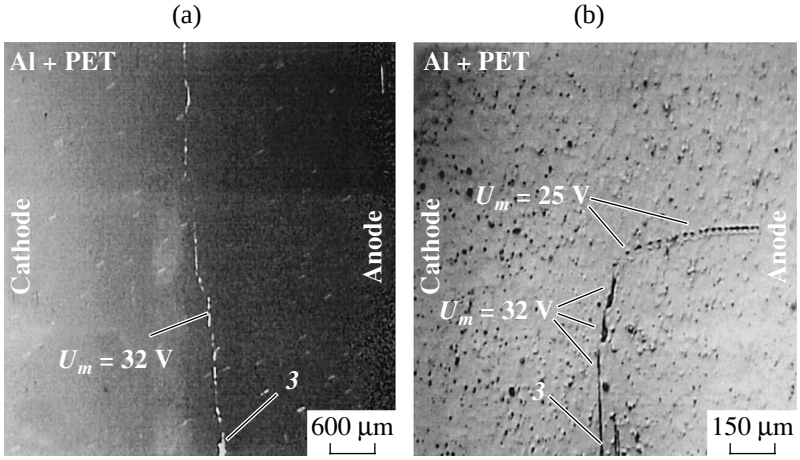

Fig. 2. Micrographs showing (a) the growth of a transverse crack and (b) the formation of a longitudinal crack in a thin aluminum layer on PETP substrate.

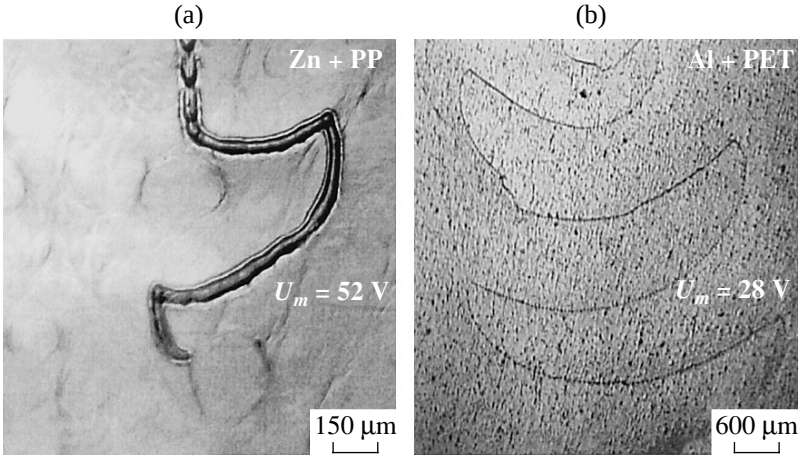

Fig. 3. Micrographs showing the patterns of crack oscillation caused by alternation of the electrode polarity for (a) Zn/PP and (b) Al/PETP systems.

the Al/PETP system, showing the initial transverse crack growth (three voltage pulses at $U_m \approx 32$ V) and the subsequent crack rotation (20 pulses at $U_m \approx 25$ V). When the pulse amplitude was reduced to $U_L \approx 15$ V, the crack ceased to grow. In this case, the average current density in the sample was $j_L \sim 0.7 \times 10^{10}$ A/m^2. Analogous experimental results were obtained for a zinc metallization on PP (Fig. 3a).

The polar mechanism of crack propagation toward the anode exhibits a stable character. This is illustrated by Fig. 3b, which shows a pattern of the oscillatory dynamics of crack growth in the Al/PETP system with periodic alternation of the polarity of voltage applied to the electrodes. Probably, this mechanism is related to the interaction of the flow of conduction electrons with defects (vacancies) in the crystal lattice of aluminum. This very mechanism is responsible for the electromigration processes in thin metal films and in the phenomenon of electroplastic deformation [6, 11]. In any case, the analysis of mechanisms responsible for the metal film breakage must take into account the role of the polymer–metal interface.

Thus, we have experimentally established that the breakage of thin metal films under the action of moderate current densities (~10^{10} A/m^2) can proceed according to two different mechanisms of the material degradation. These mechanisms are characterized by different threshold current densities and different directions of propagation of the breaking crack. Detailed analysis of these mechanisms requires separate consideration.

REFERENCES

1. O. A. Emel'yanov, Pis'ma Zh. Tekh. Fiz. **30** (19), 40 (2004) [Tech. Phys. Lett. **30**, 817 (2004)].
2. O. A. Emel'yanov, Zh. Tekh. Fiz. **75** (5), 131 (2005) [Tech. Phys. **50**, 660 (2005)].
3. G. S. Kuchinskiĭ and N. I. Nazarov, *Heavy-Duty Electric Capacitors* (Énergoatomizdat, Moscow, 1992) [in Russian].
4. F. Lin, X. Dai, and Z. Yao, IEEE Trans. Magn. **39**, 353 (2003).
5. X. Qi and S. Boggs, J. Appl. Phys. **94**, 4449 (2003).
6. J. R. Lloyd, J. Phys. D: Appl. Phys. **32**, R109 (1999).
7. V. I. Vettegren', V. L. Gilyarov, S. N. Rakhimov, and V. N. Svetlov, Fiz. Tverd. Tela (St. Petersburg) **40**, 668 (1998) [Phys. Solid State **40**, 614 (1998)].
8. I. P. Shcherbakov, D. V. Churaev, and V. N. Svetlov, Zh. Tekh. Fiz. **74** (4), 139 (2004) [Tech. Phys. **49**, 516 (2004)].
9. O. F. Pozdnyakov, A. O. Pozdnyakov, and V. R. Regel', Fiz. Tverd. Tela (St. Petersburg) **47**, 924 (2005) [Phys. Solid State **47**, 954 (2005)].
10. V. I. Vettegren', E. A. Bakulin, and Yu. V. Kovalenko, Fiz. Tverd. Tela (St. Petersburg) **44**, 765 (2002) [Phys. Solid State **44**, 796 (2002)].
11. V. I. Spitsyn and O. A. Troitskiĭ, *Electroplastic Deformation of Metals* (Nauka, Moscow, 1985) [in Russian].

Translated by P. Pozdeev

Technical Physics Letters, Vol. 31, No. 7, 2005, pp. 616–618. Translated from Pis'ma v Zhurnal Tekhnicheskoĭ Fiziki, Vol. 31, No. 14, 2005, pp. 73–76.

The December 26, 2004 Earthquake in the Indian Ocean and Geodynamic Perturbations in Novosibirsk

P. P. Belousov, P. Ya. Belousov, and Yu. N. Dubnishchev*

Institute of Thermal Physics, Siberian Division, Russian Academy of Sciences, Novosibirsk, Russia

** e-mail: dubnistchev@itp.nsc.ru*

Received February 28, 2005

Abstract—Some results from the monitoring of the geodynamic perturbations in Novosibirsk are considered in relation to the December 26, 2004 earthquake in the Indian Ocean, which gave rise to the catastrophic sea wave. © *2005 Pleiades Publishing, Inc.*

Within the framework of investigations devoted to the development of methods for predicting earthquakes, new techniques for monitoring oscillations of the Earth's surface have been developed at the Institute of Thermal Physics (Novosibirsk) [1]. The arrangement of the Novosibirsk observation station relative to the epicenter of the December 26, 2004 earthquake is shown on a map in Fig. 1a. The Novosibirsk station, having the coordinates (54°51.2′N, 0.83°06.5′E; el, 136 m), is located at a distance of 5837 km from the epicenter. Figures 1b and 1c show the earthquake region on different scales. Our equipment monitored the radial component of oscillations of the Earth's surface.

Figure 2 presents a fragment of the record illustrating (in relative units) the dynamics of the radial compo-

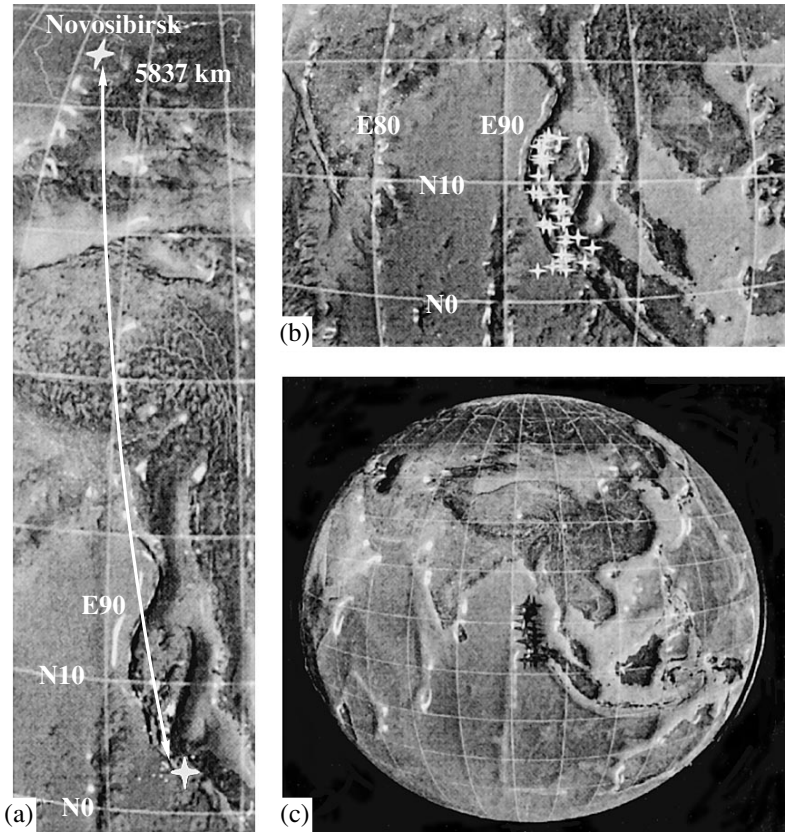

Fig. 1. Maps showing (1a) the geographic location of the Novosibirsk station relative to the epicenter of the December 26, 2004 earthquake and (1b, 1c) the earthquake region on different scales.

1063-7850/05/3107-0616$26.00 © 2005 Pleiades Publishing, Inc.

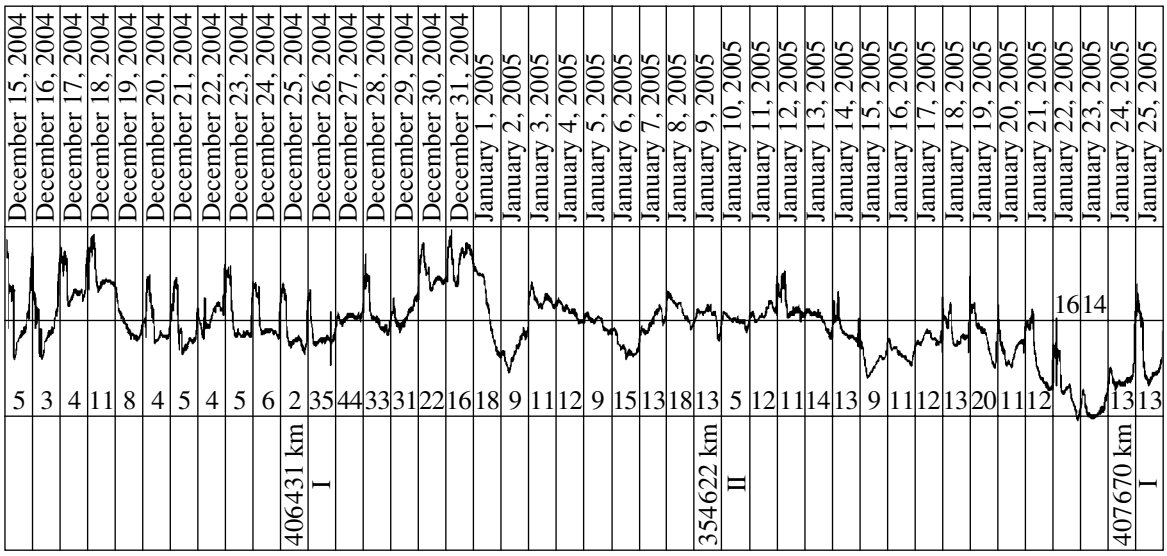

Fig. 2. Time series of the radial component of oscillations of the Earth's surface monitored at the Novosibirsk station. The upper scale indicates the time (1 day/div); figures under the curve indicate the number of earthquakes (rated ≥ 4) over this day; the bottom scale indicates Moon phases and the corresponding Moon–Earth distance (I, full Moon; II, new Moon).

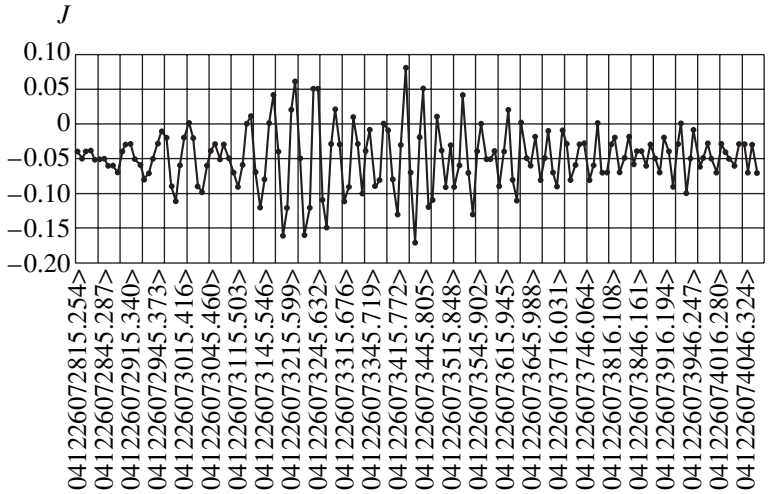

Fig. 3. A fragment of the time series in Fig. 2, depicted on a greater scale, showing the radial component of oscillations of the Earth's surface monitored at the Novosibirsk station, which were caused by the geodynamic perturbation related to the December 26, 2004 earthquake in the Indian Ocean (*J* is the amplitude, rel. units; *t* is the date and time (GMT + 6 h)).

nent of the Earth's surface in the period from December 14, 2004 to January 25, 2005. An arrow indicates the perturbation related to the December 26, 2004 earthquake. Figure 3 shows this dynamic perturbation on a greater scale. The detected signal represents a wave train lasting about 20 min, with a period of oscillations varying from ≈40 s (in the beginning) to ≈20 s (at the end). The signal was detected at Novosibirsk at 7 h 28 min (GMT). The distance (5837 km) from the epicenter was traveled by the perturbation for 29.53 min. The shape of the wave train and its frequency spectrum are probably determined by the dispersion properties of the medium in which the signal was transmitted.

As can be seen from Fig. 2, the signal due to the earthquake proper was preceded by intense radial displacements of the Earth's crust, which were manifested by a sequence of periodic pulses. The period of this sequence is equal to one day, while the average duration of pulsed perturbations amounted approximately to one quarter of a day. The nature of these periodic pulsed perturbations is determined by the diurnal lunar–solar action [2]. The earthquake took place at full Moon (December 26, 2004, 21 h 06 min), that is, when the lunar–solar action was at its maximum (spring tide).

Figure 2 also shows that, after the earthquake, the tidal deformations of the Earth's surface are superim-

posed with low-frequency aperiodic perturbations. On this background, the tidal dynamics becomes less pronounced. As was pointed out in the mass media, no significant seismic activity in this region of the Indian Ocean was registered for a rather long period of time. The radial displacements of the Earth's surface with a diurnal cycle, observed over a time interval preceding the perturbation due to earthquake, have proved to be much stronger than the displacements with a semidiurnal cycle. An analysis of the records of radial oscillations of the Earth's surface shows that geodynamic activity in the form of earthquakes is correlated with the lunar cycle.

REFERENCES

1. P. P. Belousov, P. Ya. Belousov, and Yu. N. Dubnishchev, *Optical Methods for Diagnosis of Flows* (Siberian University Publishers, Novosibirsk, 2003) [in Russian].
2. *Free Oscillations of Earth*, Ed. by V. N. Zharkov (Mir, Moscow, 1964) [in Russian].

Translated by P. Pozdeev

Technical Physics Letters, Vol. 31, No. 7, 2005, pp. 619–621. Translated from Pis'ma v Zhurnal Tekhnicheskoĭ Fiziki, Vol. 31, No. 14, 2005, pp. 77–82.

Fractal Structures Formed in Metals Irradiated by Ion and Laser Beams

V. S. Khmelevskaya, N. V. Kulikova, and V. V. Bondarenko

Obninsk State Technical University of Nuclear Power Engineering, Obninsk, Russia

Revised manuscript received March 18, 2005

Abstract—The state of the surface of various metal alloys upon irradiation with ion and laser beams has been studied. At a high level of radiation damage, structural elements formed on the metal surface exhibit spatial self-organization. These surface elements can be considered as fractal structures, with the fractal dimension dependent both on the parameters of external action and the properties of metal targets. © *2005 Pleiades Publishing, Inc.*

We have reported [1–3] that the action of ion and laser beams on metallic materials (pure metals and solid solutions) under certain conditions (radiation dose, target temperature, beam intensity) leads to the development of instability in subsurface layers of the targets, which results in the formation of structures showing evidence of spatial self-organization. Such structures are known to be characteristic of the open systems treated in the nonlinear region at a supercritical intensity of external action [4, 5], in particular, at a sufficiently high level of radiation damage. Previously, the radiation-induced states in metals upon ion irradiation were studied in detail for 40 metals [2, 6] and it was established that these states are nonequilibrium, since the related changes in the structure and properties disappeared in the course of postradiation annealing at temperatures not exceeding the target temperature in the course of irradiation.

Figures 1–3 show the examples of typical self-organized structures. The spatial structures presented in Fig. 1 were revealed by methods of optical metallography on the surface of a Fe–Cr alloy irradiated in a Vita accelerator setup with 30-keV Ar^+ ions to a total dose of 1×10^{18} cm^{-2} at a target temperature of 500°C. Figures 1a and 1b correspond to two grains of the given polycrystalline material, which have different crystallographic orientations.

Figures 2a and 2b show different grains of a polycrystalline V–4Cr–4Ti alloy irradiated with 30-keV

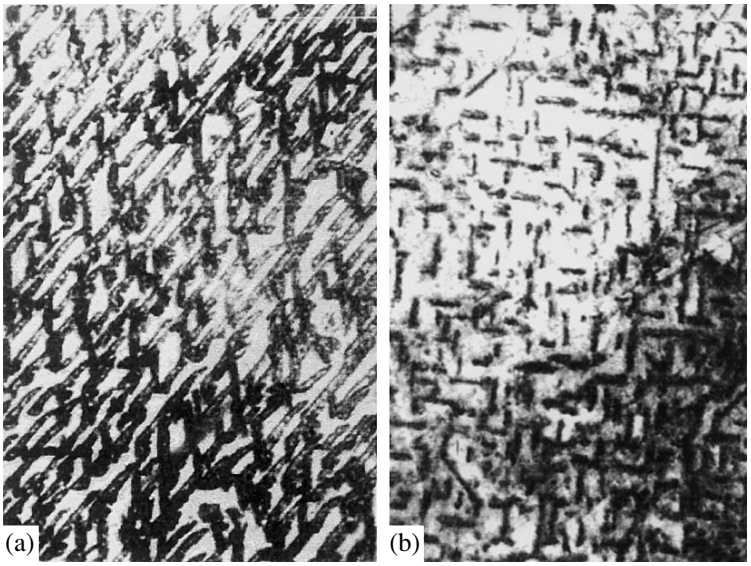

Fig. 1. Spatially self-organized structure formed in a polycrystalline alloy of the Fe–Cr system irradiated with 30-keV Ar^+ ions at a target temperature of 500°C. Patterns (a) and (b) refer to grains with different crystallographic orientations denoted I and II, respectively, in the table.

1063-7850/05/3107-0619$26.00 © 2005 Pleiades Publishing, Inc.

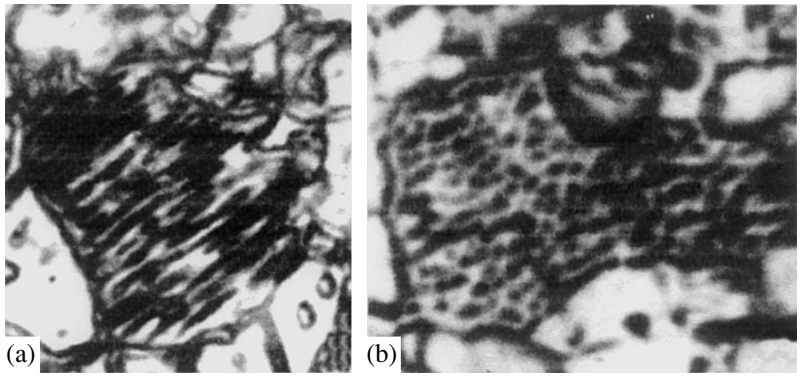

Fig. 2. Spatially self-organized structure formed in a polycrystalline V–4Cr–4Ti alloy irradiated with 30-keV Ar^+ ions at a target temperature of 700°C. Patterns (a) and (b) refer to grains with different crystallographic orientations denoted I and II, respectively, in the table.

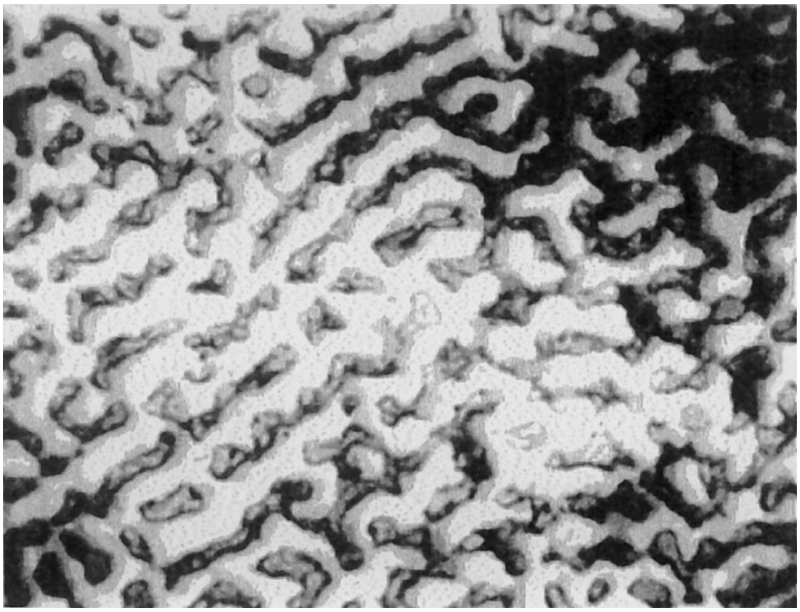

Fig. 3. Spatially self-organized structure formed in a Fe–18Cr–10Ni–Ti alloy exposed to 150 laser pulses.

Ar^+ ions to a total dose of 1.5×10^{18} cm^{-2} at a target temperature of 700°C.

Figure 3 presents an image of the surface of a sample of Fe–18Cr–10Ni–Ti alloy (fcc lattice) exposed to a solid-state pulsed YAG:Nd laser (LTI-406 type) operating at a wavelength of 1.06 μm and a pulse width of 10–20 ns.

The structures presented in Figs. 1–3 are self-similar on various spatial scales and can be considered as fractals [7]. We have attempted to apply the conventional methods of fractal analysis [7, 8] to the quantitative description of the observed spatial self-organization and the establishment of relations between the quantitative characteristics of observed fractal structures and the parameters of external action.

The methods of fractal analysis have been successfully used in materials science (see, e.g., [9, 10]). However, these methods were applied predominantly to the analysis of grain or porous structure of various materials. In this Letter, we present the results of fractal analysis of the spatially self-organized structures observed for the first time in ion-irradiated metals and the heterophase structures formed under the laser action.

The fractal analysis was performed by applying methods of computer simulation to the digitized images of structures presented in Figs. 1 and 2. The images were treated as the realization of a spatial stochastic process defined in a certain domain with dimensionality 2 [7, 9, 11]. The images were analyzed using continuous rectangular limitation, which provides for the most illustrative representation of self-organization

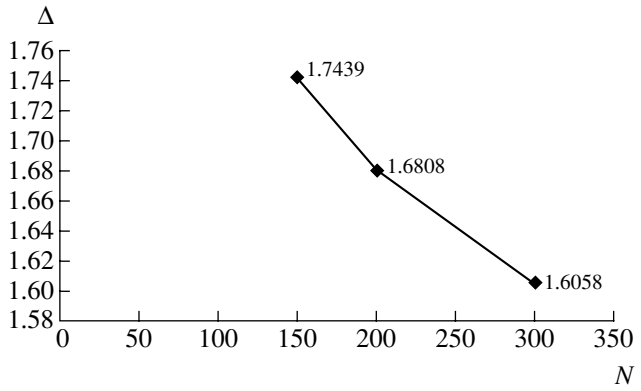

Fig. 4. A plot of the fractal dimension Δ of a fractal structure formed in a Fe–18Cr–10Ni–Ti alloy versus number *N* of laser pulses.

processes. If the object under consideration exhibits self-similarity, it can be quantitatively characterized in terms of the fractal dimension [7–9, 11]. In the course of computer analysis, the sample image is represented as a sequence of matrices obtained by subdividing the photographic image with square lattices composed of identical cells with gradually decreasing dimensions [7, 8]. The discretization is achieved by assigning a given cell unity, if the block covered by this cell contains a dark spot, and by assigning it zero otherwise [12]. The size of the cells covering the image for obtaining the first approximating matrix is selected so as to be comparable with the size of elements in the given structure.

The results of our analysis showed that the selected quantitative characteristic (fractal dimension) of self-organized structures is correlated with the parameters of external action. Figure 4 shows a plot of the fractal dimension Δ of a fractal structure formed in a Fe–18Cr–10Ni–Ti alloy versus number *N* of laser pulses. As can be seen, the fractal dimension monotonically decreases so that the Δ values for 150 and 300 laser pulses differ by 9%.

Fractal dimensions of self-organized structures formed in different grains of ion-irradiated polycrystalline alloys

Material	Crystal lattice	Target temperature, °C	Crystal orientation (conditional)	Fractal dimension
Fe–12Cr–Mo–W–V–Nb	bcc	500	I	1.7754
Fe–12Cr–Mo–W–V–Nb	bcc	500	II	1.849
V–4Cr–4Ti	bcc	700	I	1.7292
V–4Cr–4Ti	bcc	700	II	1.8017

Figures 1 and 2 present the digital images of fractal structures observed upon laser irradiation on the surface of bcc alloys of the Fe–Cr and V–Cr–Ti systems. In both cases, the two images refer to different grains with unlike (and unknown) crystallographic orientations (denoted by I and II in the table). As can be seen, the structures are visibly distinguishable and possess different fractal dimensions (see table).

In conclusion, we can ascertain that the fractal dimension as a quantitative characteristic of a self-organized structure is sensitive to both the parameters of external action and the internal properties of irradiated materials. The problem is undoubtedly worth further investigation, but it is already evident that fractal analysis may be very useful in the investigation of substances in substantially nonequilibrium states.

REFERENCES

1. V. S. Khmelevskay and V. G. Malynkin, Phase Transit. **60**, 59 (1997).
2. V. S. Khmelevskaya and V. G. Malynkin, Materialovedenie, No. 2, 25 (1998).
3. V. S. Khmelevskaya, V. G. Malynkin, and E. V. Bazaleev, Pis'ma Zh. Tekh. Fiz. **20** (23), 21 (1994) [Tech. Phys. Lett. **20**, 633 (1994)].
4. G. Nicolis and I. Prigogine, *Self-Organization in Non-Equilibrium Systems* (Wiley, New York, 1977).
5. H. Haken, *Synergetics: an Introduction* (Springer-Verlag, Berlin, 1977; Mir, Moscow, 1980).
6. V. S. Khmelevskay, S. P. Solovyev, and V. G. Malynkin, J. Nucl. Mater. **199**, 214 (1993).
7. B. B. Mandelbrot, *The Fractal Geometry of Nature* (Freeman, San Francisco, 1982; Inst. Komp. Issled., Moscow, 2002).
8. J. Feder, *Fractals* (Plenum, New York, 1988; Mir, Moscow, 1991).
9. V. S. Ivanova, A. S. Balankin, I. Zh. Bunin, and A. A. Oksagoev, *Synergetics and Fractals in Materials Science* (Nauka, Moscow, 1994) [in Russian].
10. A. G. Kolmakov, G. V. Vstovskiĭ, S. A. Maslyaev, and V. N. Pimenov, Perspekt. Mater., No. 4, 5 (1999).
11. I. A. Popova, N. A. Savrasova, and E. P. Domashevskaya, Kondens. Sredy Mezhfaz. Gran. **2**, 294 (2000).
12. G. V. Vstovsky, A. G. Kolmakov, and I. Zh. Bunin, *Introduction to Multifractal Parametrization of Material Structure* (Center for Regular & Chaotic Dynamics, Izhevsk, 2001) [in Russian].

Translated by P. Pozdeev

Technical Physics Letters, Vol. 31, No. 7, 2005, pp. 622–623. Translated from Pis'ma v Zhurnal Tekhnicheskoĭ Fiziki, Vol. 31, No. 14, 2005, pp. 83–87.

The Effect of Alternating Current on the Plasma Frequency of the Tunnel Josephson Junctions

I. N. Askerzade

Institute of Physics, National Academy of Sciences of Azerbaijan, Baku, Azerbaijan
Department of Physics, Ankara University, 06100 Tangodan, Ankara, Turkey
e-mail: solstphs@physics.ab.az; iasker@science.ankara.edu.tr

Received February 28, 2005

Abstract—The effect of alternating current on the plasma frequency of the tunnel Josephson junctions simultaneously carrying both direct (dc) and alternating (ac) currents has been studied. The presence of the ac component leads to a decrease in the plasma frequency. An analytical expression describing the plasma frequency as a function of the ac current amplitude is proposed. The obtained results agree with the recent experimental data on the properties of tunnel Josephson junctions. © *2005 Pleiades Publishing, Inc.*

In recent years, low-temperature quantum effects in the Josephson junctions have received much attention [1, 2]. As is known, the Josephson junction dynamics has much in common with the motion of a particle in a potential of the washboard type [3],

$$U(\phi) = -E_J(i\phi + \cos\phi), \quad (1)$$

where i is the dc current expressed in the I_c (critical current) units, ϕ is the Josephson phase, and $E_J = \hbar I_c/2e$ is Josephson energy. In the case when the capacitance of the junction is sufficiently large, the junction may exhibit slowly decaying oscillations of the plasma phase (determined by Eq. (1)) at the bottom of the potential well. The frequency of these oscillations (plasma frequency) depends on the dc current and is given by the formula (see, e.g., [3]),

$$\Omega_p = \left(\frac{2eI_c}{\hbar C}\right)^{1/2}(1 - i^2)^{1/4}. \quad (2)$$

Relation (2) is usually observed with high precision in the Josephson junctions connected to a dc voltage source. In the case of $I = I_c\sin\phi$, the theory [3] exhibits perfect agreement with experiment. However, there are deviations from the behavior predicted by formula (2) in the Josephson junctions characterized by anharmonic current–phase relations [4]. The anharmonicity may be cased by the simultaneous passage of both dc and ac currents of large amplitudes via the junction.

Recently, Gronbech-Jensen *et al.* [5] studied the dynamics of the tunnel Josephson junctions, simultaneously carrying dc and ac currents, by measuring the statistics of switching of low-temperature tunnel junctions of the Nb–$NbAlO_x$–Nb type to the resistive state. The critical current statistics in this system, which is controlled by thermal fluctuations at the bottom of the potential well (1), was determined for 10000 events. By changing the ac current amplitude, it was possible to control the dc current corresponding to a peak in the distribution of switching events.

The results obtained in [5] confirmed the validity of relation (2) for the plasma frequency for small amplitudes of the ac current component. However, as the ac current amplitude grows, the agreement of formula (2) with the experimental values measured in [5] deteriorates, which can be related to an anharmonic character of the potential (1) at large ac current amplitudes. However, no theoretical analysis of this situation has been presented.

This study was aimed at a theoretical investigation of the effect of alternating current on the plasma frequency of the tunnel Josephson junction simultaneously carrying dc and ac currents. The effect of the ac current component on the thermal activation threshold in the system under consideration was analyzed previously [6].

The dynamics of a Josephson junction can be described using the following equation [3]:

$$\ddot{\phi} + \alpha\dot{\phi} + \sin\phi = i + i_d\sin(\omega_d t), \quad (3)$$

where i and i_d are the dc and ac (drive) current components, respectively, expressed in units of the critical current I_c; ω_d is the applied ac field frequency expressed in units of the plasma frequency at a zero dc current, $\omega_p(i = 0) = (2eI_c/\hbar C)^{1/2}$.

In order to calculate the plasma frequency, with allowance for the ac current, the Josephson phase can be expressed as

$$\phi = \phi_0 + \phi_1, \quad (4)$$

where ϕ_1 and ϕ_0 are the fast (oscillating) and slow phase components, respectively. Substituting expression (4) into relation (3), we obtain the equation

$$\ddot{\phi}_1 + \alpha\dot{\phi}_1 + \sin\phi_0\cos\phi_1 + \cos\phi_0\sin\phi_1 = i + i_d\sin\omega_d t. \quad (5)$$

A solution of this equation can be found in the following form:

$$\phi_1 = -\frac{i_d}{\alpha^2 + \omega_d^2}\sin\omega_p t - \frac{\alpha}{\omega_p}\frac{i_d}{\alpha^2 + \omega_d^2}\cos\omega_p t. \quad (6)$$

For the tunnel Josephson junctions, that is, the junctions with low damping, we have $\alpha \ll 1$ and, hence, the second term in Eq. (6) can be ignored. Substituting the simplified expression into Eq. (5) and making transformations, we eventually obtain the following relations determining small oscillations of the phase at the bottom of the potential well:

$$\sin\phi_0 = \frac{i}{J_0\left(\frac{i_d}{\alpha^2 + \omega_d^2}\right)}, \quad (7)$$

$$\Omega_p = \left(\frac{2eI_c}{\hbar C}\right)^{1/2}\left(1 - \frac{i^2}{J_0^2\left(\frac{i_d}{\alpha^2 + \omega_d^2}\right)}\right)^{1/4}, \quad (8)$$

where $J_0(x)$ is the zero-order Bessel function. Relations (7) and (8) were obtained using formulas

$$\cos(a\sin\Omega t) = \sum_n A_n e^{in\Omega t}, \quad A_n = J_{2k}(a); \quad n = 2k, \quad (9)$$

$$\cos(a\sin\Omega t) = \sum_n B_n e^{in\Omega t}, \quad B_n = J_{2k+1}(a); \quad n = 2k+1. \quad (10)$$

Note that, in the limit of $i_d \longrightarrow 0$, formula (8) converts into relation (2). According to formula (8), an increase in the ac current component i_d leads to a decrease in the plasma frequency Ω_p. Thus, the presence of the ac component leads to renormalization of the plasma frequency (2) of the tunnel Josephson junction. The results of calculations using formulas (2) and (8) are presented in the figure by the solid and dashed curves, respectively, in comparison to the experimental data (black circles) taken from [5]. As can be seen from these data, formula (8) provides a better description of the experimental results reported in [5].

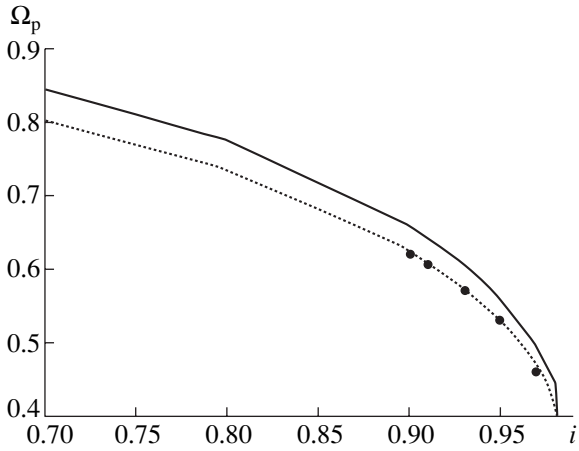

Dependence of the plasma frequency of a tunnel Josephson junction on the ac current amplitude: (black circles) experimental data from [5]; (solid curve) calculation using formula (2) ($i_d = 0$); (dashed curve) calculation using formula (8) ($i_d \neq 0$).

In conclusion, a theory of the thermal activation of the tunnel Josephson junctions simultaneously carrying both direct (dc) and alternating (ac) currents was developed. It was demonstrated that the presence of an ac current component leads to a decrease in the plasma frequency of the Josephson junction, the effect being proportional to the ac current amplitude. The results of calculations well agree with the published experimental data.

REFERENCES

1. *Quantum Mesoscopic Phenomena and Mesoscopic Devices in Microelectronics: Proceedings of the NATO Advanced Study Institute, Ankara, 1999*, Ed. by I. O. Kulik and R. Ellialtioglu (Kluwer Academic, Dordrecht, 2000).
2. I. N. Askerzade, Zh. Tekh. Fiz. **73** (4), 140 (2003) [Tech. Phys. **48**, 519 (2003)].
3. K. K. Likharev, *Dynamics of Josephson Junctions and Circuits* (Nauka, Moscow, 1985; Gordon and Bearch, New York, 1986).
4. I. N. Askerzade, Zh. Tekh. Fiz. **73** (11), 140 (2003) [Tech. Phys. **48**, 1496 (2003)].
5. N. Gronbech-Jensen, M. G. Castelliano, F. Chiarello, *et al.*, cond-mat/0403245.
6. I. N. Askerzade, Pis'ma Zh. Tekh. Fiz. **30** (20), 30 (2004) [Tech. Phys. Lett. **30**, 857 (2004)].

Translated by P. Pozdeev

Technical Physics Letters, Vol. 31, No. 7, 2005, pp. 624–627. Translated from Pis'ma v Zhurnal Tekhnicheskoĭ Fiziki, Vol. 31, No. 14, 2005, pp. 88–94.

High Repetition Rate Pulsed X-ray Source Employing Supershort Avalanche Electron Beams

V. F. Tarasenko[a,*], S. K. Lyubutin[b,], B. G. Slovikovsky[b], and I. D. Kostyrya[a]**

[a] *Institute of High-Current Electronics, Siberian Division, Russian Academy of Sciences, Tomsk, Russia*

[b] *Institute of Electrophysics, Ural Division, Russian Academy of Sciences, Yekaterinburg, Russia*

*e-mail: * VFT@loi.hcei.tsc.ru; ** rukin@iep.uran.ru*

Received March 11, 2005

Abstract—The formation of a volume discharge in an open gas diode with coaxial electrodes was accompanied by hard X-ray emission. The conditions of supershort avalanche electron beam formation are retained at a pulse repetition rate up to 1.5 kHz. © *2005 Pleiades Publishing, Inc.*

Introduction. Previously, it was reported [1–6] that subnanosecond electron beams are obtained in gas-filled diodes at working gas pressures of 1 bar and above, and some possible applications have been considered. Such supershort avalanche electron beams possess unique properties [7]. In gas diodes with optimum design (characterized by small dimensions and low inductance [3, 4]) filled with air at atmospheric pressure, the beam current amplitudes reached several hundreds of amperes at a pulse full width at half height (FWHM) not exceeding several hundreds f picoseconds [2–4, 7]. Recently, a diode with the supershort avalanche electron beam was used for the volume discharge formation in a CO_2 laser operating at atmospheric pressure [5] and for the excitation of cathodoluminescence in crystals [6]. However, all previous experiments devoted to the formation of supershort avalanche electron beams were performed in the regimes of single pulses or low repetition rates (not exceeding 5 Hz). At the same time, the modern generators of high-voltage nanosecond pulses can operate in a pulse train regime with repetition rates up to 1 kHz and above [8, 9]. In particular, a solid-state generator recently described in [9] produced voltage pulses at a repetition rate of 3.5 kHz with an amplitude of 150–160 kV, a pulse width (FWHM) of 1.4 ns, and a leading front duration of 200–250 ns in a 50-Ω transmission line.

This study is devoted to assessing the possibility of obtaining supershort avalanche electron beams at high repetition frequencies.

Experimental. The experiments were performed using a gas-filled diode in a setup described in detail elsewhere [9, 10]. Overvoltage on a tunneling-impact sharpening device was created using a solid-state generator of short pulses employing SOS-diodes and an intermediate pulse-shaping circuit [10] operating in the conventional shock ionization wave regime. The generator provided output pulses with an amplitude of 220 kV and a leading front duration of about 1 ns. The tunneling-impact sharpener, connected to the input of a transmission line, formed pulses with a leading front duration of about 250 ps. All lines of the pulse generator were filled with a transformer oil.

The gas diode was analogous to that described in [2], comprising a cathode mounted on the central electrode and an anode. The experiments were performed with anodes and cathodes of two types. Cathode 1 represented a tube with a diameter of 6 mm, made of a 100-μm-thick steel foil. Cathode 2 had the shape of a steel ball with a diameter of 17.4 mm. Flat anode 1 was made of a 45-μm-thick AlBe foil, while the role of anode 2 was played by the inner metal surface of the gas diode case, which provided effective cooling in the regime of high pulse repetition rates.

In regime 1, the gas diode operated with flat anode 1 and cathode 1, whereby the discharge was formed between the cathode edge and the central part of the flat anode. In this regime, the interelectrode gap width could be varied from 9 to 16 mm. The first regime was convenient for measuring the electron beam parameters behind the output foil. In open-diode regime 2, the AlBe foil was removed and the discharge was initiated between the edge of tube cathode 1 (or the side surface of ball cathode 2) and the edge of a cylindrical case of the gas diode. The electrode arrangement was coaxial, the interelectrode distance from the cathode to the gas diode edge was 21 mm for cathode 1 and 15.3 mm for cathode 2. Since the foil in regime 2 was removed, the

1063-7850/05/3107-0624$26.00

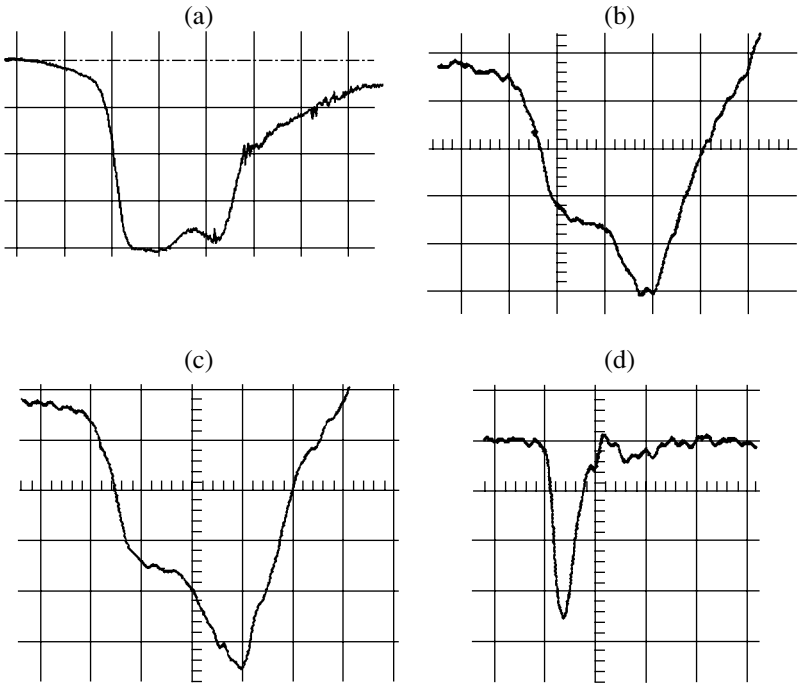

Fig. 1. The typical oscillograms of (a, b, c) voltage pulses and (d) electron beam current pulse measured at low pulse repetition rates. (abscissa scale: 0.5 ns/div; ordinate scale: 39 kV/div (a, b, c) and 30 A/div (d)).

integral pattern of discharge could be observed and photographed using a photo camera.

In this regime, the presence of the electron beam and its relative intensity were determined using a Victoreen 541R dose meter placed at a distance of 5 cm from the foil plane and oriented perpendicularly to the cathode axis. The system could be operated in a pulse train regime, with a repetition rate up to 1.5 kHz and the number of pulses in a train varied from 150 to 3000.

The voltage pulses in the transmission line were measured using capacitive voltage dividers. The electron beam current pulses were measured using a low-inductance collector with a diameter of 2 cm loaded on a coaxial cable. The output pulses from the voltage divider and the collector were fed to a 6-GHz digital stroboscopic oscillograph (TDS 6604, 20 G/s, which corresponded to 20 points/ns). The intrinsic signal buildup time in the measuring circuit did not exceed 100 ps. The measurements were performed either in the regime of single pulses, in a pulse sequence mode with the repetition frequency varied from 1.5 to 1500 Hz, or in a pulse train mode (at a frequency of 100 Hz and above).

Results and discussion. Figure 1a shows the pulse shape measured at the output of the voltage divider in the transmission line. This pulse was obtained without reflection from the gas diode, which was eliminated by increasing the transmission line length. The voltage amplitude was 156 kV, the current amplitude was 3.2 kA, and the pulse width (FWHM) was 1.4 ns. Figure 1b shows the output voltage pulse measured for the gas diode operating in regime 1 with cathode 1; Fig. 1d presents the beam current pulse measured behind the foil. The voltage amplitude in the incident wave was 134 kV, and that for the reflected pulse was 55 kV, which corresponds to a gas diode resistance of ~120 Ω and a maximum diode voltage of 189 kV. The amplitude of the supershort avalanche electron beam (Fig. 1d) measured behind the foil in the optimum regimes exceeded 100 A. Figure 1c shows the shape of the voltage pulse measured for the open diode operating with cathode 1. The increase in the reflected pulse amplitude is related to an increase in the interelectrode gap width and to a growth of the diode resistance to ~170 Ω. Note that the maximum in the oscillograms of voltage pulses in Fig. 1b and 1c is followed by a drop, which is related to a decrease in the discharge plasma resistance during the pulse.

The most important result was obtained for the open diode operating in the pulse train mode. In the regime with cathode 1, the maximum X-ray exposure dose (fluence) was observed for a pulse repetition rate of 1.5 Hz and above. As the repetition rate was increased to 100 Hz, the fluence exhibited a decrease (at 100 Hz, the dose meter did not detect X-ray emission over a sequence of 450 pulses). However, when the pulse repetition rate was increased further, the X-ray emission was detected again and the second maximum in the fluence was observed at a frequency of ~200 Hz. When the

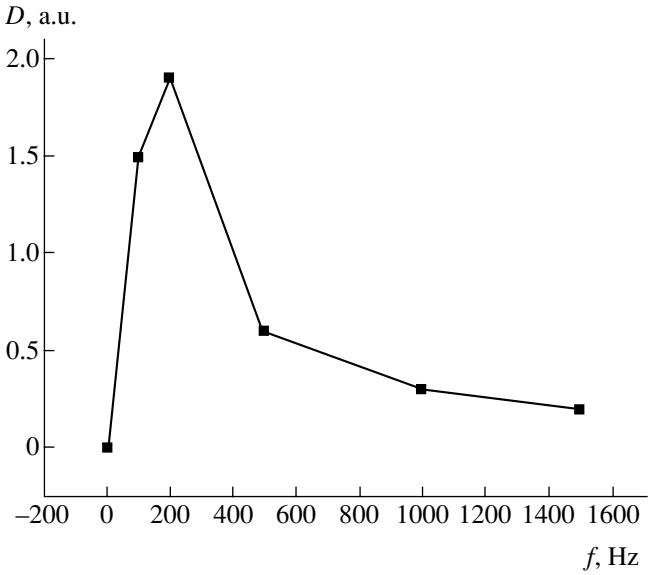

Fig. 2. A plot of the X-ray fluence versus pulse repetition rate in the open diode regime with cathode 1.

repetition rate was increased from 0.5 to 1.5 kHz, the fluence (calculated per 150 pulse train) decreased only by half.

In the experiment with cathode 2 (Fig. 2), the minimum fluence was observed for a pulse repetition rate of 1.5 Hz, while the maximum was again observed at ~200 Hz. When the repetition rate was increased from 0.5 to 1.5 kHz, the fluence (calculated per 150 pulse train) decreased, but by a factor of no more than 3. At 1.5 kHz, the fluence with cathode 2 was 1.5 times than with cathode 1. When a 5-mm-thick lead screen was placed in front of the dose meter, the X-ray emission was not detected in all regimes, whereas a 170-μm-thick aluminum foil did not significantly reduce the dose meter readings.

The results of visual observations and photographs of the integral emission from the open gas diode showed that the discharge formed in single-pulse mode had a volume character and was concentrated at the sites of small enhancement of the electric field. At a low repetition rate and a small number of pulses in the train, we also observed a volume discharge in the form of expanding streams with bright points at the tube end (cathode 1) or on a part of the ball surface (cathode 2) at a minimum distance from the anode.

At high repetition rates and large numbers of pulses in the train (more than 50), the form of discharge in the interelectrode gap changed, but its volume character was retained. With increasing repetition rate and the number of pulses in train, the region occupied by the discharge expanded. When the number of pulses in the train exceeded ~1000, bright channels appeared in the interelectrode gap. It should be noted that the X-ray fluences in regimes 1 and 2 with cathode 1 differed only by 20% (16 and 13 mR per 150 pulses at 1.5 kHz, respectively). The dose meter was in both cases placed at a distance of 5 cm from the foil plane.

Discussion. When a high-voltage pulse with a subnanosecond front is applied to the interelectrode gap, a critical field is generated near the anode [11] by the approaching plasma front and an supershort avalanche electron beam is formed. The beam energy and amplitude depend on various factors [3], including the pulse repetition rate. Our investigation showed for the first time that the conditions of supershort avalanche electron beam formation are retained at a high pulse repetition rate. The X-ray emission mostly results from the electron bremsstrahlung on the anode. The second maximum in the dependence of the X-ray fluence on the repetition rate is related to an increase in the region occupied by the discharge. As the pulse repetition rate increases, the plasma in the regions with maximum current densities cannot recombine and the conditions of electron beam formation are deteriorated (because of a decrease in the electric field gradient at the anode). As the current density decreases, the discharge region expands and the conditions of beam formation are realized in the regions of lower current density, which allows the X-ray emission to be detected at higher repetition rates.

Conclusions. Thus, we have demonstrated for the first time that the conditions of supershort avalanche electron beam formation are retained at a high pulse repetition rate (up to 1.5 kHz). The X-ray emission generated by electrons with the energies above 60 keV was detected in the case of nanosecond high-voltage pulses and a volume character of discharge in open gas diodes filled with air at atmospheric pressure. The dependence of the X-ray fluence on the pulse repetition rate can probably be used for increasing the stability of discharge sharpeners at high repetition rates.

Acknowledgments. The authors are grateful to V.G. Shpak and S.N. Rukin for their support of this study, S.A. Shunailov for his help in experiments, and V.M. Orlovskii for creating a collector for the detection of subnanosecond electron beams.

REFERENCES

1. S. B. Alekssev, V. M. Orlovskiĭ, and V. F. Tarasenko, Pis'ma Zh. Tekh. Fiz. **29** (10), 29 (2003) [Tech. Phys. Lett. **29**, 411 (2003)].
2. V. F. Tarasenko, V. G. Shpak, S. A. Shunailov, *et al.*, Pis'ma Zh. Tekh. Fiz. **29** (21), 1 (2003) [Tech. Phys. Lett. **29**, 879 (2003)].
3. V. F. Tarasenko, V. S. Skakun, I. D. Kostyrya, *et al.*, Laser Part. Beams **22**, 75 (2004).

4. S. B. Alekssev, V. P. Gubanov, V. M. Orlovskiĭ, and V. F. Tarasenko, Pis'ma Zh. Tekh. Fiz. **30** (20), 36 (2004) [Tech. Phys. Lett. **30**, 859 (2004)].

5. S. B. Alekssev, V. M. Orlovskiĭ, and V. F. Tarasenko, Kvantovaya Élektron. (Moscow) **33**, 1059 (2003).

6. E. I. Lipatov, V. F. Tarasenko, V. M. Orlovskiĭ, *et al.*, Pis'ma Zh. Tekh. Fiz. **31** (6), 29 (2005) [Tech. Phys. Lett. **31**, 231 (2005)].

7. V. F. Tarasenko, V. M. Orlovskiĭ, and S. A. Shunailov, Izv. Vyssh. Uchebn. Zaved., Fiz., No. 3, 94 (2003).

8. V. P. Gubanov, S. D. Korovin, I. V. Pegel, *et al.*, IEEE Trans. Plasma Sci. **25**, 258 (1997).

9. S. K. Lyubutin, S. N. Rukin, B. G. Slovikovskiĭ, and S. N. Tsyranov, Pis'ma Zh. Tekh. Fiz. **31** (5), 36 (2005) [Tech. Phys. Lett. **31**, 196 (2005)].

10. E. A. Anichkin, S. K. Lyubutin, A. V. Ponomarev, *et al.*, Prib. Tekh. Éksp., No. 4, 106 (2002).

11. V. F. Tarasenko and S. I. Yakovlenko, Usp. Fiz. Nauk **174**, 953 (2004) [Phys. Usp. **47**, 887 (2004)].

Translated by P. Pozdeev